Phenomenology of the Higgs and Flavour Physics In the Standard Model and Beyond

D I S S E R T A T I O N

zur Erlangung des akademischen Grades

doctor rerum naturalium
(Dr. rer. nat.)
im Fach Physik

eingereicht an der
Mathematisch-Wissenschaftlichen Fakultät
Humboldt-Universität zu Berlin

von
M.Sc. Lina Alasfar
geboren am 27. 09. 1994 in Riad

Präsidentin der Humboldt-Universität zu Berlin:
Prof. Dr.-Ing. Dr. Sabine Kunst

Dekan der Mathematisch-Wissenschaftlichen Fakultät:
Prof. Dr. Elmar Kulke

Gutachter:
1. Prof. Dr. R. Gröber, Humboldt-Universität zu Berlin
2. Prof. Dr. Dr. M. Musterman, Potsdam-Institut fur Klimafolgenforschung
3. Prof. Dr. M. Mustermann2, Heidelberg

Tag der mündlichen Prüfung: 06. November 2013

Contents

List of publications

1. **L. Alasfar**, G. Degrassi, P. P. Giardino, R. Gröber and M. Vitti
   Virtual corrections to $gg \to ZH$ via a transverse momentum expansion
   JHEP **05** (2021), 168
   arXiv:2103.06225 [hep-ph].

2. **L. Alasfar**, A. Azatov, J. de Blas, A. Paul and M. Valli
   B anomalies under the lens of electroweak precision
   JHEP **12** (2020), 016
   arXiv:2007.04400 [hep-ph].

3. **L. Alasfar**, R. Corral Lopez and R. Gröber
   Probing Higgs couplings to light quarks via Higgs pair production
   JHEP **11** (2019), 088
   arXiv:1909.05279 [hep-ph].

Part I

Higgs Physics

1 The Standard Model Higgs boson

> It's very nice to be right sometimes...
> it has certainly been a long wait.
>
> *Peter Higgs*

Write intro here

1.1 Spontaneous symmetry breaking

Before talking about symmetry breaking, we need to discuss the concept of symmetry in physics. Symmetry has an essential role in studying physical systems. It manifests not only as a geometric feature of physical objects but also in the dynamics of physical systems. For example, one can find symmetries in the equation of motion, Lagrangians/Hamiltonians and actions. The magnetisation of materials is a good example of the role that symmetry plays in describing physical behaviour. For instance, **paramagnetic** materials have a positive magnetic susceptibility χ_B due to the random arrangement of their electrons' spins. The paramagnetic material spins arrangement will therefore possess rotational symmetry. The material has no *preferred direction* in space [1]. On the contrary, **ferromagnetic** materials with the electrons' spins aligned in a certain direction, will not have such symmetry as there will be a preferred direction, see Figure 1.1.

In particle physics and quantum field theory, symmetry plays an essential role in the taxonomy and dynamics of elementary particles and their bound states, i.e. hadrons, cf. [2, 3]. There are two types of symmetries considered when studying elementary particles and their quantum fields: external and internal symmetries. The first is the symmetry of the spacetime background. Typically, this is a four-dimensional Poincaré symmetry. However, in some models, higher spacetime dimensions or non-flat geometries are considered. Though there is no current evidence of higher dimensions or indications of non-flat spacetime from colliders and cosmological observations [4]. The second class of symmetries is internal symmetries stemming from the quantum nature of these particles/fields. Because their state is described by a **ray** in complex Hilbert/Fock spaces, internal symmetries are simply symmetries of rotations in these spaces that keep the action variation unchanged. Internal symmetries are usually described in terms of simple

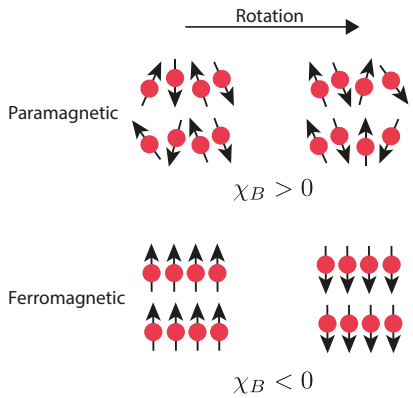

Figure 1.1. In paramagnetic materials, the spins are randomly distributed such that a rotation performed on the system will keep the spin distribution invariant. However, for ferromagnetic materials, where the spins are aligned in a single direction, the symmetry is broken, and the system has a preferred direction.

or product of simple **Lie groups**, e.g. $SU(N)$ [1], and particles/fields will be arranged as multiplets in some representation of the groups. The rotations of the states could be parametrised by constants. In this case, the symmetry is called **global**, or fields of spacetime, where the symmetry is then called **local** or **gauged**.

Gauge symmetries describe rotations in the state space that depend on spacetime, the generator of the gauge transformations could propagate between two spacetime points. This is the way particle/field interactions are described in quantum field theory. The generators of these gauge transformations are called gauge bosons, and they mediate the interactions between the particles/fields and transform under the adjoint representation of the gauge group. Hence, we observe that gauge symmetries are the basis of describing the fundamental interactions of nature, which we call **gauge theories**.

An example of a gauge theory that is realised in nature is the **Standard Model** (SM). Which is a gauge theory based on the group $G_{\text{SM}} := SU(3)_C \otimes SU(2)_L \otimes U(1)_Y$. The first simple group is for the *strong* interaction described by quantum chromodynamics (QCD). The product of the two remaining groups $SU(2)_L \otimes U(1)_Y$ forms the Weinberg-Salam *electroweak* (EW) model [7–9], where $SU(2)_L$ describes the weak interaction which only couples to *left handed* fermions and $U(1)_Y$ is the weak hypercharge Y gauge group, defined by the formula

$$Y = 2(Q - T_3). \tag{1.1}$$

Where Q is the electric charge and T_3 is the third component of the weak isospin. A description of the matter content of the SM and their multiplicities with respect to G_{SM}

[1] Gauge theories based on finite groups have been investigated in the literature, but their phenomenological significance is yet to be further investigated [5, 6]

is shown in Table 1.1

Particle/Field	G_{SM} multiplicity	mass [GeV]
	Quarks	
$Q = \binom{u_L}{d_L}, \binom{c_L}{s_L}, \binom{t_L}{b_L}$	$(\mathbf{3}, \mathbf{2}, 1/6)$	$m_u = 2.16 \cdot 10^{-3}$, $m_d = 2.67 \cdot 10^{-3}$
$U = u_R, c_R, t_R$	$(\mathbf{3}, \mathbf{1}, 2/3)$	$m_c = 0.93 \cdot 10^{-2}$, $m_s = 1.27$
$D = d_R, s_R, b_R$	$(\mathbf{3}, \mathbf{1}, -1/3)$	$m_t = 172.4$, $m_b = 4.18$
	Leptons	
$L = \binom{\nu_{e,L}}{e_L}, \binom{\nu_{\mu,L}}{\mu_L}, \binom{\nu_{\tau,L}}{\tau_L}$	$(\mathbf{1}, \mathbf{2}, -1/2)$	$m_e = 0.511 \cdot 10^{-3}$, $m_\mu = 1.05 \cdot 10^{-2}$
$E = e_R, \mu_R, \tau_R$	$(\mathbf{1}, \mathbf{1}, -1)$	$m_\tau = 1.77$,m_ν =??
	Gauge bosons	
$g/G^A_\mu, \;\; A = 1 \ldots 8$	$(\mathbf{8}, \mathbf{1}, 0)$	0.0
γ/A_μ	$(\mathbf{1}, \mathbf{1}, 0)$	0.0
$W^\pm_\mu$	$(\mathbf{1}, \mathbf{3}, 0)$	80.379
Z_μ	$(\mathbf{1}, \mathbf{3}, 0)$	91.1876
	The Higgs boson	
h	$(\mathbf{1}, \mathbf{2}, 1/2)$	125.10

Table 1.1. The SM constituents, their multiplicities with respect to the SM gauge group $G_{\text{SM}} := SU(3)_C \otimes SU(2)_L \otimes U(1)_Y$ and masses. The mass of the neutrinos ν is zero according to the SM prediction, but observations suggest that they are massive, and only the difference between the three masses is known [10]. The values of the masses are taken from the Particle Data Group (PDG) [4], and used throughout this thesis.

The SM has been very successful at describing particle interactions even when challenged by numerous precision tests at LEP and SLD [11–14] and later at DØ [15] and the LHC [16, 17] Nevertheless, it fails to describe the ground state if only the fermion and gauge sectors are considered. The reason for this shortcoming is that the $W^\pm$ and Z bosons have a mass, this violates the EW gauge symmetry. This can be easily seen by looking at the mass term of a spin 1 field B^A_μ

$$\mathcal{L} = m_B B^{A,\mu} B^A_\mu, \tag{1.2}$$

and performing an $SU(N)$ gauge transformation

$$B^A_\mu \to B^A_\mu + \partial_\mu \Lambda^A + g\, \varepsilon^A_{BC} B^B_\mu \Lambda^C. \tag{1.3}$$

We see that the mass term is invariant under these transformations. Secondly, because the SM is a chiral theory, as only left-handed fermions would be doublets under $SU(2)_L$,

the Dirac mass term

$$\mathcal{L}_{\mathrm{D}} = m_D \overline{\psi}_L \psi_R + \mathrm{h.c.}, \tag{1.4}$$

cannot be a singlet under $SU(2)_L$, hence also violating the EW symmetry. Despite quark and lepton masses being forbidden by the EW symmetry, we indeed observe that they do have a mass, and since they also carry charges this mass has to be a Dirac mass.

In order for the EW model to be consistent at the ground state like it is in the interaction states. A mechanism for spontaneous symmetry breaking going from an interaction state to the vacuum ought to be introduced.

1.1.1 Nambu-Goldstone theorem

Coming back to the example of the paramagnetic-ferromagnetic materials, when heated above a certain temperature, known as the **Curie Temperature** T_C will undergo a phase transition and become paramagnetic (losing their permanent magnet property), in the mean-field theory approximation the magnetic susceptibility is related to the temperature of the metal via the relation

$$\chi_B \sim (T - T_C)^{-\gamma}, \tag{1.5}$$

where γ is a critical exponent. We see that if the metal temperature $T > T_C$ the metal is in an *disordered phase* and when $T < T_C$ it is in the *ordered phase*,i.e. χ_B is the **order parameter** of this system. At the Curie temperature, the system will be at the *critical point* where the susceptibility is divergent. The exponent γ is not used to describe the system at the critical point. There is a "pictorial" description of the metal at the critical point which is helpful in picturing the Goldstone theorem. Starting at $T > T_C$, the metal would be in a paramagnetic phase, where the spins are randomly arranged. As the temperature becomes lower and lower, thermal fluctuations start to lessen. One or more regions of the metal, some of the spins will start to get aligned With continued cooling, nearing T_C, these turned spins will affect their neighbours turning them into their directions. At the critical point $T = T_C$, the system behaves in a peculiar manner, when one would see regions of spins in "up" and others in "down" directions. The system will resemble a fractal of these regions, becoming scale-invariant. Additionally, waves of oscillating local magnetisation will propagate. These waves, or spinless quasiparticles (called **Magnons**) are Goldstone bosons emerging from spontaneous symmetry breaking. Which will manifest at $T < T_C$ as the spins will be arranged in a certain single direction and the metal becomes ferromagnetic.

Theorem 1 (Nambu-Goldstone)**.** When a continuous symmetry has a conserved currents but broken in the ground state (vacuum) is called to be spontaneously broken. There is a scalar boson associated with each broken generator of this spontaneously broken symmetry. The modes of these bosons are fluctuations of the order parameter.

This theorem first emerged from condensed matter physics, particularly superconductors [18, 19]. However, it soon got applied to relativistic quantum field theories [20].

1.2 The Higgs mechanism

In order to solve the aforementioned shortcomings of the Weinberg-Salam model, Nambu-Goldstone theorem has been first proposed by P. W. Anderson [21]. However, the way that Anderson formulated his theory was unfamiliar to particle physicists and used a non-relativistic picture to illustrate how photons could gain mass in an electron plasma with a plasma frequency ω_p

$$m_\gamma^{\text{plasma}} = \frac{\hbar\omega_p}{c^2} \tag{1.6}$$

Later on, a theory that explains the mass generation of the EW gauge bosons has been published in an almost simultaneous manner by R. Braut and F. Englert [22], P. Higgs [23] and G. Guralnik, C. R. Hagen, and T. Kibble [24, 25][2]. The Higgs mechanism starts by considering the spontaneous symmetry breaking (SSB) of the EW sector of the SM via the pattern

$$SU(2)_L \otimes U(1)_Y \longrightarrow U(1)_Q \tag{1.7}$$

This is achieved by the vacuum expectation value (vev) of a complex scalar field $\phi \sim (\mathbf{1}, \mathbf{2}, +1/2)$, with the Lagrangian

$$\mathcal{L} = D_\mu\phi^* D^\mu\phi - V, \qquad V := \mu^2\phi^*\phi + \lambda(\phi^*\phi)^2, \tag{1.8}$$

with V denoting the Higgs potential, illustrated in Figure 1.2, which gives non-vanishing vacuum for $\mu^2 < 0$. The field ϕ is given explicitly by

$$\phi = \begin{pmatrix} \phi^1 + i\phi^2 \\ \frac{1}{\sqrt{2}}(h+v) - i\phi^3 \end{pmatrix} \tag{1.9}$$

The covariant derivative

$$D_\mu = \partial_\mu - ig_2\frac{\sigma_a}{2}W_\mu^a - ig_1\frac{1}{2}B_\mu, \tag{1.10}$$

dictates the coupling between the Higgs field and the EW gauge bosons and g_3, g_2 and g_1 are, respectively, the coupling constants of $SU(3)_C$, $SU(2)_L$ and $U(1)_Y$. The minimum

[2] All of these authors have contributed to the theory of SM spontaneous symmetry breaking (SSB). By calling it the "Higgs" mechanism or boson. I, by no means, have intended to ignore the role played by the rest, rather, I wanted to stick the most widely-used terminology in the field.

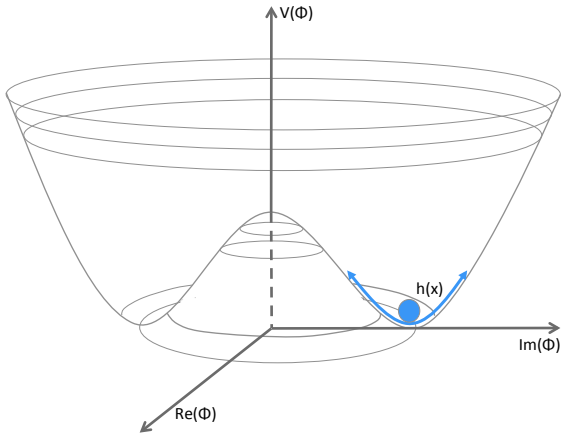

Figure 1.2. The characteristic shape of the Higgs potential showing a non-zero vacuum. While thee physical Higgs boson is an oscillation within the energy well illustrated in the diagram with blue arrows., this illustration is taken from [26].

of the scalar potential is then obtained by

$$\frac{\partial V}{\partial \phi} \mid_{\phi \to v} = 0, \tag{1.11}$$

which for a tachyonic mass $\mu^2 < 0$ will have a real non-vanishing values v corresponding to the vev of this field $\langle \phi \rangle = \left(\begin{smallmatrix} 0 \\ \frac{v}{\sqrt{2}} \end{smallmatrix}\right)$.

According to Nambu-Goldstone theorem, the three broken generators of $SU(2)_L \otimes U(1)_Y$ will become massive, and they are the $W^{\pm}$ and Z bosons, while the photon will remain massless. We will have three massless Goldstone bosons $G^{\pm} = \frac{1}{2}(\phi^1 \pm i\phi^2)$ and $G^0 = \phi^3$ that are "eaten" by the aforementioned massive photons. Where they become the longitudinal polarisations of $W^{\pm}$ and Z boson. In order to see this more concretely, we start by looking at the terms of the EW Lagrangian where the field ϕ couples to the gauge bosons, in the unbroken phase

$$D_\mu \phi^* D^\mu \phi = \frac{1}{2}|\partial_\mu \phi|^2 + \frac{1}{8} g_2^2 |\phi|^2 |W_\mu^1 + i W_\mu^2|^2 + \frac{1}{8}|\phi|^2 |g_2 W_\mu^3 - g_1 B_\mu|^2 \tag{1.12}$$

After SSB, we write the gauge bosons in the mass basis

$$\begin{aligned} W_\mu^\pm &= \frac{1}{\sqrt{2}}(W_\mu^1 \pm iW_\mu^2), \\ Z_\mu &= \frac{1}{\sqrt{g_1^2+g_2^2}}\left(g_2 W_\mu^3 - g_1 B_\mu\right), \\ A_\mu &= \frac{1}{\sqrt{g_1^2+g_2^2}}\left(g_2 W_\mu^3 + g_1 B_\mu\right). \end{aligned} \tag{1.13}$$

From this, the electric change is identified as the coupling constant to the photon A_μ

$$e = \frac{g_1}{\sqrt{g_1^2+g_2^2}}. \tag{1.14}$$

It is useful to define **Weinberg angle** θ_W, an important EW parameter relating the electric charge to the weak coupling g_2

$$\sin\theta_W = \frac{e}{g_2} \approx 0.231214, \tag{1.15}$$

typically the sin and cos of the Weinberg angle are denoted by s_W and c_W, respectively. We use the unitary gauge, to absorb the Goldstone bosons into the $W^\pm$ and Z longitudinal polarisations. In this gauge the Higgs doublet can be written as

$$\phi \to \begin{pmatrix} 0 \\ \frac{1}{\sqrt{2}}(h+v). \end{pmatrix}, \qquad v = 246\,\text{GeV}. \tag{1.16}$$

With these substitutions, one can read off the masses of the gauge bosons their bilinear terms in (1.12)

$$m_W = \frac{vg_2}{2} \qquad m_Z = \frac{v}{2}\sqrt{g_1^2+g_2^2} \qquad m_A = 0. \tag{1.17}$$

Since ϕ is a complex doublet. We have seen that it has four components, and three of them correspond to the Goldstone bosons, thus one remains physical h which is what we now identify with the "Higgs boson" discovered in the Summer of 2012 [27, 28]. The couplings between the Higgs and the electroweak bosons is related to their mass via the vev

$$g_{hVV} = \frac{2m_V^2}{v}, \qquad g_{hhVV} = \frac{2m_V^2}{v^2}. \tag{1.18}$$

By substituting (1.16), into the Higgs potential (1.8) one can write the mass of the physical Higgs boson in terms of the vev

$$m_h = \sqrt{2\lambda} v. \tag{1.19}$$

The physical Higgs mass is related to the μ parameter via the relation

$$m_h^2 = -2\mu^2, \tag{1.20}$$

One can see that the mass term after SSB changes its sign, characterising the order-parameter for this system, analogous to the magnetic susceptibility for the magnetisation of materials example. One could also identify the self-couplings of h, the trilinear and quartic couplings

$$g_{hhh} = 3\lambda v = 3\frac{m_h^2}{v}, \qquad g_{hhhh} = 3\lambda = 3\frac{m_h^2}{v^2}. \tag{1.21}$$

1.3 Yukawa interaction

It is possible to also use the Higgs vev to give fermions their masses by introducing a Yukawa-interaction terms, first introduced by S. Weinberg [9]

$$\mathcal{L}_{\text{Yuk}} = -y_e \,\overline{L}\,\phi\, E - y_d \,\overline{Q}\,\phi\, D - y_u \,\overline{Q}\,\tilde{\phi}\, U \;\; + \text{h.c.}, \tag{1.22}$$

with $\tilde{\phi} = i\sigma_2\phi$ and y_e, y_d, y_u are 3×3 matrices. These matrices are free parameters in the SM. As the Higgs boson acquires a the vev, the fermions will acquire a mass $m_f = v y'_f$ and the Higgs boson coupling to the fermions is given by

$$g_{h\overline{f}f} = \frac{m_f}{v}, \tag{1.23}$$

and the Yukawa matrices will be fixed in the mass basis y'_f by measurements of the fermion masses.
Leptonic Yukawa matrix is diagonal, with a degeneracy between the flavour and masses basis, this manifests as lepton family number conservation (the lepton family operator commutes with the Hamiltonian.). However, for the quarks, the situation is more complicated. One can rotate these matrices to the mass basis via a bi-unitary transformation via the unitary matrices $\mathcal{V}_Q, \mathcal{U}_Q$ for $q = u, d$

$$y_q \longrightarrow y'_f = \mathcal{V}_q^\dagger \, y_q \, \mathcal{U}_q = \text{diag}\left(m_{q_1}, m_{q_2}, m_{q_3}\right). \tag{1.24}$$

However, the is no degeneracy here as the Hamiltonian does not commute with the quark flavour operator. This is because the transformation matrices for the up and down-type quarks are not the same. The charged EW quark currents contains flavour mixing de-

scribed by the Kabibbo-Kobayashi-Maskawa (CKM) matrix [29, 30]. More details on the flavour sector of the SM is discussed in **??**
Figure 1.3 shows all the SM couplings' strengths, with the thickness of the chord is proportional to the strength of the coupling, on can see the Higgs couplings in orange. In

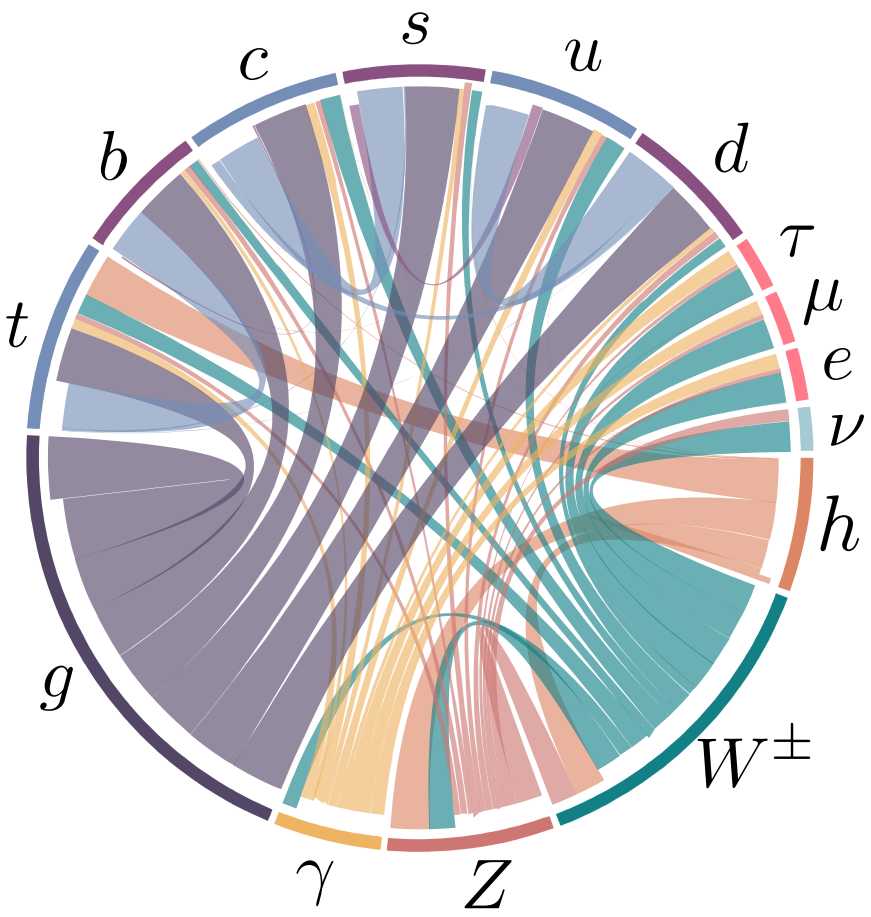

Figure 1.3. The SM Yukawa couplings are proportional to the quark masses, because of the the Higgs Yukawa couplings span about 6 orders of magnitude, as seen in the case of quarks here. This large hierarchy cannot be explained by the SM.

this figure, we cannot easily see Higgs coupling to the fermions, except for its couplings

to the third generation. Strictly speaking, if we further examined the Yukawa coupling using a logarithmic scale and focused on the quark sector as Figure 1.4 illustrates. We observe that these Yukawa couplings span about 6 orders of magnitudes with marked hierarchy amongst generations. As these couplings are in fact free parameters in the SM, and only determined by the experimental measurements of the quark (or equally applies lepton) masses. This hierarchy of quark masses therefore cannot be explain by the SM Higgs mechanism, and sometimes known as the old flavour puzzle.
In later chapters, we will examine the experimental effort to better measure these couplings and how Higgs pair production can be used to probe them in **??**. Even the potential of using techniques from *interpretable machine learning* to further improve Higgs pair sensitivity to probing light Yukawas **??**. Then in **??** we'll examine the EFT and UV models to modify them.

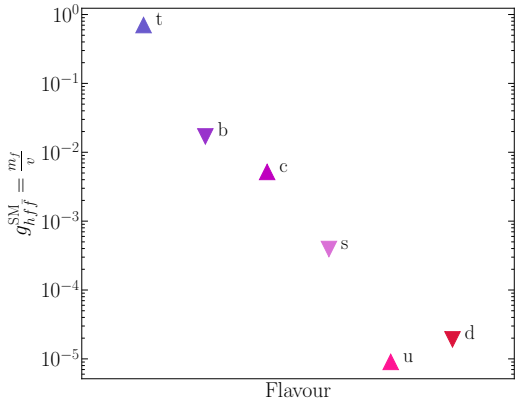

Figure 1.4. A chord diagram showing the SM couplings, with the coupling strength illustrated by the chord thickness. Higgs couplings are coloured in orange.

1.4 The Higgs and EW precision observables

Higgs physics is intertwined with the EW sector for example, the Higgs vev is determined from Fermi's constant $v = (\sqrt{2}G_F)^{-1/2}$, and is fixed by muon lifetime measurements, and comparing it with the theoretical predictions [31–34]

$$\tau_\mu^{-1} = \frac{G_F^2 m_\mu^5}{192\pi^3}\left(1 - \frac{8m_e^2}{m_\mu}\right)\left[1 - 1.810\frac{\alpha}{\pi} + (6.701 \pm 0.002)\left(\frac{\alpha}{\pi}\right)^2\right], \tag{1.25}$$

which leads to the numerical value of G_F [4]

$$G_F = 1.1663787(6) \cdot 10^{-5}\text{GeV}^{-2}, \tag{1.26}$$

given the value of the fine structure constant $\alpha^{-1} = 137.03599976(50)$.

Another important EW precision observable (EWPO) is the ratio between the W and Z masses

$$\rho = \frac{m_W^2}{c_W^2 m_Z^2}. \tag{1.27}$$

At leading order, this parameter is equal to unity in the SM. The ρ parameter depends on the representation of the scalar sector of the EW model having ϕ_i scalars with T_i weak isospin and $T_{3,i}$ being its third component, and a vev v_i, via the relation [35, 36]

$$\rho = \frac{\sum_i [T_i(T_i+1) - T_{3,i}^2] v_i^2}{2\sum_i T_{3,i}^2 v_i^2}. \tag{1.28}$$

From (1.28) one can see that a real triplet scalar, for instance, would not fit the experimental EW measurement of ρ. Hence, a complex doublet is the simplest scalar possible for the EW symmetry breaking, and the Higgs boson was expected to be seen almost four decades before its discovery. However, radiative corrections to the EW gauge bosons mass from vacuum polarisation diagrams could potentially cause ρ to deviate significantly from unity. This is not the case, as the experimentally measured value of ρ [4]

$$\rho_{\text{exp}} = 1.00038 \pm 0.00020 \tag{1.29}$$

Additionally, it is possible to think of an extended Higgs sector, where there are multiple scalars with different $SU(2)_L$ multiplicities. Or, a composite Higgs sector, where the Higgs boson is a pseudo Nambu-Goldstone boson, cf. [37, 38]. How can such models be built assuring the ρ parameter is protected from change ? The answer to this question lies in a symmetry of the Higgs Lagrangian known as custodial symmetry.

1.4.1 Custodial symmetry

After SSB, a residual global symmetry known as the custodial symmetry protects the ρ parameter from obtaining large radiative corrections at higher orders in perturbation theory. This symmetry must be kept in extended or composite Higgs models. This symmetry can be seen by rewriting the Higgs potential as

$$V = \frac{\lambda}{4}\left(\phi_1^2 + \phi_2^2 + \phi_3^2 + \phi_4^2 - 2\mu^2\right)^2. \tag{1.30}$$

This potential is invariant under $SO(4) \simeq SU(2)_L \otimes SU(2)_R$ rotations. However, when the Higgs field squires a non-vanishing vev, $\phi_4 \to h + v$, the potential becomes

$$V = \frac{\lambda}{4}\left(\phi_1^2 + \phi_2^2 + \phi_3^2 + h^2 + 2vh + v^2 - 2\mu^2\right)^2, \tag{1.31}$$

which is only invariant under $SO(3) \simeq SU(2)_V$ transformations, the diagonal part of the original group. This global SSB pattern comes alongside the EW SSB of the gauge group $SU(2)_L \otimes U(1)_Y$ as global $SU(2)_L$ is itself the gauged $SU(2)_L$ group. Additionally the T^3 component of the $SU(2)_R$ global group is the gauged $U(1)_Y$ and the T^3 component of the custodial group $SU(2)_V$ is gauged as well and identified to be the electric charge operator, i.e. the generator of $U(1)_Q$.

$$\underbrace{SU(2)_R}_{\supset U(1)_Y} \otimes \overbrace{SU(2)_L}^{\text{gauged}} \longrightarrow \underbrace{SU(2)_V}_{\supset U(1)_Q}. \tag{1.32}$$

This pattern indicates that the symmetry is already broken by the gauging of the diagonal part of $SU(2)_R$ (the hypercharge). The custodial symmetry is only *approximate* in the limit of $g_1 \to 0$, and $\rho = 1$ is a consequence of $g_1 \neq 0$. The symmetry breaking pattern $\mathbf{2} \otimes \mathbf{2} = \mathbf{3} \oplus \mathbf{1}$ also allows us to identify the Goldstone bosons as the custodial triplet and the physical Higgs h as the custodial singlet, explaining the electric charge pattern they have.
We could use the isomorphism between the special orthogonal and special unitary groups to parametrise the Higgs doublet as an $SU(2)_L \otimes SU(2)_R$ bidoublet

$$\mathcal{H} = (\tilde{\phi} \;\; \phi) = \frac{1}{\sqrt{2}}\begin{pmatrix} \phi_4 - i\phi_3 & \phi_1 + i\phi_2 \\ \phi_1 - i\phi_2 & \phi_4 + i\phi_3 \end{pmatrix}, \tag{1.33}$$

with the bi-unitary transformations

$$\mathcal{H} \longrightarrow \mathcal{U}_L \mathcal{H} \mathcal{U}_R^\dagger \tag{1.34}$$

which leaves any traces of the form $\mathrm{Tr}(\mathcal{H}^\dagger\mathcal{H})$, invariant. The Higgs potential could be rewritten in terms of the bidoublet

$$V = -\frac{\mu^2}{2}\mathrm{Tr}(\mathcal{H}^\dagger\mathcal{H} + \frac{\lambda}{4}\left(\mathrm{Tr}(\mathcal{H}^\dagger\mathcal{H}\right)^2 \tag{1.35}$$

The vev is hence written in this representation as

$$\langle\mathcal{H}\rangle = \frac{v}{\sqrt{2}}\,\mathbb{1}_{2\times 2}. \tag{1.36}$$

We can also look at the Yukawa sector, and observe that in the case where $y_u = y_d = y$, we can also write the left-handed and right-handed quarks as $SU(2)_L \otimes SU(2)_R$ bidoublets and $SU(2)_R$ doublets, respectively. Hence, the quark part of the Yukawa Lagrangian in (1.22) becomes

$$\mathcal{L}_{yuk} \supset \frac{y}{\sqrt{2}}(\overline{u}_L \;\; \overline{d}_L) \begin{pmatrix} \phi_4 - i\phi_3 & \phi_1 + i\phi_2 \\ \phi_1 - i\phi_2 & \phi_4 + i\phi_3 \end{pmatrix} \begin{pmatrix} u_R \\ d_R \end{pmatrix}, \tag{1.37}$$

which is invariant under custodial transformations, but when $y_u \neq y_d$, this Lagrangian term breaks custodial symmetry. Thus, the differences between the up-type and down-type quark masses $m_u - m_d$ are considered **spurions** of the custodial symmetry and one expects to see radiative corrections to ρ being proportional to these spurions.

In order to see this more concretely, we start by examining the radiative corrections that could contribute to the deviation of ρ from unity, i.e. $\Delta\rho$ these corrections are known as the **oblique correction**. These oblique corrections come from electroweak vacuum polarisations $\Pi_{VV}(p^2)$, as shown in Figure 1.5, for more details on these corrections and their calculation see Refs.. [39, 40]

The 1-loop correction to the ρ parameter is given in terms of the Π_{VV} by

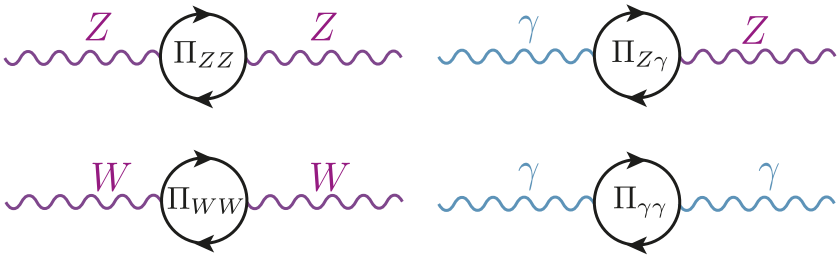

Figure 1.5. The oblique corrections, are radiative correction with electroweak gauge bosons propagators. Namely vacuum polarisations of the Z, $W^{\pm}$ and γ bosons.

$$\Delta\rho = \frac{\Pi_{WW}(0)}{m_W^2} - \frac{\Pi_{ZZ}(0)}{m_Z^2} \tag{1.38}$$

Where the dominant contributions are given by [41]

$$\Delta\rho = \frac{3G_F}{8\sqrt{2}\pi^2}\left((m_t^2 + m_b^2) - \frac{2m_t^2 m_b^2}{m_t^2 - m_b^2}\ln\frac{m_t^2}{m_b^2}\right) + \dots. \tag{1.39}$$

Since $m_b \ll m_t$, the correction is non-vanishing, and (1.39) shows clearly how the radiative corrections are proportional to the spurions of the custodial symmetry. However, this radiative correction is absorbed into the SM definition of ρ, i.e. the $\overline{\text{MS}}$ definition of the ρ-parameter $\rho^{\overline{\text{MS}}}$.

One can study new physics (NP) effects that violates custodial symmetry, by looking at deviations from $\rho = 1$ from it. Given the experimentally measured value of ρ (1.29) many NP models violating custodial symmetry can already be excluded. Nevertheless, ρ alone does not capture the full story of EWPO's. For instance, adding a new quark doublet would not necessarily violate the custodial symmetry though it still can be excluded by EWPO. It is hence useful to introduce new parameters known as **Peskin-Takeuchi parameters** [40, 42, 43]

Peskin-Takeuchi parameters

$$
\begin{aligned}
S &:= \frac{4c_W^2 s_W^2}{\alpha}\left[\frac{\Pi_{ZZ}^{\mathrm{NP}}(m_Z^2)-\Pi_{ZZ}^{\mathrm{NP}}(0)}{m_Z^2} - \frac{c_W^2-s_W^2}{c_W s_W}\frac{\Pi_{Z\gamma}^{\mathrm{NP}}(m_Z^2)}{m_Z^2} - \frac{\Pi_{\gamma\gamma}^{\mathrm{NP}}(m_Z^2)}{m_Z^2}\right], \\
T &:= \frac{\rho^{\overline{\mathrm{MS}}}-1}{\alpha} = \frac{1}{\alpha}\left[\frac{\Pi_{WW}^{\mathrm{NP}}(0)}{m_W^2} - \frac{\Pi_{ZZ}^{\mathrm{NP}}(0)}{m_Z^2}\right], \\
U &:= \frac{4s_W^2}{\alpha}\left[\frac{\Pi_{WW}^{\mathrm{NP}}(m_W^2)-\Pi_{WW}^{\mathrm{NP}}(0)}{m_W^2} - \frac{c_W}{s_W}\frac{\Pi_{Z\gamma}^{\mathrm{NP}}(m_Z^2)}{m_Z^2} - \frac{\Pi_{\gamma\gamma}^{\mathrm{NP}}(m_Z^2)}{m_Z^2}\right] - S.
\end{aligned}
\tag{1.40}
$$

The NP contributions to the EW vacuum polarisations $\Pi_{VV}^{\mathrm{NP}}(p^2)$) could either come from loop or tree-level effects. Typically both T and U are related to custodial symmetry violation. However, U has an extra suppression factor of m_{NP}^2/m_Z^2 compared to T and S. The most recent fit result for these parameters is [4]

$$
\begin{aligned}
S &= -0.01 \pm 0.10, \\
T &= 0.03 \pm 0.13, \\
U &:= 0.02 \pm 0.11.
\end{aligned}
\tag{1.41}
$$

But since T and S tend to give stronger constraint on NP, due to the suppression factor of U. One can preform a two-parameter fit of S and T setting $U = 0$, thas shown in Figure 1.6, with the numerical values [4],

$$
\begin{aligned}
S &= 0.00 \pm 0.07, \\
T &= 0.05 \pm 0.06.
\end{aligned}
\tag{1.42}
$$

The Peskin-Takeuchi parameters are important in constraining effective operators in the Higgs sector , namely

$$
\begin{aligned}
\hat{O}_S &= \phi^\dagger \sigma_i \phi W_{\mu\nu}^i B^{\mu\nu}, \\
\hat{O}_T &= |\phi^\dagger D_\mu \phi|^2.
\end{aligned}
\tag{1.43}
$$

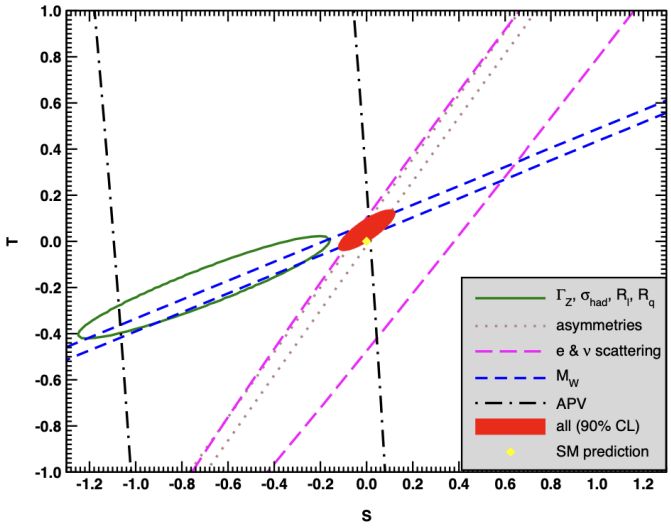

Figure 1.6. Fit results from various EWPO's for T and S setting $U =$. The contours show $1\,\sigma$ contours (39.35% for closed contours and 68% for the rest). This plot is obtained from the PDG [4]

For example, $\hat{O}_S$ appears in Technicolour models causing large deviations of S compared to its measured value [42, 44–46]. Moreover, The constraints on T parameter is important for top mass generation ans well as modifications to $Zb\bar{b}$ coupling in such models [47, 48]. We will revisit the $\hat{O}_T$ when we discuss the Higgs and effective field theories in chapter 3

1.5 Theoretical constraints on the Higgs

1.5.1 Electroweak precision data fits

Even prior to the discovery of the Higgs boson at LHC in 2012, many theoretical aspects of the Higgs sector provided marked bounds on the Higgs properties, particularly it mass. For instance, using the EWPO measurements at LEP provided an input for a fit based of radiative effects coming from the Higgs boson to such observables [11] as in diagram (a) of Figure 1.8, the bounds improved with the improvements of EWPO measurements, these bounds were known as the " blue band" plots seen with their progression in Figure 1.7.

1.5.2 Partial-wave unitarity

Another bound on Higgs mass emerged from studying the amplitudes of EW vector bosons elastic scattering having longitudinal polarisations $V_L V_L \to V_L V_L$ at high energies $E \gg m_W$ (see diagrams (b) in Figure 1.8), where the Goldstone equivalence

theorem holds [49]. This bound comes from applying the partial wave perturbative unitarity on the EW boson scattering amplitude. I will derive here this bound starting from the **Optical theorem**, which a direct result from the unitarity of the **S** matrix.

The optical theorem

Let $\mathcal{M}_{aa}$ be a covariant matrix element for an elastic scattering process with for a particle a then the following relation applies

$$\sum_f \int d\Phi_n(p_a, p_i^f)|\mathcal{M}_{af}|^2 = 2\Im(\mathcal{M}_{aa}), \tag{1.44}$$

where the sum is over all intermediate sates n-particle states f with momenta p_i^f and $d\Phi_n(p_a, p_i^f)$ is the n-particle phase space.

If we only consider a $2 \to 2$ process with momentum states. $|\, p_1, p_2 \,\rangle \to |\, k_1, k_2 \,\rangle$, then (1.44), after expanding the 2-particle phase space , simplifies to

$$\begin{aligned} &\int \frac{d^3k_1}{(2\pi)^3\, 2E_1} \int \frac{d^3k_2}{(2\pi)^3\, 2E_2} (2\pi)^4 \delta^4(p_1 + p_2 - k_1 - k_2)\, |\mathcal{M}(s,t)|^2, \\ &= \frac{1}{16\pi} \int_{-1}^{1} d(\cos\theta) |\mathcal{M}(s,t)|^2, \end{aligned} \tag{1.45}$$

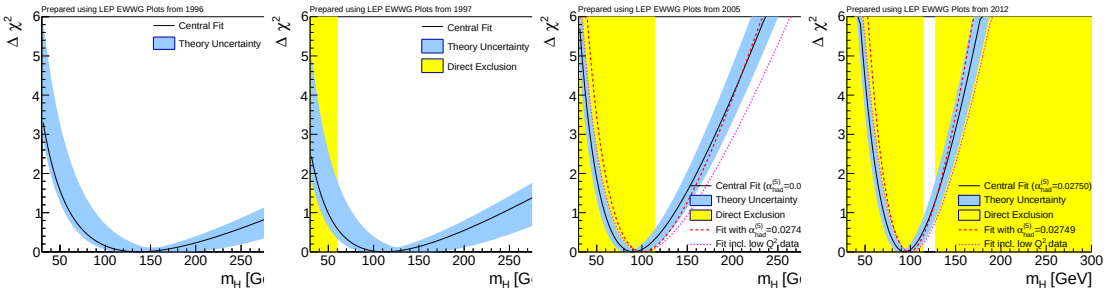

Figure 1.7. Progression of the "blue band" plots with LEP data from 1996 up to 2021 prior to the announcement of the Higgs boson discovery. There plots were taken from [26], based data from LEP [11]

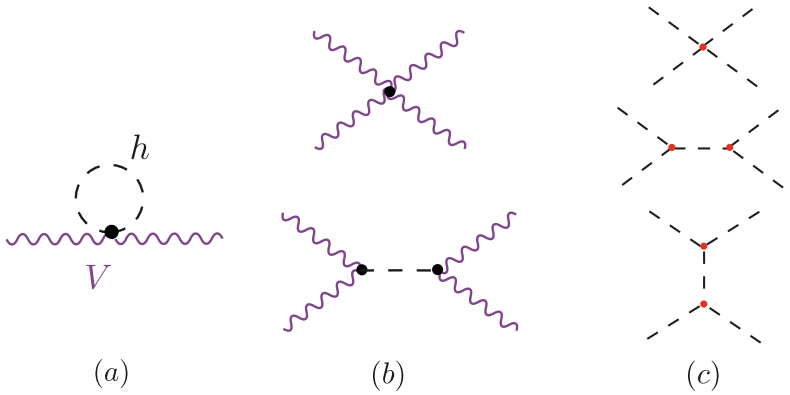

Figure 1.8. Diagrams contributing to theoretical bounds on the Higgs, (a) shows an example of radiative corrections to EWPO from the Higgs bosons. The diagrams in (b) show an elastic scattering of EW vector bosons leading to a bound on the Higgs mass from perturbative unitarity, similarly in (c) diagrams for $hh \to hh$ scattering leading to constraints on Higgs self-coupling.

with the Mandelstam variables

$$\begin{aligned} s =& k_1 + k_2, \\ t =& k_1 - p_1, \\ u =& k_1 - p_2, \\ s + t + u =& 4m^2 \end{aligned} \tag{1.46}$$

Recall that the relation between the Mandelstam variable t, and the scattering angle for the elastic scattering is given by

$$t = \frac{1}{2}(s - 4m^2)(\cos\theta - 1) \tag{1.47}$$

We could expand the matrix element $\mathcal{M}(s,t)$ in terms of *partial waves*, isolating s from scattering angle dependence

$$\mathcal{M}(s,t) = 16\pi \sum_j (2j+1) a_j P_j(\cos\theta). \tag{1.48}$$

Where a_j are called the jth partial wave amplitude, and $P_j(\cos\theta)$ are the Legendre polynomials

$$P_j(z) = \frac{1}{j!}\frac{1}{2^j}\frac{d^j}{dz^j}(z^2-1)^j \tag{1.49}$$

Which satisfies the orthonormality condition

$$\int_{-1}^{1} dz\, P_j(z) P_k(z) = \frac{1}{2j+1}\delta_{jk} \tag{1.50a}$$

$$P_j(1) = 1 \;\; \forall j. \tag{1.50b}$$

We hence get for the LHS of (1.44) scattering

$$\begin{aligned}
&\int \frac{d^3k_1}{(2\pi)^3\, 2E_1} \int \frac{d^3k_2}{(2\pi)^3\, 2E_2} (2\pi)^4 \delta^4(p_1 + p_2 - k_1 - k_2)\, |\mathcal{M}(s,t)|^2, \\
&= \frac{1}{16\pi} \int_{-1}^{1} d(\cos\theta) \left[16\pi \sum_j (2j+1) a_j(s) P_j(\cos\theta) \right] \times \\
&\qquad \left[16\pi \sum_k (2k+1) a_k^*(s) P_k(\cos\theta) \right], \\
&\Rightarrow = 32\pi \sum_j (2j+1) |a_j(s)|^2.
\end{aligned} \tag{1.51}$$

And the RHS of (1.44)

$$2\mathfrak{I}(\mathcal{M}_{aa}) = \underbrace{2\mathfrak{I}(\mathcal{M}(s,0))}_{t \text{ is integrated out.}} = 32\pi \sum_j (2j+1) \mathfrak{I}(a_j(s)). \tag{1.52}$$

Otherwise large cancellations needed, $a_j(s)$'s are hierarchal. Thus, we could compare the partial wave amplitudes term-by-term

$$|a_j(s)|^2 \leq \mathfrak{I}(a_j(s)) \quad \Rightarrow \mathfrak{R}(a_j(s))^2 + \mathfrak{I}(a_j(s))^2 \leq \mathfrak{I}(a_j(s)) \tag{1.53}$$

Rearranging terms, we get

$$\mathfrak{R}(a_j(s)) + \left(\mathfrak{I}(a_j(s)) - \frac{1}{2} \right)^2 \leq \frac{1}{4} \tag{1.54}$$

The partial wave amplitude has to lie within the unitarity circle. We use though perturbation theory if the partial wave amplitude respects the inequality

$$\mathfrak{R}(a_j(s)) \leq \frac{1}{2} \tag{1.55}$$

This is known as the perturbative partial wave unitarity bound.
When (1.55) is applied for $V_L V_L \to V_L V_L$, in the Goldstone boson equivalence theorem

regime in particular for $V = W$ boson, we get for the S-wave partial amplitude

$$a_0 \sim \frac{m_h^2}{16\pi v^2}\left(2 + \mathcal{O}\left(m_h^2/s\right)\right). \tag{1.56}$$

Looking at the asymptotic behaviour as $s \to \infty$, we obtain the bound

$$\frac{m_h^2}{8\pi v^2} < \frac{1}{2} \Leftrightarrow m_h \leq 870\,\text{GeV}. \tag{1.57}$$

Indeed this bound is obsolete now after th Higgs mass measurement, however it is very important to demonstrate the power of this technique in constraining Higgs parameters. As this method can be applied to any elastic scattering with the Higgs acts as a mediator like $ZZ \to ZZ, WW \to ff$ and constrain the correspong couplings $g_{ZZh}, g_{f\bar{f}h}$ and so on. An important bound can be derived by examining the Higgs elastic scattering $hh \to hh$ shown in (c) of Figure 1.8 in order to set bounds on Higgs self-interactions g_{hhh} and g_{hhhh}. This is what exactly has been done in ref. [50] where they have found that the S-wave partial amplitude for this process is given by

$$a_0 = -\frac{1}{2}\frac{\sqrt{s(s-4m_h^2)}}{16\pi s}\left[g_{hhh}^2\left(\frac{1}{s-m_h^2} - 2\frac{\log\frac{s-3m_h^2}{m_h^2}}{s-4m_h^2}\right) + g_{hhhh}\right], \tag{1.58}$$

which leads to unitarity bounds on the trilinear g_{hhh} and the quartic g_{hhhh} couplings

$$\left|g_{hhh}/g_{hhh}^{\text{SM}}\right| \lesssim 6.5 \qquad \text{and} \qquad \left|g_{hhhh}/g_{hhhh}^{\text{SM}}\right| \lesssim 65\,. \tag{1.59}$$

A stringer constrained can be obtained by looking at the one-loop correction to the $hh \to hh$ scattering amplitude, within the full kinematic range. The unitarity bound here is obtained by looking at the one-loop amplitude at the threshold, and is given by

$$\left|g_{hhh}/g_{hhh}^{\text{SM}}\right| \lesssim 6\,. \tag{1.60}$$

These bounds are, hitherto, the strongest on these two couplings even when compared to the ones coming from current experimental searches.

1.5.3 Other bounds

Further theoretical bounds could be obtained by studying quantum effects on the Higgs potential. For example, if we looked at the solution of the renormalisation group equation (RGE) for the Higgs self-coupling λ with the boundary condition $\lambda(v) = \lambda_0$ and

ignoring other SM particle-contributions

$$\lambda(Q^2) = \frac{\lambda_0}{1 - \frac{3}{4\pi^2}\log\frac{Q^2}{v^2}} \tag{1.61}$$

We see that the running of λ will hit a pole, known as **Landau pole** when the denominator vanishes. This will happen at the scale

$$Q_c = ve^{4\pi^2/3\lambda_0} = ve^{4\pi^2 v^2/3m_h^2} \tag{1.62}$$

This indicates that the theory will break down at scales larger or equal to Q_c. Since the "critical scale" is a function of the Higgs mass, this allows us to set an upper limit on the Higgs mass assuming the SM will be valid up to a certain scale Q_c. This bound is known as **quantum triviality** bound [51]. This is because the low energy behaviour of (1.61) leads to a vanishing interaction, and if we want the Higgs Lagrangian to bee perturbative for all scales, then λ has to be vanishing and the theory becomes non-interacting or *trivial*.

Another bound coming from the RGE of λ is the **stability bound** , which considers the stability of the Higgs potential given the running of λ by requiring that the Higgs potential is an operator bounded from below. This bound is obtained by approximating the solution of the RGE at small λ

$$\lambda(Q^2) \sim \lambda_0 + \frac{1}{16\pi^2}\left[-\frac{12m_t^4}{v^4} + \frac{3}{16}\left(2g_2^4 + (g_2^2 + g_1^2)^2\right)\right]\log\frac{Q^2}{v^2} \tag{1.63}$$

For the Higgs potential to be bounded from below $\lambda(Q^2)$ ought to be $\lambda(Q^2) > 0$. With th relation for λ_0 in terms of the mass, we get a bound on m_h

$$m_h^2 > \frac{v^2}{8\pi^2}\left[-\frac{12m_t^4}{v^4} + \frac{3}{16}\left(2g_2^4 + (g_2^2 + g_1^2)^2\right)\right]\log\frac{Q^2}{v^2} \tag{1.64}$$

Which leads to $m_h \approx 130$ GeV if we assume that the SM is valid up to the Grand Unified Theory (GUT) scale of $\sim 10^{16}$ GeV and $m_h \approx 180$ GeV for Q being at the Planck scale $\sim 10^{19}$ GeV.

More sophisticated calculations and discussion for the Higgs potential and vacuum stability has been a subject of great interest in pre and post-Higgs discovery eras cf. [51–54] and the most state-of-the-art calculation for the vacuum stability at NNLO has been preformed in ref. [55] where they also included finite temperature effects to construct a phase diagram in the $m_t - m_h$ and $m_t - \lambda(M_{pl})$ planes as shown in Figure 1.9. Indicating that the measured Higgs mass in likely compatible with a metastable vacuum rather than absolute stability. This indicates that there is a finite probability for the Higgs vacuum (false vacuum) to decay into a lower energy state (true vacuum) via quantum tunnelling.

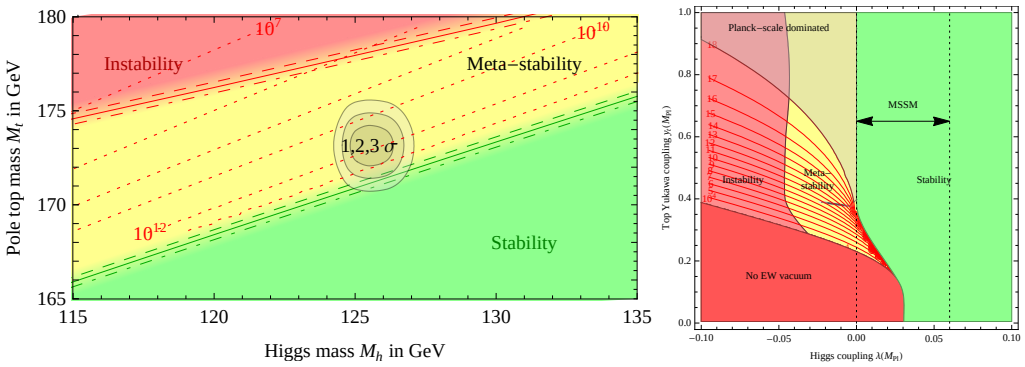

Figure 1.9. Phase diagrams of the Higgs vacuum in the $m_t - m_h$ (left) and $m_t - \lambda(M_{pl})$ (right) planes showing areas of instability, meta stability and absolute stability. In the $m_t - \lambda(M_{pl})$ diagram, the allowed range of the Higgs self-coupling λ in the Minimal Supersymmetric SM (MSSM), this plot is taken from [55]

2 Experimental measurements of the Higgs boson

The observation of the Higgs boson, then the extensive measurement of its properties and couplings has been on the top of the LHC programme priorities [56]. In the time this thesis was in the writing, the particle physics community will be celebrating a decade since the Higgs boson's discovery. Looking back 10 years ago, when I have witnessed the discovery of the Higgs boson via news press-conference in summer of 2012, and decided to be a part of this enormous step that humanity has taken, I feel astonished by the progress made in understanding this newly discovered particle!
In this chapter, I will start by an overview of the extraordinary LHC and its experiments in section 2.1. Then, I will review the state-of-the-art status of experimental measurements of the Higgs properties in section 2.2, cross-sections and couplings in section 2.3, and at the end I will discuss the challenges and outlook for the future runs of the LHC section 2.4, of which the of the rest of this thesis is going to be aim address a small part of them.

2.1 Overview of the Large Hadron Collider

The Large Hadron Collider (LHC) is the largest particle accelerator in the CERN accelerators complex, with a circumference of about 26 km,with over 9590 superconducting magnets cooled to 1.9 K. It was built as an upgrade to the Large electron positron collider (LEP) which ended its operation in the year 2000. The LHC contains four main experiments situated at the four beam collision points and detectors, and these experiments are: ATLAS, CMS, LHCb and ALICE, there also smaller experiments such as LHCf, MilliQan,TOTEM and others. For more details about the LHC cf. [57, 58] or see the LHC technical design report [59] for more technical details.
The LHC started operation in September of 2008, with low energy proton beams, then gradually increased to an energy of 3.5 TeV per proton to reach a centre of mass energy $\sqrt{s}$ of 7 TeV, and data-taking period started from 2011 . By 2012, its energy has increased to $\sqrt{s} = 8$ TeV and operated at this energy for about year and half, then stopping in mid 2013 concluding what is known as **Run-I**. In 2015, the **Run-II** started with almost double the energy $\sqrt{s} = 13$ TeV, and lasted for ca. 3 years. As this thesis being written, preparations are being made to get **Run-III** started until 2024. During these runs, heavier nuclei such as $^{207}\mathbf{Pb}$ and $^{131}\mathbf{Xe}$ have been collided either with protons or

with themselves [60].
From, 2025 and beyond, the **High-Luminosity** LHC (HL-LHC) era will commence, see Figure 2.2. Where the LHC will be shutdown for extensive upgrades [61] to potentially increase its energy to $\sqrt{s} = 14$ TeV and higher collision rates hence the term *high luminosity*. Which leads us to an important notion in particle physics phenomenology *integrated luminosity*.

The performance of colliders depends on many factors, but for phenomenological studies, like this thesis, one mainly considers the centre of mass energy $\sqrt{s}$ and the integrated luminosity $\mathscr{L}$. This is mainly due to the fact that particle colliders experiments are basically "counting experiments", and all of the bounds on physical observables or model parameters are obtained from the number of signal versus background events, and the number of expected events N_{expec} for a given resonance R and a subsequent decay final state X at any collider experiments is given by

$$N_{expec} = \sigma(pp \to R)\, \mathcal{B}(R \to X)\, \mathscr{L}\, \epsilon_{\text{SEL}}. \tag{2.1}$$

Here ϵ_{SEL} is the selection efficiency, which depends on many factors like the detector geometry and particle identification performance etc. , as well as the signal one searches for, it can be improved by better detected or selection cuts. The production cross-section increases typically with quadratically with $\sqrt{s}$, hence comes the need for higher energies but this can only achieved by building new colliders from scratch. The integrated luminosity can be increased much more easily, by longer running time of the same collider as it is the time integral of the collider's luminosity $L(t)$ over its operation time T

$$\mathscr{L} = \int^{T} L(t). \tag{2.2}$$

Therefore, we see that the integrated luminosity for the LHC experiments will increase over time, when more collisions taking place, as seen in figure Figure 2.1 showing the integrated luminosity for ATLAS and CMS experiments. As thee protons travel in the LHC in **bunches**, and as these bunches cross, protons collide at a certain frequency f, when two bunches with N_1 and N_2 protons per bunch, respectively. Each bunch will have an effective cross-section $4\pi\sigma_i$ corresponding to their physical sizes $\sigma \sim 16\,\mu\text{m}$, the luminosity is therefore given -approximately- by

$$L = \frac{f N_1 N_2}{4\pi\sigma_1\sigma_2}, \tag{2.3}$$

which is for the LHC averages to about 10^{34} collisions $\text{cm}^{-2}\,\text{s}^{-1}$ [62, 63].
The total physics-viable *pp*-collisions integrated luminosity for Run-I was 4.57 /fb for 7 TeV and 20.3 /fb for 8 TeV (ATLAS [64]) and 5.55 /fb at 7 TeV and 21.8 /fb at 8 TeV

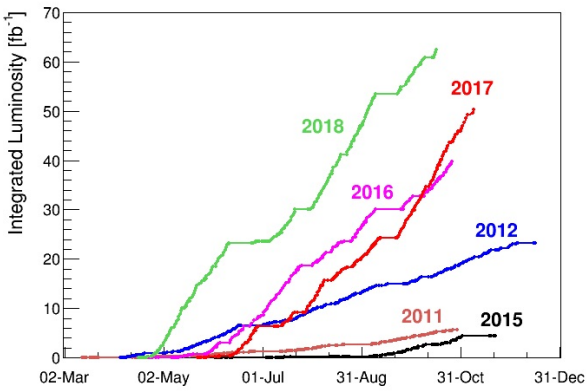

Figure 2.1. The integrated luminosity of the CMS and ATLAS experiments combined over the period from 2011-2018, source [62].

(CMS [65]). As for Run-II the integrated luminosity is 139 /fb at 13 TeV (ATLAS [66]) and 137 /fb at 13 TeV (CMS [65]). The expected integrated luminosity by the end of Run-III is 300 /fb [67] and 3000 /fb by the end of the HL-LHC at energy of 14 TeV [61].

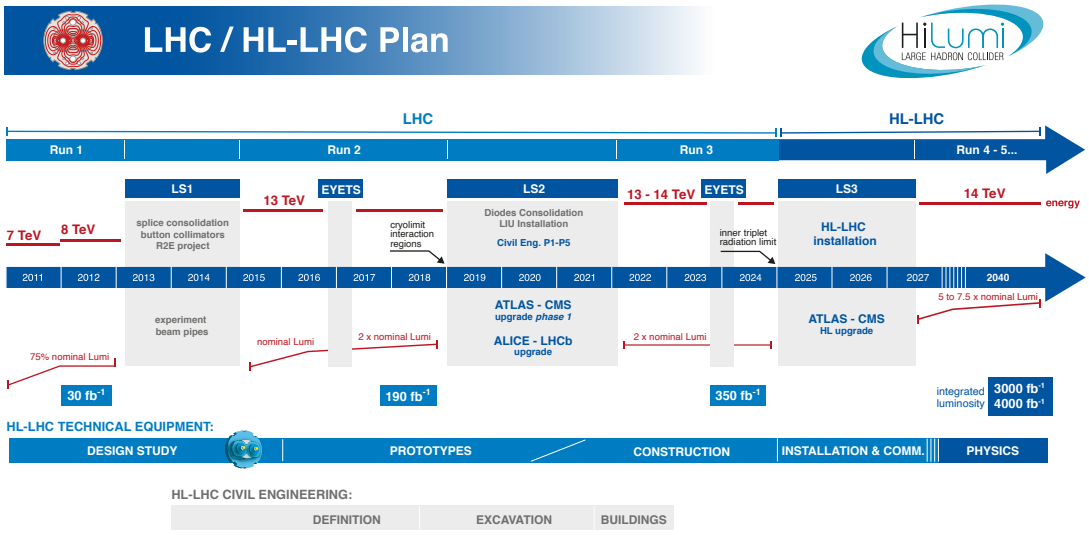

Figure 2.2. A timeline of the LHC operation showing Run-I, Run-II and future planned runs of the LHC, including the HL-LHC, source [60].

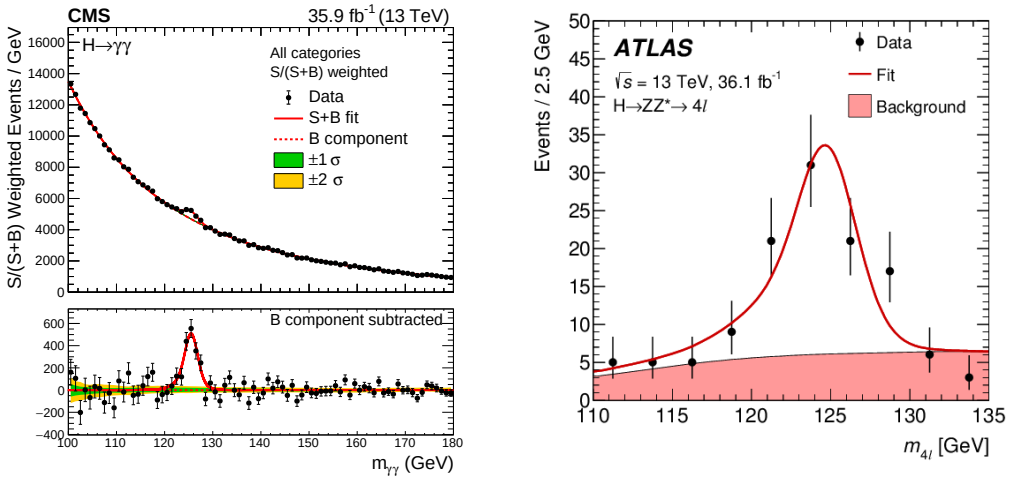

Figure 2.3. The invariant mass distributions of diphoton $m_{\gamma\gamma}$ (CMS [68]) and four lepton $m_{4\ell}$ (ATLAS [69]) final states showing a clear peak at the Higgs mass, with smooth background. These final states are ideal for Higgs mass measurements.

2.2 Higgs properties

2.2.1 Higgs boson mass measurements

In order to measure the mass of thee Higgs boson with high precision, one need to consider final states that can be reconstructed with high momentum and mass resolution, this is typically achieved when no hadronic constituents in the decays involved, such as $h \to \gamma\gamma$ and $h \to ZZ^* \to 4\ell$. Reconstructing the invariant mass distributions $m_{\gamma\gamma}$ and $m_{4\ell}$ one observes that the Higgs peak is narrow over a relatively smooth background, see Figure 2.3, which is ideal for the measurement of the Higgs mass. It should be noted that the width of the resonance is due to the detector resolution and does not correspond to the actual Higgs width.

There have been consistent improvements of the Higgs mass measurements since its discovery. In Figure 2.4 I have preformed a meta analysis on ATLAS and CMS measurements of the Higgs mass in Run-I and Run-II of the LHC for both diphoton and ZZ^* final states based on the data from the studies [68–71] using a random effects model [72]. The pooling of the studies yielded a mass measurement of $m_h = 125.21 \pm 0.10$, which translates to a 0.11% accuracy, the heterogeneity off the studies was found to be $I^2 = 49\%$ ($p = 0.05$) . Different measurements combination techniques were used in [68] and [4] yielded different central values but all of the results agree within the uncertainties.

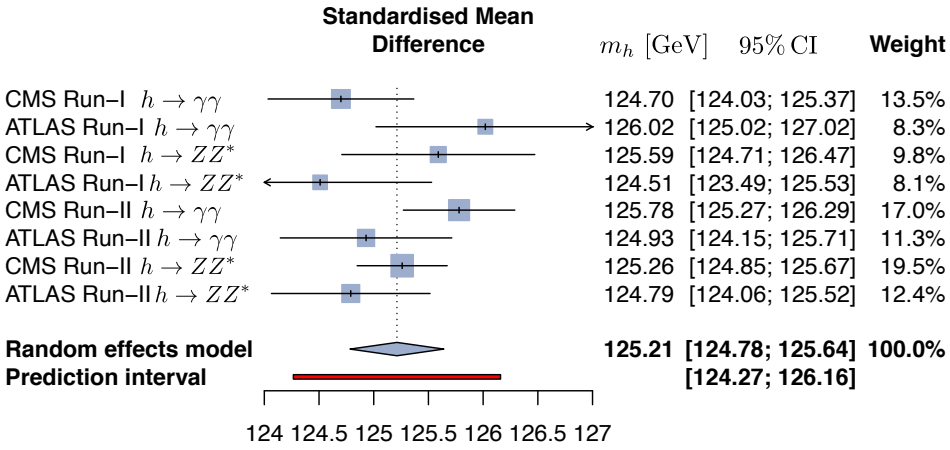

Figure 2.4. A meta analysis preformed to combine all the measurements of the Higgs mass from Run-I and Run-II, the combined result was obtained from pooling all of the studies using the random effects model method.

2.2.2 Higgs full width

The SM values of the Higgs boson full width is $\Gamma_h = 4.1$ GeV and it can be accessed in the LHC by looking at the ratio of on-shell versus off-shell Higgs production and decay to the $ZZ^{(*)}$ state, and $ZZ^{(*)} \to 4\ell, 2\ell 2\nu$, namely

$$\frac{\sigma(gg \to h \to ZZ^*)}{\sigma(gg \to h^* \to ZZ)} = \kappa_g^2 \kappa_Z^2 \frac{4m_Z^2}{m_h \Gamma_h}, \tag{2.4}$$

where the κ here denote the ratio between the measured/ or modified coupling with the Higgs and the SM prediction, i.e.

$$\kappa_X := \frac{g_{XXh}}{g_{XXh}^{\text{SM}}}. \tag{2.5}$$

Which is commonly used in reporting experimental constrains/ measurements of the Higgs couplings, as in the next section section 2.3. We shall discuss the κ formalism more in chapter 3.
We see from (2.4) that if one fixes the coupling between the gluons and the Z boson and the Higgs it is possible to access the full width directly. Unfortunately, it is not possible to directly measure the Higgs full width at the LHC, as this requires full reconstruction of the collision event and study the recoil mass which is only possible at lepton colliders [73, 74]. Alas, it is still possible to extract bounds on Γ_h using (2.4). ATLAS used this method to constrain the full width of the Higgs using Run-II data [75], while CMS has preformed the same analysis using Run-I and Run-II data combined [76], the results are 95% CL bounds of Γ_h

$$\Gamma_h < 14.4\,\text{GeV} \quad \text{(ATLAS)} \qquad 0.08\,\text{GeV} < \Gamma_h < 9.16\,\text{GeV} \quad \text{(CMS)}, \tag{2.6}$$

with the combined bound being $\sim 3\Gamma_h^{\text{SM}}$.

2.2.3 Higgs spin and parity

As we have seen in section 1.2, the Higgs boson in a scalar and $\mathcal{CP}$ even ($J^p = 0^+$) in the SM. However, the discovery of a peak in the $m_\gamma\gamma$ distribution, would not automatically imply that the particle discovered is scalar, it could be a spin-2 boson, or a pseudoscalar ($J^p = 0^-$). In order to study the J^p properties of the Higgs, one needs to examine the differential distributions of angular variables such as rapidity y or transverse momentum p_T. Both ATLAS and CMS collaborations studied using Run-I data the angular distributions of the Higgs decays $h \to ZZ^*$, $h \to WW^*$ and $h \to \gamma$, to study an anomalous VVh coupling. Then test the alternative hypothesis for J^p against the SM [77, 78]. The analysis results show that the SM 0^+ hypothesis is favoured at $> 99.9\%$ CL.

2.3 Measurements of Higgs rates and couplings

2.3.1 Higgs cross-sections

The total inclusive Higgs cross-section has been measured using the the final states $h \to \gamma\gamma$ and $h \to ZZ^* \to 4\ell$. and their combinations. The measurements has been done at the three energies the LHC was operating at: 7 TeV, 8 TeV [79] and 13 TeV [80–82] and combined with more data and compared to the SM prediction as show in [83]. As shown in Figure 2.5, the measured inclusive cross-section is in agreement with the SM prediction across al of the LHC operation energies.

In addition to the inclusive cross-section measurements, differential cross-sections of the Higgs has been measured for p_T and y as we have seen in subsection 2.2.3 for Higgs's J^p determination. Additional, the differential cross-sections for other variables have

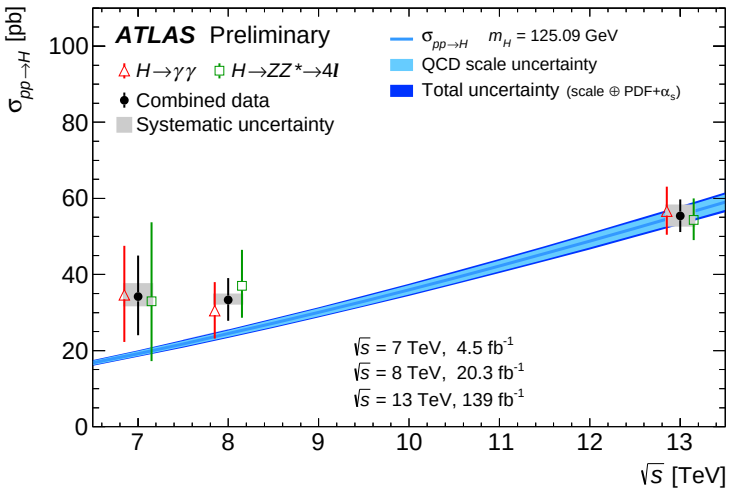

Figure 2.5. The total inclusive cross-section measurements by ATLAS collaboration [83] for 7, 8 and 13 TeV using $h \to \gamma\gamma$ and $h \to ZZ^* \to 4\ell$. channels and their combination (black points) compared to the SM prediction with the uncertainties shown as blue line with light and dark blue bands for QCD scale uncertainties and total uncertainties, respectively.

been measured, and they include $N_{jets}, p_T^{jet}, m_{jj}, \delta\phi_{jj}]$ and others using the channels $h \to ZZ^*$, $h \to WW^*$ and $h \to \gamma$. The most recent results using the full Run-II data can be found in Refs. [81, 83–85].

In addition to the total inclusive cross-section, a collection of measurements of Higgs production and decay rates has been carried out by both ATLAS and CMS. These measurements also carried out in , what is known as Standard Template Cross-Sections (STXS) framework.The STXS's are fiducial cross-sections in exclusive phase-space regions or bins separately per Higgs boson production channel. They have the advantage of standardisation of cuts and final results such that measurements could be easily combined across analyses. More details about the STXS framework can be found in the reports of LHC Higgs cross-sections working group (LHCHXSWG) cf. [86]. In Table 2.1 I summarise the state-of-art measurements of the Higgs rates separated into production and decay channels using the total LHC Run-II data from ATLAS and CMS experiments. Additionally, I give the HL-LHC projections from CMS experiment as a comparison. The results in this table are written in terms of the signal strength, which is directly extracted from measuring the number of events dividing them by the standard model,

$$\mu_{\text{Exp}} := \frac{\sigma \cdot \mathcal{B}}{\sigma^{\text{SM}} \cdot \mathcal{B}^{\text{SM}}}. \tag{2.7}$$

Production	Decay	$\mu_{\text{Exp}} \pm \delta\mu_{\text{Exp}}$ (symmetrised) **LHC Run-II** CMS 137 fb^{-1} / ATLAS 139 fb^{-1}	**HL-LHC** CMS 3 ab^{-1}	Ref.
ggF	$h \to \gamma\gamma$	0.99 ± 0.12 1.030 ± 0.110	1.000 ± 0.042	[87–89]
	$h \to ZZ^*$	0.985 ± 0.115 0.945 ± 0.105	1.000 ± 0.040	[87, 89, 90]
	$h \to WW^*$	1.285 ± 0.195 1.085 ± 0.185	1.000 ± 0.037	
	$h \to \tau^+\tau^-$	0.385 ± 0.385 1.045 ± 0.575	1.000 ± 0.055	
	$h \to b\bar{b}$	2.54 ± 2.44 –	1.000 ± 0.247	[89, 90]
	$h \to \mu^+\mu^-$	0.315 ± 1.815 –	1.000 ± 0.138	[89, 90]
VBF	$h \to \gamma\gamma$	1.175 ± 0.335 1.325 ± 0.245	1.000 ± 0.128	[87–89]
	$h \to ZZ^*$	0.62 ± 0.41 1.295 ± 0.455	1.000 ± 0.134	[87, 89, 90]
	$h \to WW^*$	0.65 ± 0.63 0.61 ± 0.35	1.000 ± 0.073	
	$h \to \tau^+\tau^-$	1.055 ± 0.295 1.17 ± 0.55	1.000 ± 0.044	
	$h \to b\bar{b}$	– 3.055 ± 1.645	–	[87]
	$h \to \mu^+\mu^-$	3.325 ± 8.075 –	1.000 ± 0.540	[89]
$t\bar{t}h$	$h \to \gamma\gamma$	1.43 ± 0.30 0.915 ± 0.255	1.000 ± 0.094	[87–89]
	$h \to VV^*$	$0.64 \pm 0.64 (ZZ^*)$ 0.945 ± 0.465 (WW^*) 1.735 ± 0.545	1.000 ± 0.246 (ZZ^*) 1.000 ± 0.097 (WW^*) –	[87, 89, 90]
	$h \to \tau^+\tau^-$	0.845 ± 0.705 1.27 ± 1.0	1.000 ± 0.149	
	$h \to b\bar{b}$	1.145 ± 0.315 0.795 ± 0.595	1.000 ± 0.116	
Vh	$h \to \gamma\gamma$	0.725 ± 0.295 1.335 ± 0.315	1.000 ± 0.233 (Zh) 1.000 ± 0.139 ($W^\pm h$)	[87–89]
	$h \to ZZ^*$	1.21 ± 0.85 1.635 ± 1.025	1.000 ± 0.786 (Zh) 1.000 ± 0.478 ($W^\pm h$)	[87, 89, 90]
	$h \to WW^*$	1.850 ± 0.438 –	1.000 ± 0.184 (Zh) 1.000 ± 0.138 ($W^\pm h$)	[89, 91]
	$h \to b\bar{b}$	– 1.025 ± 0.175	1.000 ± 0.065 (Zh) 1.000 ± 0.094 ($W^\pm h$)	[87, 89]
Zh CMS	$h \to \tau^+\tau^-$ $h \to b\bar{b}$	1.645 ± 1.485 0.94 ± 0.32	–	[90]
$W^\pm h$ CMS	$h \to \tau^+\tau^-$ $h \to b\bar{b}$	3.08 ± 1.58 1.28 ± 0.41		

Table 2.1. The experimental single Higgs production and decay rates measurements from the complete data of LHC Run II and projections for the HL-LHC. The uncertainties were symmetrised here.

2.3.2 Constraints on Higgs couplings

The measurements of the Higgs rates and their combination (also including STXS) have been used to set bounds on the Higgs couplings, the most recent bounds - as this thesis being written - have been reported by ATLAS using the Higgs inclusive rates and STXS for the full Run-II data [92], and by CMS using Higgs rates shown in Table 2.1 [90]. In Figure 2.6, I present the aggregation the ATLAS and CMS bounds on the Higgs coupling modifiers in the κ formalism defined in eq. (2.5). The aggregation of these bounds was preformed using the method described in [93] assuming there is no correlation between ATLAS and CMS measurements.

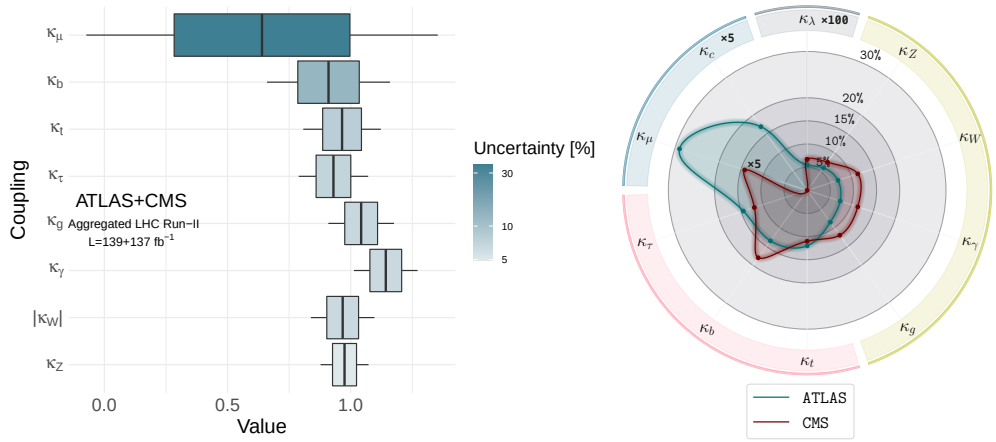

Figure 2.6. Meta analysis aggravating the most recent bounds from ATLAS [92] and CMS [90] on the Higgs couplings modifiers κ. update the fig

Examining Figure 2.6, we observe that the bounds on the Higgs boson's coupling to the gauge boson, including the effective couplings to γ and g, as well as the couplings to the third-generation fermions are in few percent within the SM prediction. The bounds on the coupling to the W boson seems to favour a negative value in CMS fits, due to the channel used to constraint it $h \to WW$ which depends on κ_W^2, thus making the best fit value of ~ -1 within the SM prediction. An independent analysis on the relative signs of κ_W and κ_t was preformed using $th/t\bar{t}h$ processes in Ref. [94], hence only the absolute value of κ_W is reported in my combination of the analysis results. Additionally, the observation of the decays $h \to b\bar{b}$ [95–97] and $h \to \tau\tau$ [98, 99] leading to direct measurements of the beauty and τ Yukawa couplings has made their bounds comparable to the gauge bosons and top couplings with the Higgs, having less than 10% uncertainty. Au contraire, bounds on the Yukawa couplings of second and first generation fermions remain very weak.

Recently, searches for the decay $h \to \mu\mu$ [100, 101] using the whole Run-II data by

both collaborations, yielded an evidence fr its observation of about 3σ. Improving the constraints on κ_μ, though as seen in Figure 2.6, the uncertainty remains high $\sim 36\%$. Searches for the Higgs decaying to charm pairs is significantly more challenging than the dimuon decays and only yielded an upper 95% CL bounds on $|\kappa_c|$ of 8.5 for ATLAS [102] and 70 for CMS [103]. There is no planned direct searches for the first generation Yukawa couplings (*direct*) measurements planned for the LHC as it is not possible to directly access decays of the Higgs to up or down quarks. Other methods for probing these couplings will be extensively discussed in **??**.

By the end of the HL-LHC, it is projected that the couplings of the Higgs, including the couplings with gauge bosons, third generation fermions as well as the muon Yukawa will be measured at few percent level, particularly the couplings with the gauge bosons will be reaching $\sim 1\%$ level uncertainty [104]. This is highlighted by Figure 2.7, this figure shows the improvement in the κ measurement uncertainty expected by the HL-LHC over Run-II.

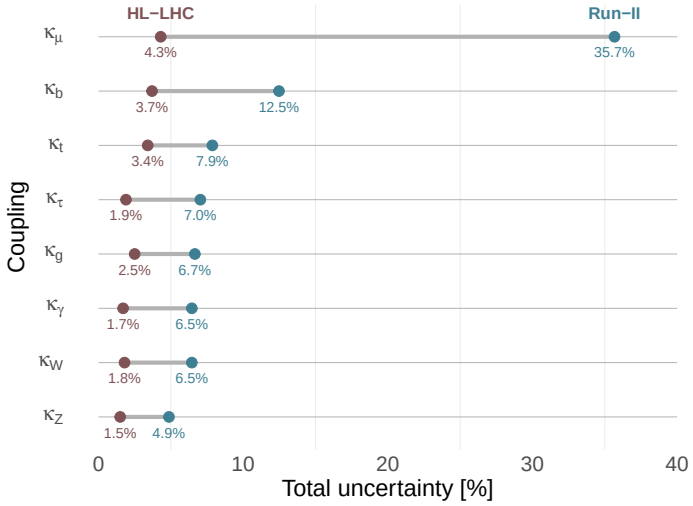

Figure 2.7. *How much the HL-LHC is projected to improve Higgs couplings' measurement?* The combining ATLAS and CMS projections

2.4 Challenges and outlook

The future runs of the LHC hold a lot of potential for further understanding of the 10-year old Higgs boson ! Although, for some processes and couplings there will still be a lot of challenges. For instance, the observation of $h \to c\bar{c}$ will require highly efficient charm-tagging, which is expected to improve at the HL-LHC by a factor of 2.5 [105].

The signal strength with rare decay $h \to Z\gamma$ currently is constrained to 3.6 times the SM values at 95% CL [106] and it is projected to be measured at the HL-LHC with $\sim 10\%$ uncertainty.

One of the couplings of the Higgs which we did not discuss above is the Higgs self-interaction (trilinear and quartic), as I have shown in subsection 1.5.2 that the perturbative unitarity bound derived in Ref. [50] is the strongest bound on these couplings so far. This is due to the fact that to experimentally measure the Higgs self-coupling, one needs to search for double Higgs production to access the trilinear self-coupling, and triple Higgs production for the quartic. These processes are very challenging, due to their low inclusive cross-section ~ 30 fb for hh [107] and < 0.1 fb for hhh at LHC maximum expected operational energy of 14 TeV and the latter is challenging even for future colliders of inclusive cross section at 100 TeV of only ~ 5 fb [108]; as opposed to single Higgs production with inclusive cross-section of ~ 70 pb. Certainly the difficulty is aggrivated when one considers that the second Higgs would also decay, further lowering the signal strength. The triple Higgs production thus, will not be accessable at the LHC and consequently the quartic self-coupling. However, there is a lot of potential for the trilinear self-coupling, particularly at the HL-LHC.

In chapter 5 I will discuss the potential for using single Higgs processes as proposed by several studies, cf. [109–116] and the challenges accompanying it. Later in **??** the Higgs pair production at the LHC will be overviewed along the current and future searches for this process and the bounds from them on the trilinear Higgs self-coupling.

Another elusive couplings that we have came across are the light Yukawas. In particular light quark Yukawa couplings of the first generation. After overviewing the proposed methods for constraining them, in **??** I will discuss a novel method for directly measuring light quark Yukawa coupling using Higgs pair production. And in **??** a sophisticated method based on interpretable machine learning will be showcased, by which, it is possible to simultaneously constrain the two elusive Higgs interactions: light Yukawas and the trilinear self-coupling using Higgs pair production !

3 Higgs and effective field theories

The study of the Higgs properties, couplings and rates aims to shed light on the structure of its potential, how and why it is responsible for the EW symmetry breaking. Explaining the vacuum expectation value and the mass of the Higgs has been the aim of many theoreticians and phenomenologists. This is because the SM provides no insights on the nature of the Higgs potential, and its parameters, as these are an input parameters that needed to be provided from experimental observations. The Higgs potential shown in eq. (1.8) is the minimal one that could cause the EW symmetry breaking, but nature may not have taken this minimalist approach. In particular, that this potential suffers from severe fine-tuning as we have discussed in the hierarchy problem add a discussion about this.

In order to test whether the Higgs potential and the way it generates SSB is the minimalist SM way or there are other more complex structures involved one needs to measure Higgs rates and compare them with the SM, as overviewed in the previous chapter, using the κ formalism. Alas, this approach does not help in understanding what would the new physics (NP) structures be more likely to case a certain deviation, if any observed. Conversely, we would be interested in knowing what the allowed NP structures given the current (or future) measurements of the Higgs rates are. Of course, by looking at concrete models, one-by-one, confronting them with Higgs data one would get an insight on the aforementioned questions but withal very tedious as there are numerous ways NP might manifest.

In order to make our search for NP more accessible and model-agnostic, we could revert to **effective field theories** (EFT), one of the most perspicacious concepts of quantum field theory.

If the new BSM degrees of freedom are much heavier than the electroweak scale, a general description of potential new physics effects can be formulated in the language of an effective field theory (EFT). One possibility of such a parameterization is the so-called Standard Model EFT (SMEFT), in which new physics effects are given in terms of higher-dimensional operators involving only SM fields and that also respect the SM gauge symmetries. The dominant effects on Higgs physics, electroweak physics and top quark physics stem from dimension-six operators, suppressed by the new physics scale Λ. This approach is justified in the limit in which energy scales $E \ll \Lambda$ are probed.

In the presence of a gap between the electroweak scale and the scale of new physics, Λ, the effect of new particles below the new physics scale can be described by an EFT. In the case of the SMEFT, the SM Lagrangian is extended by a tower of higher-dimensional

operators, $\mathcal{O}_i$, built using the SM symmetries and fields (with the Higgs field belonging to an $SU(2)_L$ doublet), and whose interaction strength is controlled by Wilson coefficients, C_i, suppressed by the corresponding inverse power of Λ. In a theory where baryon and lepton number are preserved, the leading order (LO) new physics effects are described by the dimension-six SMEFT Lagrangian,

$$\mathcal{L}^{d=6}_{\text{SMEFT}} = \mathcal{L}_{\text{SM}} + \frac{1}{\Lambda^2}\sum_i C_i\mathcal{O}_i. \tag{3.1}$$

A complete basis of independent dimension-six operators was presented for the first time in [117], the so-called *Warsaw basis*.

This note aims at summarising the ongoing efforts for EFT tools for HH and intends to give recommendations for the use of various EFT parameterisations for HH. The note will map the current efforts and outlines where further efforts are needed.
We distinguish between two different kind of EFTs with different assumptions made on the Higgs field, SM effective field theory (SMEFT) and Higgs effective field theory (HEFT), the latter is also referred to as non-linear chiral electroweak Lagrangian. In SM effective field theory the Higgs boson is assumed to transform as in the SM as a SU(2) doublet. The effective Lagrangian the allows for all operators compatible with the symmetries of the SM. For the Higgs boson sector, the leading operators arise at the dimension-6 level. We define the SM Lagrangian as

$$\begin{aligned}\mathcal{L} = {} & (D_\mu\phi)^\dagger(D^\mu\phi) - \mu^2|\phi|^2 - \lambda|\phi|^4 - \left(y_d\bar{q}_L\phi d_R + y_u\epsilon_{ab}\bar{q}_{La}\phi^\dagger_b u_R + \text{h.c}\right) \\ & - \frac{1}{4}B_{\mu\nu}B^{\mu\nu} - \frac{1}{4}W^a_{\mu\nu}W^{\mu\nu,a} - \frac{1}{4}G^a_{\mu\nu}G^{\mu\nu,a} + \sum_{\psi=q,u,d,\ell}\overline{\psi}\not{D}\psi\end{aligned} \tag{3.2}$$

A summation over the different generations of quarks (q, u and d) and leptons (ℓ) is assumed implicitly. The $\text{SU}(2)_L$ doublet field in the unitary gauge is given by $\phi = 1/\sqrt{2}(0, v+h)^T$ with v denoting the vacuum expectation value, $v \approx 246\,\text{GeV}$. The covariant derivative is defined as conventionally with the plus sign and $G_{\mu\nu}$, $W_{\mu\nu}$ and $B_{\mu\nu}$ are the SU(3), SU(2) and U(1) field strengths. We have assumed CP-conservation. For di-Higgs production allowing also for CP-violating operators see ref. [118]. The effective Lagrangian at dimension-6 can be generally be written in various basis, with the different operators connected by equations of motions. Two different complete basis are the Warsaw basis [117] and the strongly-interacting light Higgs basis (SILH), originally proposed by [119] and completed in [120, 121]. In addition, in [122] the so-called HISZ subset of operators was presented. In the Warsaw basis the effective operators relevant

for di-Higgs production are given by

$$\begin{aligned}\Delta\mathcal{L}_{\text{Warsaw}} = &\frac{C_{\phi,\Box}}{\Lambda^2}(\phi^\dagger\phi)\Box(\phi^\dagger\phi) + \frac{C_{\phi D}}{\Lambda^2}(\phi^\dagger D_\mu\phi)^*(\phi^\dagger D^\mu\phi) + \frac{C_\phi}{\Lambda^2}(\phi^\dagger\phi)^3 \\ &+ \left(\frac{C_{u\phi}}{\Lambda^2}\phi^\dagger\phi\bar{q}_L\phi^c t_R + h.c.\right) + \frac{C_{\phi G}}{\Lambda^2}\phi^\dagger\phi G^a_{\mu\nu}G^{\mu\nu,a} \\ &+ \frac{\overline{C}_{uG}}{\Lambda^2}(\bar{q}_L\sigma^{\mu\nu}T^a G^a_{\mu\nu}\tilde{\phi}t_R + \text{h.c.})\,,\end{aligned} \tag{3.3}$$

where $\tilde{\phi}_i = \epsilon_i k \phi^*_k$. While the Warsaw basis is constructed such that derivative operators are systematically removed by equations of motion, two derivative Higgs interactions remain. They contain covariant derivatives rather than simple derivatives and hence cannot be removed by gauge-independent field redefinitions. In order to obtain a canonically normalised Higgs kinetic term the standard field redefinition is

$$H = \begin{pmatrix} 0 \\ h(1 + c_{H,kin}) + v \end{pmatrix} \tag{3.4}$$

with

$$c_{H,kin} = \left(C_{H,\Box} - \frac{1}{4}C_{HD}\right)\frac{v^2}{\Lambda^2}\,. \tag{3.5}$$

This field redefinition though generates derivative Higgs self-interactions, $h(\partial_\mu h)^2$ and $h^2(\partial_\mu h)^2$. For an easier comparison with other effective descriptions which do not appear in the HEFT Lagrangian. Instead one can use a gauge-dependent field redefinition (which transforms Goldstone/Higgs components in a different way). Such a choice is tricky but we do not need to care for any issues regarding gauge dependence since we do not have gauge fields in the considered process. While the full gauge dependent field redefinition is given for instance in [123], we just need the one of the Higgs

$$h \to h + c_{H,kin}\left(h + \frac{h^2}{v} + \frac{h^3}{3v^2}\right)\,. \tag{3.6}$$

This field redefinition hence leads to a dependence on $c_{H,kin}$ of all Higgs boson couplings.

The SILH Lagrangian instead can be written as

$$\begin{aligned}\Delta\mathcal{L}_{\text{SILH}} = &\frac{\bar{c}_H}{2v^2}\partial_\mu(\phi^\dagger\phi)\partial^\mu(\phi^\dagger\phi) + \frac{\bar{c}_u}{v^2}y_t(\phi^\dagger\phi\,\bar{q}_L\tilde{\phi}t_R + \text{h.c.}) - \frac{\bar{c}_6}{2v^2}\frac{m_h^2}{v^2}(\phi^\dagger\phi)^3 \\ &+ \frac{\bar{c}_{ug}}{v^2}g_s(\bar{q}_L\sigma^{\mu\nu}G_{\mu\nu}\tilde{\phi}t_R + \text{h.c.}) + \frac{4\bar{c}_g}{v^2}g_s^2\phi^\dagger\phi\,G^a_{\mu\nu}G^{a\mu\nu}\,.\end{aligned} \tag{3.7}$$

A canonical definition of the Higgs kinetic term can be obtained by means of the field

redefinition

$$h \to h - \frac{\bar{c}_H}{2}\left(h + \frac{h^2}{v} + \frac{h^3}{3v^2}\right) , \tag{3.8}$$

again leading to a dependence on $\bar{c}_H$ of all Higgs boson couplings. While the operators relevant for di-Higgs production between the SILH and Warsaw basis are basically the same, we have adopted different power counting rules of the coefficients in front of the operators. For eq. (3.3) a purely dimensional power counting was used, while eq. (3.7) reflects the UV predjuice regarding the scaling of the operators, e.g. new physics generating an operator $\phi^\dagger\phi\, G^a_{\mu\nu}G^{a\mu\nu}$ usually stems from colored new particles that couple with the strong coupling constant to the gluons. In ref. [119] for instance the coefficient in front of this operator contains an extra $1/16\pi^2$ to reflect the loop-suppression of weakly coupled new physics to the effective Higgs gluon coupling.

The relevant terms for di-Higgs production of the HEFT Lagrangian is given by

$$\Delta\mathcal{L}_{\text{HEFT}} = -m_t\left(c_t\frac{h}{v} + c_{tt}\frac{h^2}{v^2}\right)\bar{t}\,t - c_{hhh}\frac{m_h^2}{2v}h^3 + \frac{\alpha_s}{8\pi}\left(c_{ggh}\frac{h}{v} + c_{gghh}\frac{h^2}{v^2}\right)G^a_{\mu\nu}G^{a,\mu\nu} . \tag{3.9}$$

In contrast to eqs. (3.3) and (3.7) the couplings of one and two Higgs bosons to fermions or gluons become de-correlated. We noted that we have omitted the top quark dipole operator. From the UV point of view of a weakly interacting model such a coupling would enter at the loop level hence effectively have an extra suppression factor of $1/16\pi^2$. In contrast to the $\phi^\dagger\phi\, G^a_{\mu\nu}G^{a\mu\nu}$ operator that carries such a suppression as well, the dipole-operator enters only via loop diagrams and is hence suppressed compared to all the other operators assuming a weakly-interacting UV model. In table 3.1 we give the

HEFT	SILH	Warsaw
c_{hhh}	$1 - \frac{3}{2}\bar{c}_H + \bar{c}_6$	$1 - 2\frac{v^4}{m_h^2}C_H + 3c_{H,kin}$
c_t	$1 - \frac{\bar{c}_H}{2} - \bar{c}_u$	$1 + c_{H,kin} - C_{uH}\frac{v^3}{\sqrt{2}m_t}$
c_{tt}	$-\frac{\bar{c}_H+3\bar{c}_u}{4}$	$-C_{uH}\frac{3v^3}{2\sqrt{2}m_t} + c_{H,kin}$
c_{ggh}	$128\pi^2\bar{c}_g$	$8\pi/\alpha_s v^2 C_{HG}$
c_{gghh}	$64\pi^2\bar{c}_g$	$4\pi/\alpha_s v^2 C_{HG}$

Table 3.1. Leading order translation between different operator basis choices.

translation among the various choices for an effective field theory description. The HEFT is more general than SMEFT allowing for di-Higgs production to vary the couplings of two Higgs bosons to fermions or gluons in an uncorrelated way from the corresponding couplings with a single Higgs boson. While being more general, this obviously also has

the disadvantage that more barely constrained couplings enter into di-Higgs production leading potentially to degeneracies in their determination. In table 3.1 we also see that the translation between the Warsaw basis as defined from eq. (**??**) contains an α_s. Since α_s is a running parameter and for di-Higgs production typically evaluated at $M_{hh}/2$ a translation between the coupling between Warsaw and SILH/HEFT needs to consider this fact. This can be rectified by including the running of C_{HG} at the order at which the running of α_s is considered or by redefining

$$C_{HG} \to C'_{HG} = \frac{1}{\alpha_s} C_{HG}. \tag{3.10}$$

Finally, we would like to comment on the models which are realised by the different choices for the EFT. Typically, HEFT is the correct choice in strongly-interacting models where the Higgs boson arises as a pseudo-Goldstone boson. Since HEFT does not assume that the Higgs boson transforms within a SM doublet, Goldstone boson scattering is not unitarised by the Higgs boson implying that the HEFT description cannot stay valid for new physics above scales of $\Lambda > 4\pi v$. Generically speaking HEFT assumes larger deviations from the SM. UV models that are generically described by HEFT tend to linearise in the limit in which the coupling deviations are small with respect to the SM. For instance, models like Minimal Composite Higgs Models given the current coupling constraints can in good approximation be described by a linear EFT (SMEFT). Another prime example for HEFT, the dilaton, in its simplest description generically predicts too large coupling deviations in the gluon Higgs couplings [124] and hence also its description via HEFT is challenged. A further example for a UV realisation of HEFT is the singlet model in the strong coupling regime keeping the vacuum expectation value of the singlet close to the electroweak scale [125**?**]. The regime where the HEFT should be the preferred description is though where the mixing between singlet and doublet Higgs fields is rather large hence again strongly constrained by single Higgs coupling measurements. In the limit where both the new mass scale, singlet mass and singlet vacuum expectation value, decouple, is well described within SMEFT. A UV dynamics that is described by HEFT and not SMEFT given the current coupling constraints hence remains an open question. Nevertheless, one should keep in mind that HEFT for di-Higgs production is more general and that Higgs pair production is THE place of probing potential de-correlation among couplings of one or two Higgs bosons to fermions or gauge bosons.

Part II

Single Higgs Processes at the LHC

4 Overview of Higgs production at colliders

The precise determination of the Higgs boson properties is one of the main focus of the Large Hadron Collider (LHC) physics programme. Within the current experimental precision, the measurement of the Higgs couplings so far appear to be in agreement with the Standard Model (SM) prediction within an accuracy of, typically, ten percent [126, 127]. In many beyond the SM (BSM) scenarios, however, it is expected that new physics will introduce modifications in the Higgs properties.

The LO amplitude

We recall the projected LO on shell amplitude [128]

$$\mathcal{M}_{LO} = \frac{T_f \alpha_s g_{ht\bar{t}}}{2\sqrt{2}\pi} \mathcal{F}^{(1\ell)} S_\epsilon, \tag{4.1}$$

with the projector

$$\mathbb{P}^{\mu\nu} = g^{\mu\nu} - 2\frac{p_2^\mu p^\nu}{m_h^2}, \tag{4.2}$$

and the 1 loop form factor

$$\begin{aligned} \mathcal{F}^{(1\ell)} &= m_h \sqrt{\tau}\left((1-\tau)H(0,0,x)+2\right), \\ x &= \frac{\tau + 2\sqrt{1-\tau}-2}{\tau}, \end{aligned} \tag{4.3}$$

where $\tau = 4m_t^2/m_h^2$, $H(m,n,x)$ is the harmonic ploylogarithm function (HPL), and

$$S_\epsilon = \Gamma(1+\epsilon)(\mu/m_t)^{2\epsilon}. \tag{4.4}$$

The decay width is therefore given by

$$\Gamma_{LO}(h \to gg) = \frac{\alpha_s^2 G_F m_h^3 m_t^2 \tau}{8\pi^3\sqrt{2}} \left(3(\tau-1)^2 H(0,0,0,0,x) + 2(\tau-1)H(0,0,x) + 2\right) \tag{4.5}$$

With the following definitions

$$\begin{aligned} g_{ht\bar{t}} &= g_{ht\bar{t}}^{SM} = \frac{\sqrt{2}m_t}{v}, \\ v &= \left(G_F\sqrt{2}\right)^{-1/2}, \\ T_f &= \frac{1}{2}. \end{aligned} \tag{4.6}$$

5 Four top operator in Higgs production and decay

In the previous chapters, the SMEFT has been portrayed as a robust and practical parametrisation of NP degrees of freedom for LHC searches, keeping in mind that these degrees of freedom have masses that are higher than the LHC reach. We have seen in chapter 3 the SMEFT parametrisation for dimension-six operators involving the Higgs boson, and discussed some constraints on them. The operator $\mathcal{O}_\phi$ stands out as one of the weakly constrained SMEFT operators involving the Higgs, this is due to the current low experimental sensitivity on the Higgs self-coupling as shown in **??**. In order to probe the Higgs trilinear sel-coupling directly, one ought to observe Higgs pair production, see **??**. However, it has been proposed that bounds on the Higgs trilinear coupling could still be constructed from single Higgs data, and yield competitive constraints on this coupling than the current Higgs pair searches [109–116], this due the appearance of the Hggs self-coupling in the NLO EW corrections to single Higgs processes, as Figure 5.1 demonstrates an example of such corrections. Using the results from the aforementioned

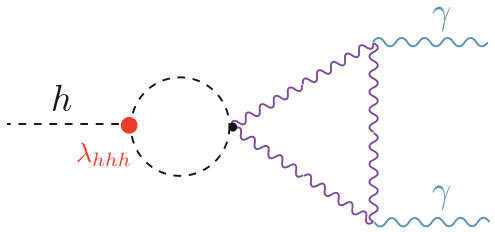

Figure 5.1. NLO EW corrections of single Higgs processes, were the Higgs trilinear self-coupling (the red circle) enters. Here the Higgs decay to two photons is shown as an example.

references, a global fit with all operators that enter at tree-level in addition to the loop effects from the Higgs self-coupling has been preformed in ref. [129]. Additionally, experimental searches for Higgs trilinear self-coupling have been presented by ATLAS [130] and CMS [90].

The physics of the top quark and the Higgs are deeply intertwined, and when one starts looking at the operators entering at NLO of Higgs processes, and by restricting oneself to pure Higgs or EW operators, one would miss the full picture in a global fit. Namely, the top quark operators. Though many of the top quark operators are

strongly constraint from top observables, a few set of dimension-six operators remain as weakly constraint as the trilinear Higgs self-coupling or more. These operators are four-fermion operators involving the top quark. They would be constrained directly from the production of four tops observation. However, this process has a small cross-section at the LHC of 12 fb [131], which is more or less comparable to the Higgs pair production. Experimental searches for the production of four top quarks has been first made byCMS [132] combining different LHC runs, followed by ATLAS [133], the latter reporting a 4.3σ observation of this processes with cross-section of 24^{+7}_{-6} fb. When the whole third generation quarks is included, one sees the same story with $t\bar{t}b\bar{b}$ contact interaction which require the observation of $t\bar{t}b\bar{b}$ production for a direct constraint, see [134, 135] for experimental searches and [136, 137] for SMEFT fits. It should be noted that for the production of four tops, or two tops two beauty quarks in SMEFT, the contact terms do not interfere with the SM process, and only appear proportional to $\mathcal{O}(1/\Lambda^4)$. This makes the SMEFT global analysis of these operators depend highly on the EFT truncation scheme used, i.e. whether to keep quadratic terms or not.

These four-fermion operators enter in single Higgs processes at NLO, in a similar manner as the Higgs self-coupling. In this chapter, the exact NLO corrections to the Higgs rates, i.e. production and decay, due to these four-fermion operators have been competed, and it was found to be significantly larger or at the same scale as the corrections from C_ϕ. Since the four-fermions operators are weakly constrained they should be included in fits involving Higgs data. We shall demonstrate that, there is a significant correlation amongst the Higgs self-coupling and the four-fermion operators.

As the direct bounds for $t\bar{t}t\bar{t}$ and $t\bar{t}b\bar{b}$ contact interactions are weak, single Higgs data provides competitive bounds of there operators alongside other alternative constraints like top quark pair production [138] and electroweak precision data [139] .

The chapter is structured as follows: in section 5.1 the SMEFT four-fermion operators of the third generation are presented. In **??** the full NLO calculation of Higgs rates due to the four-fermion operators is illustrated. Afterwards, in section 5.3, a fit from Higgs data combining the Higgs trilinear coupling and the four-fermion operators is presented, for both Run-II and HL-LHC, with more collaborate results for the latter is found in **??**. The results are further discussed in section 5.4.

5.1 Four-fermion operators in SMEFT

Before estimating the corrections of the four-fermion operators to Higgs rates, we start by introducing these operators in SMEFT . We are interested here in four-fermion operators of the third generation, that arise at dimension-six level. Using the same convention as the Higgs SMEFT operators in chapter 3, we recall the relearnt part of the SMEFT

Lagrangian [117],

$$\begin{aligned}\Delta\mathcal{L}^{d=6}_{\text{SMEFT}} = &\frac{C_{tt}}{\Lambda^2}(\bar{t}_R\gamma_\mu t_R)(\bar{t}_R\gamma^\mu t_R) + \frac{C^{(1)}_{Qt}}{\Lambda^2}(\overline{Q}_L\gamma_\mu Q_L)(\bar{t}_R\gamma^\mu t_R) + \frac{C^{(8)}_{Qt}}{\Lambda^2}(\overline{Q}_L T^A\gamma_\mu Q_L)(\bar{t}_R T^A\gamma^\mu t_R)\\ &+ \frac{C^{(1)}_{QQ}}{\Lambda^2}(\overline{Q}_L\gamma_\mu Q_L)(\overline{Q}_L\gamma^\mu Q_L) + \frac{C^{(3)}_{QQ}}{\Lambda^2}(\overline{Q}_L\sigma_a\gamma_\mu Q_L)(\overline{Q}_L\sigma_a\gamma^\mu Q_L) \qquad (5.1)\\ &+ \left[\frac{C^{(1)}_{QtQb}}{\Lambda^2}(\overline{Q}_L t_R)i\sigma_2(\overline{Q}^{\mathrm{T}}_L b_R) + \frac{C^{(8)}_{QtQb}}{\Lambda^2}(\overline{Q}_L T^A t_R)i\sigma_2(\overline{Q}^{\mathrm{T}}_L T^A b_R) + \text{h.c.}\right]\\ &+ \frac{C_{bb}}{\Lambda^2}(\bar{b}_R\gamma_\mu b_R)(\bar{b}_R\gamma^\mu b_R) + \frac{C^{(1)}_{tb}}{\Lambda^2}(\bar{t}_R\gamma_\mu t_R)(\bar{b}_R\gamma^\mu b_R) + \frac{C^{(8)}_{tb}}{\Lambda^2}(\bar{t}_R T^A\gamma_\mu t_R)(\bar{b}_R T^A\gamma^\mu b_R)\\ &+ \frac{C^{(1)}_{Qb}}{\Lambda^2}(\overline{Q}_L\gamma_\mu Q_L)(\bar{b}_R\gamma^\mu b_R) + \frac{C^{(8)}_{Qb}}{\Lambda^2}(\overline{Q}_L T^A\gamma_\mu Q_L)(\bar{b}_R T^A\gamma^\mu b_R)\,,\end{aligned}$$

here the notation is slightly modified from the standard Warsaw basis one. The flavour indices were suppressed since only the the third generation is considered throughout this chapter. Adopting the same notation from previous chapters, Q_L denotes the left-handed $SU(2)_L$ doublet quarks while t_R and b_R refer to the right-handed singlets, the rest of the objects in (5.1) follow the same conventions as in chapter 3 . In studies involving SMEFT fits, such as [140] the $SU(3)_C$ singlet and octet left-handed operators $C^{(1),SU(3)}_{QQ}$, $C^{(8)}_{QQ}$ are used instead of the singlet and triplet of $SU(2)_L$ appearing in eq. (5.1). These two conventions are related via the relations

$$\begin{aligned}C^{(1),SU(3)}_{QQ} &= 2C^{(1)}_{QQ} - \frac{2}{3}C^{(3)}_{QQ},\\ C^{(8)}_{QQ} &= 8C^{(3)}_{QQ}.\end{aligned} \qquad (5.2)$$

Additionally, all of these Wilson coefficients are assumed to be real.

From here on, only operators that induce sizeable NLO correction to Higgs processes are taken into account. These operators turns out to be the ones that introduce loop corrections to the top or beauty Yukawa, top or beauty masses and finite corrections from top loops. Such corrections will be proportional to the top mass. On the contrary, corrections from beauty loops are highly suppressed by m_b. Also, operators that have chiral structure that does not enable them to enter in the Yukawa renormalisation group equation (RGE)'s will not be constrained from Higgs data as they would only contribute through small finite terms, as we shall see later. Hence, only four top and the $\mathcal{O}^{(1),(8)}_{QtQb}$ operators will be considered, as they will possess corrections with top quark loops.

5.2 Contribution of four-fermion operators to Higgs rates at NLO

This section will demonstrate the calculation of NLO Higgs production and decay rates from the four-heavy-quarks operators discussed above. For the production of Higgs via gluon fusion or Higgs decay to gluon, photons and beauty quarks, the results were computed fully analytically and presented in this section. However, for the associated production of the Higgs with top pair $t\bar{t}h$, the corrections were computed numerically, due to the length of the the analytic expressions if the result.

5.2.1 Analytic calculations

The NLO corrections to gluon fusion, $h \to gg$, $h \to \gamma\gamma$ and $h \to b\bar{b}$ all come from the sub-diagrams listed in Table 5.1, with top loops entering in the mass renormalisation or to/beauty Yukawa vertex correction. Where $N_c = 3$ the number of colours, and $c_F = (N_c^2 - 1)/(2N_c) = 4/3$ the $SU(3)$ quadratic Casimir in the fundamental representation. The effect of beauty loops coming from for $C_{QtQb}^{(1/8)}$, can be easily read from this table by

Diagram	colour factor		mass/coupling
	singlet	octet	
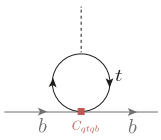	$2N_c + 1$	c_F	$y_t\, m_b\, m_t^2$
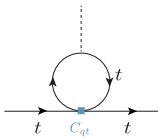	1	c_F	$y_t\, m_t^3$
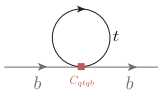	$2N_c + 1$	c_F	m_t^3
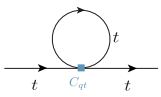	1	c_F	m_t^3

Table 5.1. The sub diagrams contributing to the NLO corrections of gluon fusion Higgs production higgsdecasy to gluon, photon and beauty quarks.

exchanging $t \leftrightarrow b$, which is significantly smaller than the corrections coming from top loops.

We see that these corrections correspond to the Wilson coefficients appearing in the RGE's include them in the appendix, and operators with (LL)(LL) or (RR(RR)) chiral structures do not contribute to these processes.
By considering the two-loop corrections to the gluon fusion illustrated in Figure 5.2 we find that such correction contain the sub-diagrams shown in Table 5.1, except for diagram (e), which is found to be vanishing for on-shell gluons. Additionally, these diagrams indicated that the two-loop corrections will be reduced to a product of two one-loop functions after the integral reduction.
Following the Feynman rules derived in ref. [141] for the four-fermion operators of interest here, the *ggtoh* two-loop amplitude was calculated, then Dirac algebra and further algebraic manipulations were preformed in Mathematica using `PackageX` [142]. Reduction of the resulting two-loop to Master integrals has been preformed using `KIRA` [143], all of the resulting master integrals were indeed products on one-loop functions as expected. The computation has been cross-checked independently, using a different pipeline : `FeynArts` [144], for amplitude generation then `FeynRules` [145] and `Fire` [146] for algebriac manipulation and loop-integral reduction.

The sub-diagrams appearing in the two-loop calculation, correspond to mass and vertex renormalisation, hence they contain poles that require counter-terms. A mixture of on-shell (OS) and $\overline{\text{MS}}$ – schemes has been used for the mass and $hq\bar{q}$ coupling renormalisation, respectively. The renormalisation of SM quantities in the OS and NP ones in the $\overline{\text{MS}}$ scheme was proposed by [147], which provides consistency since the NP is assumed to be of a Higher scale than the SM.

The top/beauty mass renormalisation can be expressed as

$$m_{t/b}^{\text{OS}} = m_{t/b}^{(0)} - \delta m_{t/b}, \tag{5.3}$$

with the corresponding counter-terms

$$\begin{aligned}\delta m_t =& \frac{1}{16\pi^2}\frac{C_{Qt}^{(1)} + c_F C_{Qt}^{(8)}}{\Lambda^2} m_t^3 \left[\frac{2}{\bar{\epsilon}} + 2\log\left(\frac{\mu_R^2}{m_t^2}\right) + 1\right] \\ &+ \frac{1}{16\pi^2}\frac{(2N_c+1)C_{QtQb}^{(1)} + c_F C_{QtQb}^{(8)}}{\Lambda^2}\left[\frac{1}{\bar{\epsilon}} + \log\left(\frac{\mu_R^2}{m_b^2}\right) + 1\right] m_b^3\,,\end{aligned} \tag{5.4}$$

$$\delta m_b = \frac{1}{16\pi^2}\frac{(2N_c+1)C_{QtQb}^{(1)} + c_F C_{QtQb}^{(8)}}{\Lambda^2}\left[\frac{1}{\bar{\epsilon}} + \log\left(\frac{\mu_R^2}{m_t^2}\right) + 1\right] m_t^3\,, \tag{5.5}$$

with $\bar{\epsilon}^{-1} = \epsilon^{-1} - \gamma_E + \log(4\pi)$, in dimensional regularization with $d = 4 - 2\epsilon$. It is

possible to convert from OS to the $\overline{\text{MS}}$ scheme for mass counter-terms via the following relations

$$\delta m_t^{\overline{\text{MS}}} = \frac{1}{8\pi^2}\frac{C_{Qt}^{(1)} + c_F C_{Qt}^{(8)}}{\Lambda^2} m_t^3 \frac{1}{\bar{\epsilon}} + \frac{1}{16\pi^2}\frac{(2N_c+1)C_{QtQb}^{(1)} + c_F C_{QtQb}^{(8)}}{\Lambda^2}\frac{1}{\bar{\epsilon}} m_b^3 \,, \tag{5.6}$$

$$\delta m_b^{\overline{\text{MS}}} = \frac{1}{16\pi^2}\frac{(2N_c+1)C_{QtQb}^{(1)} + c_F C_{QtQb}^{(8)}}{\Lambda^2}\frac{1}{\bar{\epsilon}} m_t^3 \,. \tag{5.7}$$

The effect of changing to the mass renormalisation scheme is small for the top mass but rather significant, up to 100% for the beauty mass.
The top/beauty Higgs coupling in SMEFT, is written as

$$g_{ht\bar{t}/hb\bar{b}} = \frac{m_{t/b}}{v} - \frac{v^2}{\Lambda^2}\frac{C_{t\phi/b\phi}}{\sqrt{2}} \,. \tag{5.8}$$

Hence, a modification of the Higgs couplings to bottom and top quarks is generated by operator mixing, even if $C_{t\phi/b\phi}$ are zero at Λ. From this, the $\overline{\text{MS}}$ counter-term should take the form

$$\delta g_{ht\bar{t}/hb\bar{b}} = \frac{m_{t/b}}{v}\delta m_{t/b} - \frac{v^2 \delta C_{t\phi/b\phi}}{\sqrt{2}}, \tag{5.9}$$

where $\delta C_{t\phi/b\phi}$ is directly read from the anomalous dimension, see App for the explicit expression of the RGE's.

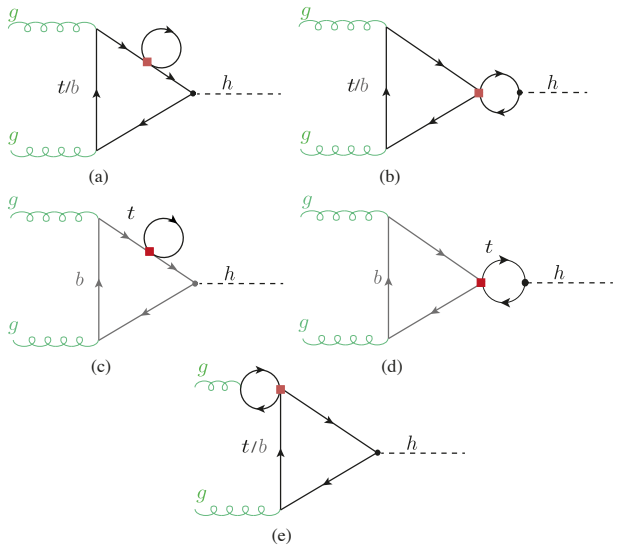

Figure 5.2. Example Feynman diagrams for four-fermion-operator contributions to the Higgs production via gluon fusion. The red box indicates the four-fermion operator.

Correction to gluon fusion and $h \to gg$

The modification of the Higgs production via gluon fusion can be written as

$$\frac{\sigma_{ggF}}{\sigma_{ggF}^{\mathrm{SM}}} = 1 + \frac{\sum_{i=t,b} 2\mathrm{Re}\left(F_{\mathrm{LO}}^{i} F_{\mathrm{NLO}}^{*}\right)}{\left|F_{\mathrm{LO}}^{t} + F_{\mathrm{LO}}^{b}\right|^{2}} \tag{5.10}$$

with

$$F_{\mathrm{LO}}^{i} = -\frac{8m_i^2}{m_h^2}\left[1 - \frac{1}{4}\log^2(x_i)\left(1 - \frac{4m_i^2}{m_h^2}\right)\right] \tag{5.11}$$

and

$$\begin{aligned} F_{\mathrm{NLO}} =& \frac{1}{4\pi^2\Lambda^2}(C_{Qt}^{(1)} + c_F C_{Qt}^{(8)}) F_{\mathrm{LO}}^{t}\left[2m_t^2 + \frac{1}{4}(m_h^2 - 4m_t^2)\left(3 + 2\sqrt{1 - \frac{4m_t^2}{m_h^2}}\log(x_t)\right)\right. \\ &\left. + \frac{1}{2}(m_h^2 - 4m_t^2)\log\left(\frac{\mu_R^2}{m_t^2}\right)\right] \\ &+ \frac{1}{32\pi^2\Lambda^2}((2N_c+1)C_{QtQb}^{(1)} + c_F C_{QtQb}^{(8)})\left[F_{\mathrm{LO}}^{b}\frac{m_t}{m_b}\left(4m_t^2 - 2m_h^2\right.\right. \\ &\left.\left. -(m_h^2 - 4m_t^2)\sqrt{1 - \frac{4m_t^2}{m_h^2}}\log(x_t) - (m_h^2 - 4m_t^2)\log\left(\frac{\mu_R^2}{m_t^2}\right)\right) + (t \leftrightarrow b)\right]. \end{aligned} \tag{5.12}$$

Only top quark loops contribute to the parts proportional to $C_{Qt}^{(1),(8)}$. The variable x_i for a loop particle with mass m_i is given by

$$x_i = \frac{-1 + \sqrt{1 - \frac{4m_i^2}{m_h^2}}}{1 + \sqrt{1 - \frac{4m_i^2}{m_h^2}}}. \tag{5.13}$$

Using the same amplitudes, the $h \to gg$ partial width modification can be written as

$$\frac{\Gamma_{h\to gg}}{\Gamma_{h\to gg}^{\mathrm{SM}}} = 1 + \frac{\sum_{i=t,b} 2\mathrm{Re}\left(F_{\mathrm{LO}}^{i} F_{\mathrm{NLO}}^{*}\right)}{|F_{\mathrm{LO}}^{t} + F_{\mathrm{LO}}^{b}|^{2}} \tag{5.14}$$

Correction to Higgs decays to photons

Analogously, since the decay $h \to \gamma\gamma$ contains the same topologies as gluon fusion, we could use the result from the above calculation to calculate the correction to

the partial width for this decay

$$\frac{\Gamma_{h\to\gamma\gamma}}{\Gamma^{\rm SM}_{h\to\gamma\gamma}} = 1 + \frac{2{\rm Re}\left(F_{{\rm LO},\gamma}F^*_{{\rm NLO},\gamma}\right)}{|F_{{\rm LO},\gamma}|^2}. \tag{5.15}$$

However, one should pay attention to the change in the prefactors, and the extra EW contributions for $h \to \gamma\gamma$

$$F_{{\rm LO},\gamma} = N_C\, Q_t^2 F^t_{\rm LO} + N_C\, Q_b^2 F^b_{\rm LO} + F^W_{\rm LO} + F^G_{LO}, \tag{5.16}$$

and $F_{{\rm NLO},\gamma}$ is obtained from $F_{\rm NLO}$ by replacing the LO form factor that appears inside of it by $F^i_{\rm LO} \to N_c\, Q_i^2 F^i_{\rm LO}$, with the charges $Q_t = 2/3$ and $Q_b = -1/3$. The W boson contribution

$$F^W_{\rm LO} = 2\left(1 + 6\frac{m_W^2}{m_h^2}\right) - 6\frac{m_W^2}{m_h^2}\left(1 - 2\frac{m_W^2}{m_h^2}\right)\log^2(x_W), \tag{5.17}$$

with m_W the W mass, and the Goldstone contribution

$$F^G_{\rm LO} = 4\frac{m_W^2}{m_h^2}\left(1 + \frac{m_W^2}{m_h^2}\,\log^2(x_W)\right). \tag{5.18}$$

Four-fermion operators also affect the $h \to Z\gamma$ partial width. However, as in the diphoton case, the effect is expected to be small due to the dominance of the W boson loop. Because of this, and given the smallness of the $h \to Z\gamma$ branching ratio and the relatively low precision expected in this channel at the LHC, the effects of four-fermion interactions in this decay are neglected.

Correction to Higgs decays to $b\bar{b}$

The dominant four-fermion contributions to decay channel $h \to b\bar{b}$ come from the operators with Wilson coefficients $C^{(1),(8)}_{QtQb}$. The corresponding diagram at NLO is shown in fig 5.3. Adopting the same renormalisation procedure as outlined in the previous subsection, we obtain the following expression for the correction to the $h \to b\bar{b}$ decay rate in the presence of $\mathcal{O}^{(1),(8)}_{QtQb}$,

$$\begin{aligned}\frac{\Gamma_{h\to b\bar{b}}}{\Gamma^{\rm SM}_{h\to b\bar{b}}} =& 1 + \frac{1}{16\pi^2}\frac{m_t}{m_b}(m_h^2 - 4m_t^2)\frac{(2N_c+1)C^{(1)}_{QtQb} + c_F C^{(8)}_{QtQb}}{\Lambda^2} \\ &\times\left[2 + \sqrt{1 - \frac{4m_t^2}{m_h^2}}\log(x_t) - \log\left(\frac{m_t^2}{\mu_R^2}\right)\right],\end{aligned} \tag{5.19}$$

which carries an enhancement factor of m_t/m_b and is hence expected to be rather

large.

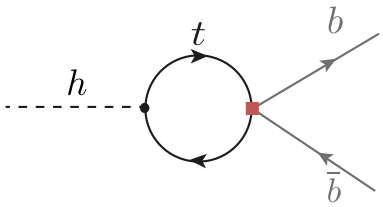

Figure 5.3. Feynman diagram contributing to the NLO $h \to b\bar{b}$ process.

The results of the NLO effects from the four-fermion operators reported above, do not take into an account the running of the Wilson coefficients. This would be based on the assumption that these coefficients are defined at the process scale. Nevertheless, when we want to compare different process or assume that the four-fermion operators are defined at the UV scale, i.e. Λ, for example after matching with some UV model. One has take into an account the running of these Wilson coefficients from Λ down to the process scale Those running effects can be included via the renormalisation group equation (RGE) for the operators with Wilson coefficient $C_{t\phi}$ and $C_{b\phi}$ [148, 149], that lead approximatively to

$$\begin{aligned} C_{t\phi}(\mu_R) - C_{t\phi}(\Lambda) = & \frac{1}{16\pi^2 v^2}\left[-2y_t(m_h^2 - 4m_t^2)(C_{Qt}^{(1)} + c_F C_{Qt}^{(8)})\log\left(\frac{\mu_R^2}{\Lambda^2}\right)\right. \\ & \left. + \frac{y_b}{2}(m_h^2 - 4m_b^2)\left((2N_c+1)C_{QtQb}^{(1)} + c_F C_{QtQb}^{(8)}\right)\log\left(\frac{\mu_R^2}{\Lambda^2}\right)\right] \end{aligned} \tag{5.20}$$

and

$$C_{b\phi}(\mu_R) - C_{b\phi}(\Lambda) = \frac{y_t}{32\pi^2 v^2}\left[(m_h^2 - 4m_t^2)\left((2N_c+1)C_{QtQb}^{(1)} + c_F C_{QtQb}^{(8)}\right)\log\left(\frac{\mu_R^2}{\Lambda^2}\right)\right], \tag{5.21}$$

where $y_{t/b} = \sqrt{2}m_{t/b}/v$. Note that the combinations of Wilson coefficients appearing in (5.20)(5.21) are the same as in F_{NLO} in (5.12). Effectively, we can then obtain the result under the assumption that the four-fermion operators are the only non-zero ones at the high scale by replacing in (5.12) $\mu_R \to \Lambda$, noting that we have renormalised the top and beauty quark masses in the OS scheme. Including the leading logarithmic running of $C_{b\phi}$ of (5.21) from the high scale Λ to the electroweak scale is achieved by setting in (5.19) $\mu_R \to \Lambda$. The expression in (5.19) agrees with results obtained from the full calculation of the NLO effects in the dimension-six SMEFT, first computed in [150].

5.2.2 NLO corrections to $t\bar{t}h$

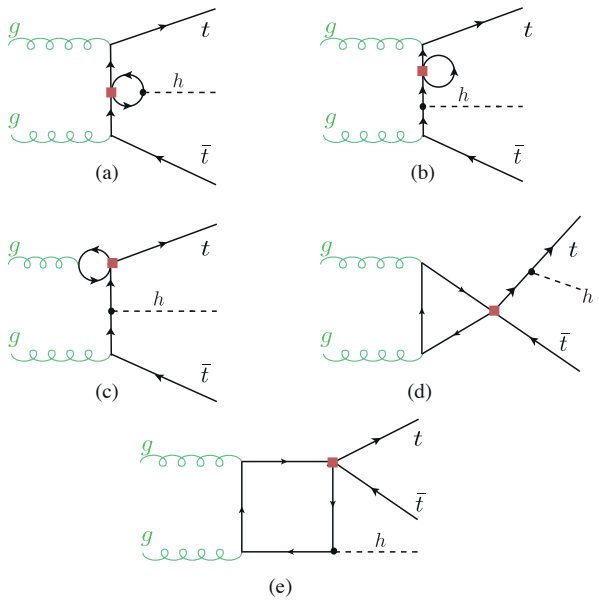

Figure 5.4. Feynman diagrams including the four-fermion loop contributions to the $gg \to t\bar{t}h$ subprocess.

Unlike the previous processes, the associated production of the Higgs with top quark pair involves new topologies not limited to Yukawa vertex or mass renormalisation. At the LHC, there are two sub-processes responsible for the $t\bar{t}h$ production: gluon-initiated process illustrated in Figure 5.4 and quark-initiated one, see in Figure 5.5. We see the new *finite* topologies induced by the four-fermion operator corrections in (d) triangle and (e) box topologies in Figure 5.4 and (b) triangle topology in Figure 5.5. Additionally, the $t\bar{t}g$ vertex correction in the quark-initiated process (diagram (c)) of Figure 5.5 is non-vanishing as the gluon is off-shell. This vertex correction has a UV pole that requires a counter-term for its cancellation

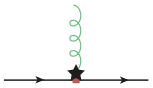

$$= \frac{ig_s}{12\pi^2\Lambda^2} T^A_{ij} p_g^2 \gamma^\mu \left(C_{tt} P_R + \left(C^{(1)}_{QQ} + C^{(3)}_{QQ} \right) P_L + \frac{C^{(8)}_{Qt}}{4} \right) \left(\frac{1}{\bar{\epsilon}} - 1 \right). \quad (5.22)$$

Another difference between $t\bar{t}h$ and the rest of the processes considered, is that this process has multiple colour projectors, as the quark anti quark triplets or the gluon pairs do not have to recombine to only a singlet state rather to both a singlet and an octet, according to the expansion of product $\mathbf{3} \otimes \overline{\mathbf{3}} \to \mathbf{1} + \mathbf{8}$. This breaks the degeneracy between the singlet and octet Wilson coefficients. Lastly, due to the new topologies and

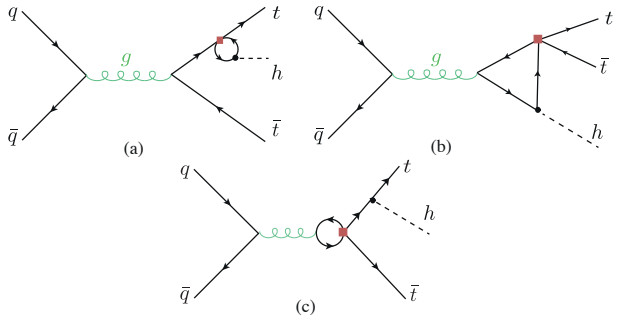

Figure 5.5. Feynman diagrams including the four-fermion loop contributions to the $q\bar{q} \to t\bar{t}h$ subprocess.

$t\bar{t}g$ vertex correction, operators with single chirality will contribute to NLO corrections, namely Ctt and $C_{QQ}^{(1,3)}$.

All of the four-fermion operators are implemented in the loop-capable UFO model `SMEFTatNLO` model [138] and their contribution to NLO corrections of $t\bar{t}h$ can hence be computed via `Madgraph_aMCNLO` [151] (version 3.1.0) with some tweaking to remove the NLO QCD corrections. This is done via a use-defined loop filter function in Madgraph. The results were reproduced by an analytic computation based on the reduction of one-loop amplitudes via the method developed by G. Ossola, C.G. Papadopoulos and R. Pittau (OPP reduction) [152]. The OPP reduction was done using the `CutTools` programme [153]. This programme take the full one-loop amplitude and then reduces it to terms with 1,2,3 and 4-point loop functions in four dimensions, keeping spurious terms from the ϵ part of the amplitude. To correct for such terms, one needs to compute the divergent UV counter-term as well as a finite rational terms, denoted R_2 as in Ref. [154].[1] The amplitudes were generated in the same way as for gluon fusion. The UV and R_2 counter-terms, that need to be supplemented to `CutTools`, were computed manually following the method detailed in [154]. For both codes, the NNPDF23 parton distribution functions set at NLO [155] was used.

The singlet and octet operators $\mathcal{O}_{QtQb}^{(1),(8)}$ contribute to $t\bar{t}h$ only via beauty loops and in principle, could be directly dismissed like the other beauty quark operators mentioned above. However, it is instructive to investigate their effect albeit it is expected to be small. Since the `SMEFTatNLO` model does not have these operators, it was needed to implement them manually in that model. This is simply done by include the vertices generated by these operators as well as their UV and R_2 counter-terms, only relevant for $t\bar{t}th$ calculation. The calculation of the NLO correction by these operators was done both in Madgraph using a modified UFO model and with the code based on `CutTools`.

[1] Another rational term R_1 appears due to the mismatch between the four and d dimensional amplitudes, but this is computed automatically in `CutTools`.

The effects where comparable to the leading log effects computed using `SMEFTsim` package [156] of $\sim 10^{-6}$. Hence confirming the expectation that beauty quark loops have a negligible effect.

In order to take the effect of Wilson coefficients' running, the relevant contribution for the gluon-initiated process as the same as the stated for the gluon fusion in (5.20). While for the quark-initiated process, one needs to consider the operator mixing in the running, particularly between operators that contain second and third generation quarks mixed together. These corrections can be obtained from the RGEs in refs. [148, 149, 157].

5.2.3 Results

The NLO correction from the four-fermion operators of the third generation quarks on the Higgs rates i.e., partial width Γ or cross-section σ., is extracted from the above computation using the formula

$$\delta R(C_i) = R/R^{\mathrm{SM}} - 1, \tag{5.23}$$

here effect from the operator with Wilson coefficient C_i on the Higgs rate R is denoted by $\delta R(C_i)$. Only contributions linear in the Wilson coefficients are considered. In order to isolate the finite terms from the ones coming from the RGE leading log approximation, the correction is further expanded to finite $\delta R^{fin}_{C_i}$ and leading log terms $\delta R^{log}_{C_i}$ as follows

$$\delta R(C_i) = \frac{C_i}{\Lambda^2}\left(\delta R^{fin}_{C_i} + \delta R^{log}_{C_i}\log\left(\frac{\mu_R^2}{\Lambda^2}\right)\right). \tag{5.24}$$

Using this formula, one can obtain the correction at any NP scale Λ, though in the remainder of this chapter this scale is set to 1 TeV. In Table 5.2, the finite and logarithmic corrections for the operators considered in this study is reported. Using this table in filling the formula (5.24) will give the correction to Higgs rates. However, since some of the rates are Higgs partial widths, the Higgs total width Γ_h will be affected and therefore all of Higgs rates are changed. An important observation from Table 5.2 is that the finite terms, are either larger or at the same order than the leading log ones, except for $h \to b\bar{b}$ corrections from $C^{(1),(8)}_{QtQb}$. This highlights the importance of thee full NLO calculation for these corrections in constraining these four-fermion operators, in particular $\mathcal{O}^{(1),(8)}_{Qt}$.

As mentioned earlier, there is a degeneracy amongst the singlet and octet operators, seen clearly in the analytic result for gluon fusion and Higgs decays considered. This degeneracy is though broken for $\mathcal{O}^{(1),(8)}_{Qt}$ due to $t\bar{t}h$. Since, the effect of $\mathcal{O}^{(1),(8)}_{QtQb}$ is negligible for this process, thee true degree of freedom for these operators' Wilson coefficients is the linear combination

$$C^{+}_{QtQb} = (2N_c + 1)C^{(1)}_{QtQb} + c_F C^{(8)}_{QtQb}. \tag{5.25}$$

Operator	Process	μ_R	$\delta R_{C_i}^{fin}$ [TeV^2]	$\delta R_{C_i}^{log}$ [TeV^2]
$\mathcal{O}_{Qt}^{(1)}$	ggF	$\frac{m_h}{2}$	$9.91 \cdot 10^{-3}$	$2.76 \cdot 10^{-3}$
	$h \to gg$	m_h	$6.08 \cdot 10^{-3}$	$2.76 \cdot 10^{-3}$
	$h \to \gamma\gamma$		$-1.76 \cdot 10^{-3}$	$-0.80 \cdot 10^{-3}$
	$t\bar{t}h$ 13 TeV	$m_t + \frac{m_h}{2}$	$-4.20 \cdot 10^{-1}$	$-2.78 \cdot 10^{-3}$
	$t\bar{t}h$ 14 TeV		$-4.30 \cdot 10^{-1}$	$-2.78 \cdot 10^{-3}$
	Γ_h	$\frac{m_h}{2}$	$4.93 \cdot 10^{-4}$	$1.68 \cdot 10^{-4}$
$\mathcal{O}_{Qt}^{(8)}$	ggF	$\frac{m_h}{2}$	$1.32 \cdot 10^{-2}$	$3.68 \cdot 10^{-3}$
	$h \to gg$	m_h	$8.11 \cdot 10^{-3}$	$3.68 \cdot 10^{-3}$
	$h \to \gamma\gamma$		$-2.09 \cdot 10^{-3}$	$-1.07 \cdot 10^{-3}$
	$t\bar{t}h$ 13 TeV	$m_t + \frac{m_h}{2}$	$6.53 \cdot 10^{-2}$	$-2.40 \cdot 10^{-3}$
	$t\bar{t}h$ 14 TeV		$7.29 \cdot 10^{-2}$	$2.40 \cdot 10^{-3}$
	Γ_h	$\frac{m_h}{2}$	$6.58 \cdot 10^{-4}$	$2.24 \cdot 10^{-4}$
$\mathcal{O}_{QtQb}^{(1)}$	ggF	$\frac{m_h}{2}$	$2.84 \cdot 10^{-2}$	$9.21 \cdot 10^{-3}$
	$h \to gg$		$1.57 \cdot 10^{-2}$	$9.21 \cdot 10^{-3}$
	$h \to \gamma\gamma$	m_h	$-1.30 \cdot 10^{-3}$	$-0.78 \cdot 10^{-3}$
	$h \to b\bar{b}$		$9.25 \cdot 10^{-2}$	$1.68 \cdot 10^{-1}$
	Γ_h	$\frac{m_h}{2}$	$5.49 \cdot 10^{-2}$	$7.37 \cdot 10^{-2}$
$\mathcal{O}_{QtQb}^{(8)}$	ggF	$\frac{m_h}{2}$	$5.41 \cdot 10^{-3}$	$1.76 \cdot 10^{-3}$
	$h \to gg$		$2.98 \cdot 10^{-3}$	$1.76 \cdot 10^{-3}$
	$h \to \gamma\gamma$	m_h	$-0.25 \cdot 10^{-3}$	$-0.15 \cdot 10^{-3}$
	$h \to b\bar{b}$		$1.76 \cdot 10^{-2}$	$3.20 \cdot 10^{-2}$
	Γ_h	$\frac{m_h}{2}$	$1.05 \cdot 10^{-2}$	$1.41 \cdot 10^{-2}$
$\mathcal{O}_{QQ}^{(1)}$	$t\bar{t}h$ 13 TeV	$m_t + \frac{m_h}{2}$	$1.75 \cdot 10^{-3}$	$1.90 \cdot 10^{-3}$
	$t\bar{t}h$ 14 TeV		$2.35 \cdot 10^{-3}$	$1.90 \cdot 10^{-3}$
$\mathcal{O}_{QQ}^{(3)}$	$t\bar{t}h$ 13 TeV	$m_t + \frac{m_h}{2}$	$1.32 \cdot 10^{-2}$	$5.50 \cdot 10^{-3}$
	$t\bar{t}h$ 14 TeV		$1.42 \cdot 10^{-2}$	$5.50 \cdot 10^{-3}$
$\mathcal{O}_{tt}$	$t\bar{t}h$ 13 TeV	$m_t + \frac{m_h}{2}$	$4.60 \cdot 10^{-3}$	$2.01 \cdot 10^{-3}$
	$t\bar{t}h$ 14 TeV		$5.09 \cdot 10^{-3}$	$2.01 \cdot 10^{-3}$

Table 5.2. The NLO corrections from the four heavy-quark SMEFT operators of this study to single Higgs rates. We have separated the contributions into the finite piece $\delta R_{C_i}^{fin}$ and the leading log running of the Wilson coefficients $\delta R_{C_i}^{log}$, see (5.24).

5.3 Fit to Higgs observables

Using the results from the prevous NLO calculations, and combining them with the calculations of NLO Higgs rates from the trilinear Higgs self-coupling λ_3,preformed in ref. [110–113, 115] we could expand on the previous fits for λ_3 from Higgs data, to include four-fermion SMEFT Wilson coefficients as well. In order to examine the true sensitivity

of single Higgs observables to λ_3. Although combined fits from Higgs data including λ_3 and SMEFT operators modifying Higgs rates at LO has been preformed [129]. Such fits would not be sufficient in determine the actual sensitivity for λ_3, in particular when the SMEFT operators are weakly constraint and possess significant modifications to Higgs rates as we have seen in Table 5.2. This chapter does not include a global SMEFT fit, but merely motivates it by illustrating how thee sensitivity for probing the Higgs-self coupling from single Higgs data gets diluted when the four-fermion operators are included, and how these two are correlated.

In the previous references, the modification to Higgs self coupling was reported in terms of the κ-formalism, for the consistency of this analysis, the NLO corrections from the trilinear self-coupling will be converted from this formalism to the SMEFT notation, in terms of the Wilson coefficient C_ϕ. For more details on the conversion between SMEFT and κ-formalism see app here or something. In order to keep track of power counting (in terms of Λ) in SMEFT, we expand the results of [111] after converting it to SMEFT , to get

$$\delta R_{\lambda_3} \equiv \frac{R_{\rm NLO}(\lambda_3) - R_{\rm NLO}(\lambda_3^{\rm SM})}{R_{\rm LO}} = -2\frac{C_\phi v^4}{\Lambda^2 m_h^2} C_1 + \left(-4\frac{C_\phi v^4}{\Lambda^2 m_h^2} + 4\frac{C_\phi^2 v^8}{m_h^4 \Lambda^4}\right) C_2. \tag{5.26}$$

In (5.26), the coefficient C_1 corresponds to the contribution of the trilinear coupling to the single Higgs processes at one loop, adopting the same notation as [111]. The values of C_1 for the different processes of interest for this paper are given in **??**. The coefficient C_2 describes universal corrections and is given by

$$C_2 = \frac{\delta Z_h}{1 - \left(1 - \frac{2C_\phi v^4}{\Lambda^2 m_h^2}\right)^2 \delta Z_h}, \tag{5.27}$$

where the constant δZ_h is the SM contribution from the Higgs loops to the wave function renormalisation of the Higgs boson,

$$\delta Z_h = -\frac{9}{16}\frac{G_F m_h^2}{\sqrt{2}\pi^2}\left(\frac{2\pi}{3\sqrt{3}} - 1\right). \tag{5.28}$$

The coefficient C_2 thus introduces additional $\mathcal{O}(1/\Lambda^4)$ (and higher order) terms in δR_{λ_3}. In ref. [111] considering the κ formalism the full expression of (5.27) is kept, while we define two different descriptions: one in which we expand δR_{λ_3} up to linear order and an alternative scheme in which we keep also terms up to $\mathcal{O}(1/\Lambda^4)$ in the EFT expansion. Keeping the full expression in (5.27) and including terms up to $\mathcal{O}(1/\Lambda^4)$ in C_2 lead to nearly the same results as the simple $\mathcal{O}(1/\Lambda^4)$ fit.

A Bayesian fit was preformed using Markov-chain Monte Carlo (MCMC) method.

Process	C_1	$\delta R^{fin}_{C_\phi}$
ggF/ $gg \to h$	$6.60 \cdot 10^{-3}$	$-3.10 \cdot 10^{-3}$
$t\bar{t}h$ 13 TeV	$3.51 \cdot 10^{-2}$	$-1.64 \cdot 10^{-2}$
$t\bar{t}h$ 14 TeV	$3.47 \cdot 10^{-2}$	$-1.62 \cdot 10^{-2}$
$h \to \gamma\gamma$	$4.90 \cdot 10^{-3}$	$-2.30 \cdot 10^{-3}$
$h \to b\bar{b}$	0.00	0.00
$h \to W^+W^-$	$7.30 \cdot 10^{-3}$	$-3.40 \cdot 10^{-3}$
$h \to ZZ$	$8.30 \cdot 10^{-3}$	$-3.90 \cdot 10^{-3}$
$pp \to Zh$ 13 TeV	$1.19 \cdot 10^{-2}$	$-5.60 \cdot 10^{-3}$
$pp \to Zh$ 14 TeV	$1.18 \cdot 10^{-2}$	$-5.50 \cdot 10^{-3}$
$pp \to W^\pm h$	$1.03 \cdot 10^{-2}$	$-4.80 \cdot 10^{-3}$
VBF	$6.50 \cdot 10^{-3}$	$-3.00 \cdot 10^{-3}$
$h \to 4\ell$	$8.20 \cdot 10^{-3}$	$-3.80 \cdot 10^{-3}$

Table 5.3. The relative correction dependence on C_ϕ for single Higgs processes taken from [115]. If the $\sqrt{s}$ is not indicated, the C_1 coefficient (see eq. (5.26)) is the same for both 13 and 14 TeV.

Using a flat prior s $\pi(C_i) = const.$ and a log likelihood of a Gaussian distribution

$$\log(L) = -\frac{1}{2}\left[(\vec{\mu}_{\text{Exp}} - \vec{\mu})^T \cdot \mathbf{V}^{-1} \cdot (\vec{\mu}_{\text{Exp}} - \vec{\mu})\right]. \tag{5.29}$$

Constructed as follows:

Experimental input $\vec{\mu}_{\text{Exp}}$ The signal strength from experimental measurements of single Higgs rates defined as

$$\mu_{\text{Exp}} \equiv \sigma_{\text{Obs}}/\sigma_{\text{SM}}. \tag{5.30}$$

These measurements as taken from LHC Run II for centre-of-mass energy of $\sqrt{s} =$ 13 TeV and integrated luminosity of $139\,\text{fb}^{-1}$ for ATLAS and $137\,\text{fb}^{-1}$ for CMS. In addition to HL-LHC projections by CMS for $\sqrt{s} = 14$ TeV and integrated luminosity of $3000\,\text{fb}^{-1}$. Both of these input types have been already discussed in link here and summarised in Table 2.1.

Theoretical prediction $\vec{\mu}$ The corresponding theoretical predictions for each of the experimental measurement /projection have been built using the modification to the cross-sections and branching ratios coming from the SMEFT four-fermion operators and C_ϕ. To keep with the power-counting, the signal strength is also expanded

in powers of Λ, keeping only Λ^{-2} terms.

$$\mu(C_\phi, C_i) = \frac{\sigma_{\text{Prod}}(C_\phi, C_i) \times \text{BR}(C_\phi, C_i)}{\sigma_{\text{Prod,SM}} \times \text{BR}_{\text{SM}}} \approx 1 + \delta\sigma(C_\phi, C_i) + \delta\Gamma(C_\phi, C_i) - \delta\Gamma_h(C_\phi, C_i). \tag{5.31}$$

Uncertainties and correlations V The correlation matrix $\mathbf{V}$ is build from thee experimental uncertainties found in Table 2.1. For Run-II data, only ATLAS collaboration reported the correlation amongst different channels, and only correlations $> 10\%$ are considered. While for the HL-LHC, the whole correlation matrix found on the webpage [158]. The HL-LHC projections for the S2 scenario explained in [159] were used. These assume the improvement on the systematics that is expected to be attained by the end of the HL-LHC physics programme, and that theory uncertainties are improved by a factor of two with respect to current values. Theoretical uncertainties were not considered in this fit

The python package `pymc3` [160] was used to construct the posterior distribution. We use the `Arviz` Bayesian analysis package [161] to extract the credible intervals (CIs) from the highest density posterior intervals (HDPI) of the posterior distributions, where the intervals covering 95% (68%) of the posterior distribution are considered the 95% (68%) CIs. In the Gaussian limit, these 95% (68%) CIs should be interpreted as equivalent to the 95% (68%) Frequentist Confidence Level (CL) two-sided bounds. `HEPfit` [162] code was used to validate the fits. Given that current bounds on these operators are rather weak, one may wonder about the uncertainty in our fits associated to the truncation of the EFT. Note that, since the four-quark operators only enter into the virtual corrections at NLO, Higgs production and decay contain only linear terms in $1/\Lambda^2$ in the corresponding Wilson coefficients, i.e. the quadratic terms coming from squaring the amplitudes are technically of next-to-NLO. Hence, the quadratic effects in the signal strengths come from not linearising the corrections to the product $\sigma_{\text{Prod}} \times \text{BR}$. These effects have been invistigated, and found to have a negligible effect on the fit. The operators of single chirality $\mathcal{O}_{tt}$ and $\mathcal{O}_{QQ}^{(1)/(3)}$ were not included in the fit, as their effect on Higgs rates is limited to small δR for $t\bar{t}h$. Thus, they cannot be contained simultaneously with C_ϕ using single Higgs data.

5.3.1 Fit results

In Figure 5.6 and Figure 5.7 the 68% and 95% highest posterior density contours of the two-parameter posterior distributions and their marginalisation for the two-parameter fits involving C_ϕ and one of the four-heavy quark Wilson coefficients, evaluated at the scale $\Lambda = 1$ TeV for Run-II LHC measurements . Both linearised and quadratically truncated δR_{λ_3} fits are shown, and we observe that the 95% CI bounds (shown on top of the panels) and correlations depends on the truncation.

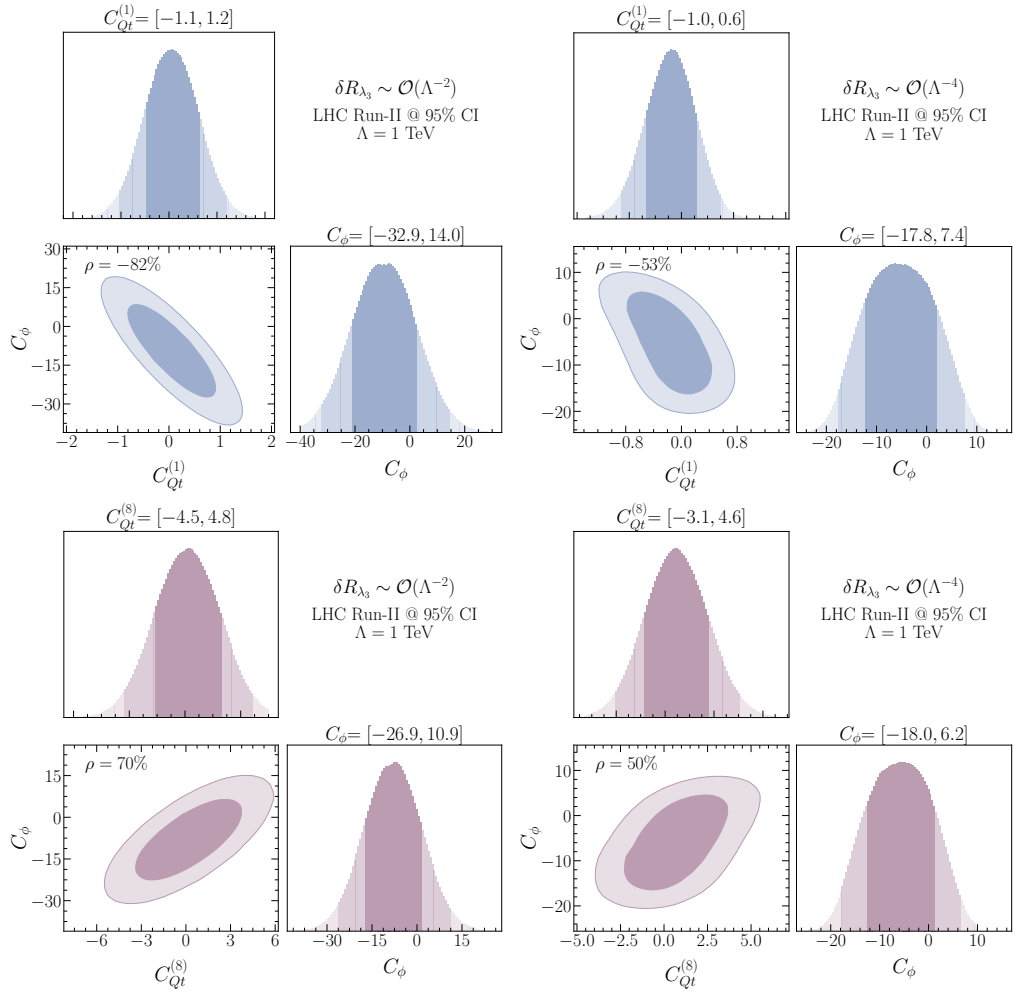

Figure 5.6. The 68% and 95% highest density posterior contours of the posterior distribution of C_ϕ with $C_{Qt}^{(1)}$ (up) and C_ϕ with $C_{Qt}^{(8)}$ (down) with the marginalised one-dimensional posteriors for each of the Wilson coefficients and their 68% and 95% HDPIs (shown above in numbers the 95% CI bounds). The limits correspond to values of the Wilson coefficients evaluated at the scale $\Lambda = 1$ TeV. On the left we used the linear scheme in δR_{λ_3} while on the right we keep up to quadratic terms in δR_{λ_3}.

We observe that the four-fermion operators are strongly correlated with Higgs self-coupling modifier $\mathcal{O}_\phi$, in the linear fit. With Pearson's correlation of $\gtrsim 0.7$ with p-value $< 10^{-4}$. In the case of quadratic δR_{λ_3} fit, we observe diminished Pearson correlation, but in this scenario Pearson's correlation test is not particularly applicable, as we have

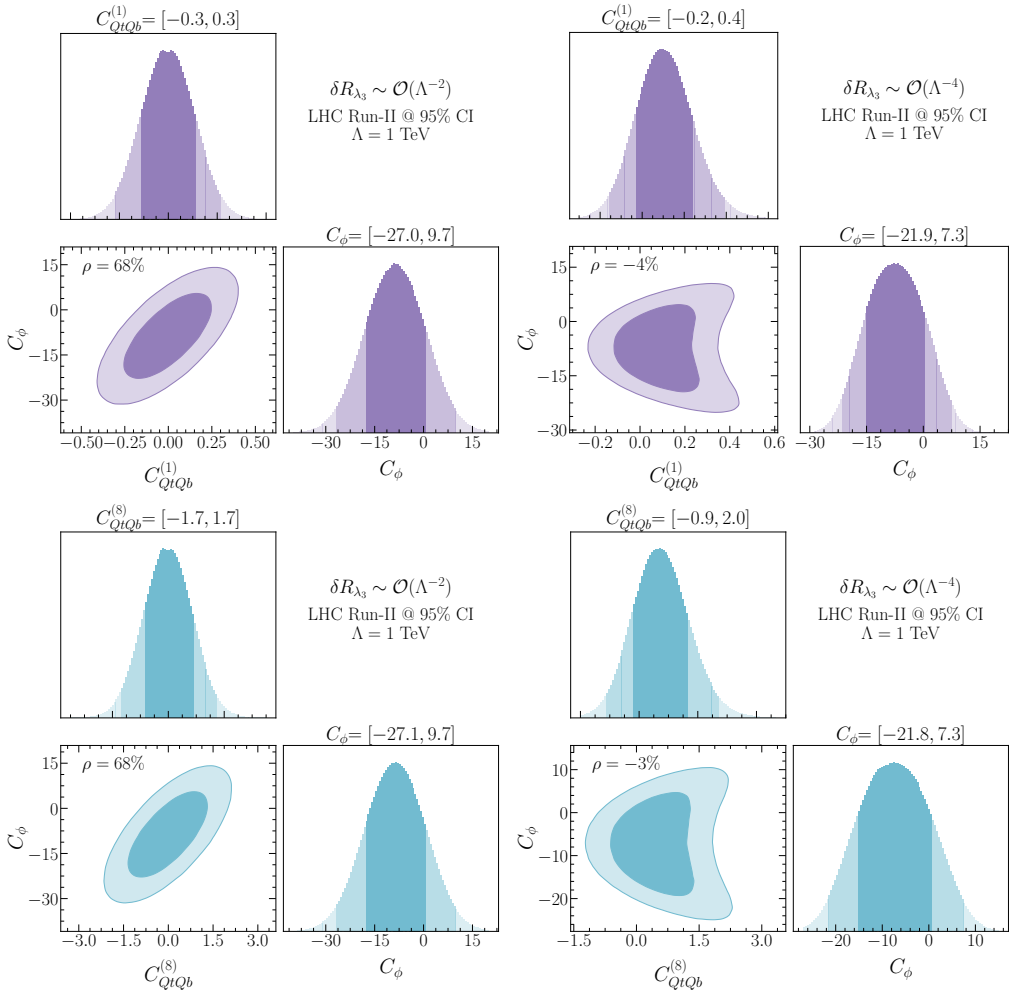

Figure 5.7. The 68% and 95% highest density posterior contours of the posterior distribution of C_ϕ with $C^{(1)}_{QtQb}$ (up) and C_ϕ with $C^{(8)}_{QtQb}$ (down) with the marginalised one-dimensional posteriors for each of the Wilson coefficients. and their 68% and 95% HDPIs (shown above in numbers the 95% CI bounds). The limits correspond to values of the Wilson coefficients evaluated at the scale $\Lambda = 1$ TeV. Similar to $C^{(1),(8)}_{Qt}$, the left plot shows the linearised δR_{λ_3} while the right one shows the quadratic scheme in the trilinear Higgs self-coupling modification. Due to the degeneracy between these Wilson coefficients the posterior contours and their marginalised intervals look very similar for both of them (except for the range they cover).

non-linear relation between the variables.

The two-parameter fit results for thee four-fermion Wilson coefficients are mesmerised in the forest plots in Figure 5.8 marginalising the posteriors distributions over C_ϕ. The

finite effects were isolated by preforming fits with δR^{fin} only. The finite effects are small for $O_{QtQb}^{(1)/(8)}$ but dominant for the four-top operators $O_{Qt}^{(1)/(8)}$mainly coming from $t\bar{t}h$. The effect of EFT truncations of δR_{λ_3} can also be observed as shifts in the mean value for the Wilson coefficients, but the 95% CI's themselves are not significantly affected. In these plots, the fits results from this study are also confronted with the limits obtained from fits to top data [136, 137, 140, 163–165]. Showing that when the Wilson coefficient running is taken into an account, the 95% CI bounds obtained from Higgs data are consistently stronger than the ones from top data.

In Figure 5.9 the fit results for C_ϕ after marginalising over the four-fermion Wilson coefficients in both EFT truncations schemes of δR_{λ_3}. In addition to a single parameter fit for C_ϕ. Additionally the current 95 % CL bound on C_ϕ extracted from Higgs pair production search using th final state $b\bar{b}\gamma\gamma$ preformed by ATLAS using Run-II data [166], translated from κ formalism.
The mean values and the 95%CI's change depending on the four-fermion Wilson coefficient that was paired with C_ϕ in the two.-parameter fit. As expected, the single parameter fits for C_ϕ yield stronger bound on C_ϕ than the two-parameter fits, thus the inclusion of the four-fermion operators in single Higgs data dilutes C_ϕ bounds . Additionally, the truncation order of δR_{λ_3} appears to have a significant effect on the length of the CI's, with quadratic fits giving more stringent constraint on C_ϕ. Instead, for Higgs pair production is makes only a negligible effect if linear or up to quadratic terms in the EFT expansion are kept for the $C_\phi > 0$ bound, while the bound weakens at linear order in $1/\Lambda^2$ for $C_\phi < 0$ [167]. For instance, the quadratic single parameter fit for C_ϕ is comparable to the direct bound from Higgs pair production. However, this changes dramatically, when one includes the four-fermion operators in a combined fit, and the single Higgs data constraints on C_ϕ become less significant compared to the direct hh bounds.
It should be noted that the strongest bound on the Higgs self-coupling currently comes from the perturbative unitarity bound of ref. [50], as discussed in chapter.

One of the important aspects of multivariate studies is the correlation among variables. Apart from the two-parameter fits discussed above, here we also consider a four-parameter fit to C_ϕ plus the three directions in the four heavy-quark operator parameter space that the Higgs rates are mostly sensitive too, i.e. neglecting $C_{QQ}^{(1),(3)}$ and C_{tt}, and trading $C_{QtQb}^{(1)}$ and $C_{QtQb}^{(8)}$ by C_{QtQb}^{+}. When considering two- or four-parameter fits of C_ϕ and the four-heavy-quark Wilson coefficients, we observe a non-trivial correlation patterns amongst these coefficients. Figure 5.10 illustrates these correlation patterns clearly for the four-parameter fit. We observe that the Wilson coefficients $C_{Qt}^{(1),(8)}$ are strongly correlated because, in analogy to $C_{QtQb}^{(1),(8)}$, they only appear in certain linear combination whenever correcting the Yukawa coupling. However, unlike $C_{QtQb}^{(1),(8)}$ they are not completely degenerate because the main part of the NLO correction to $t\bar{t}h$ does

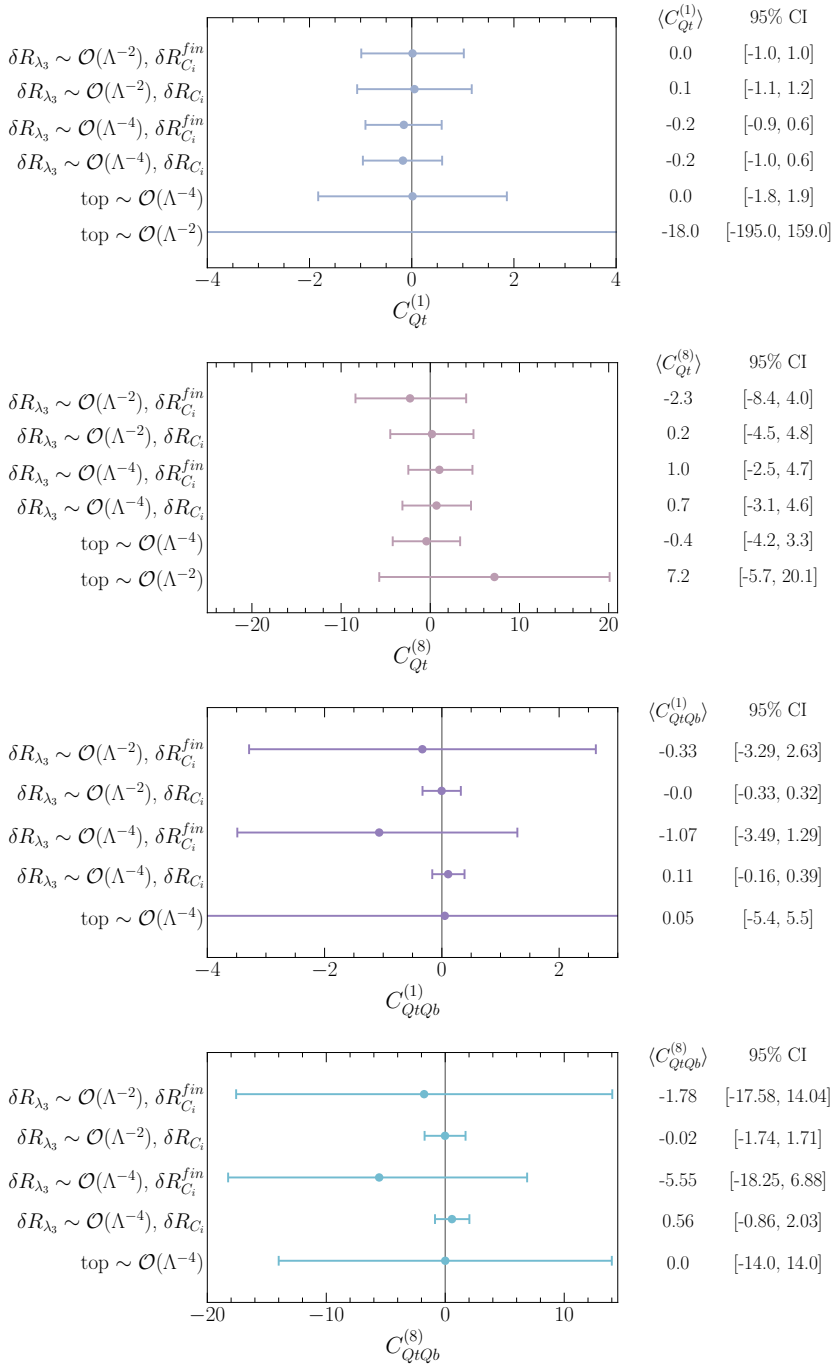

Figure 5.8. Forest plots illustrating the means and 95% CIs of the posteriors built from the four-fermion Wilson coefficients with C_ϕ marginalised. The plots confront also the truncation of the EFT at $\mathcal{O}(1/\Lambda^2)$ and $\mathcal{O}(1/\Lambda^4)$ of δR_{λ_3} as defined in (5.26). The 95% CI bounds stem from Higgs data. The last two rows for each operator show instead the limits obtained by a single parameter fit to top data, linear and quadratic. The top data results are taken from [140] for $C_{Qt}^{(1),(8)}$ and [137] for $C_{QtQb}^{(1),(8)}$.

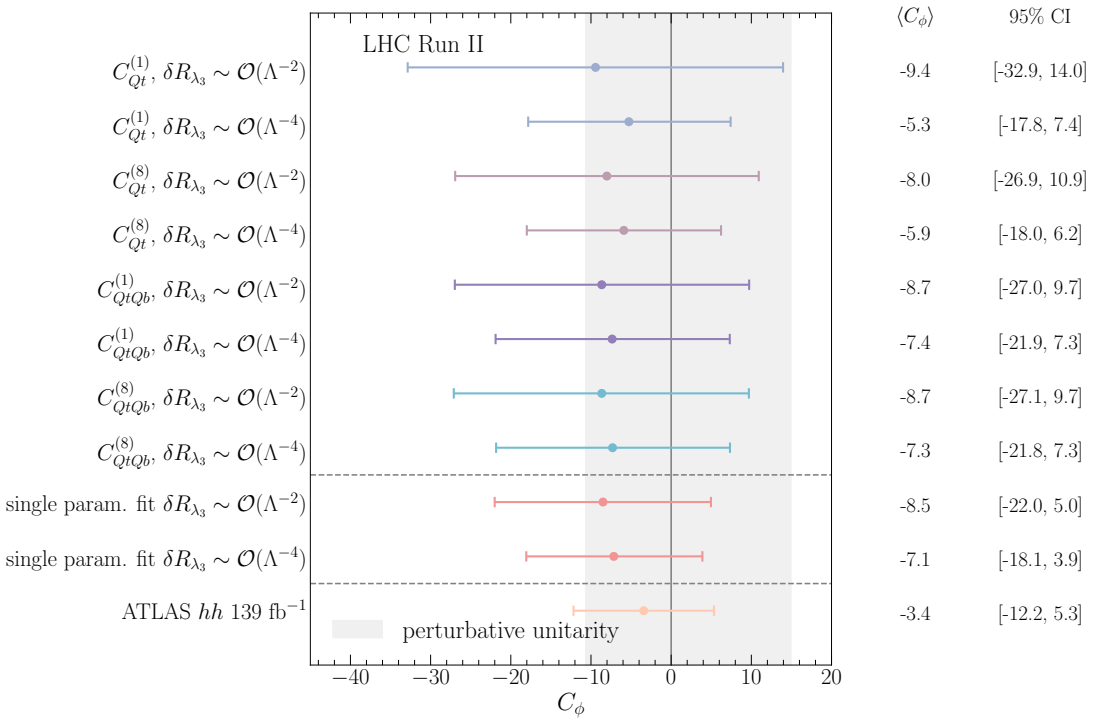

Figure 5.9. A forest plot illustrating the means and 95% CIs of the posteriors built from the C_ϕ in a two-parameter fit with the four-fermion operators marginalised. We compare the fit results for C_ϕ from full run-II Higgs data keeping terms up to $\mathcal{O}(1/\Lambda^2)$ or $\mathcal{O}(1/\Lambda^4)$ in δR_{λ_3}. For comparison, also the 95% CI and means for the single parameter fit for C_ϕ with the same single Higgs data is shown as well as the bounds on C_ϕ from the 139 fb^{-1} search for Higgs pair production [166]. The horizontal grey band illustrates the perturbative unitarity bound [50].

not contain the aforementioned linear combination. The four-parameter fit also reveals that the Wilson coefficients $C_{Qt}^{(1),(8)}$ have a large correlation with C_{QtQb}^{+} because all of the four Wilson coefficients appear in a linear combination in the NLO corrections except for $h \to b\bar{b}$ and $t\bar{t}h$. However, this correlation is not as strong due to the large NLO correction of the Higgs decay $h \to b\bar{b}$ from $C_{QtQb}^{(1),(8)}$. Moreover, the correlation between the four-heavy-quark Wilson coefficients and C_ϕ depends on the δR_{λ_3} truncation.

5.3.2 Prospects for HL-LHC

We now turn to examine the potential of the HL-LHC. For this, we use the CMS projections for the single Higgs signal strengths provided in refs. [89, 158] for a centre-of-mass energy of $\sqrt{s} = 14$ TeV and integrated luminosity of $3\,\text{ab}^{-1}$. We use the projections for the S2 scenario explained in [159]. These assume the improvement on the systematics that is expected to be attained by the end of the HL-LHC physics programme, and that theory uncertainties are improved by a factor of two with respect to current values. These projections are assumed to have their central values in the SM prediction with the total uncertainties summarised in table 2.1 in Appendix **??**.[2]

In Figure 5.11 we confront the results of the fits to Run-2 data with the projections for the HL-LHC for single parameter fits. For the operators $\mathcal{O}_{Qt}^{(1),(8)}$ the constraining power of the HL-LHC is roughly a factor two better as the current bounds we could set from single Higgs data, while for the operators $\mathcal{O}_{QtQb}^{(1),(8)}$ the improvement is a little less. In Figure 5.13 we show the limits on C_ϕ in a single parameter fit for Run-2 and the projections for the HL-LHC including in δR_{λ_3} up to order $\mathcal{O}(1/\Lambda^2)$ or $\mathcal{O}(1/\Lambda^4)$. While for Run-2 data the inclusion of $\mathcal{O}(1/\Lambda^4)$ made a huge difference, this is less pronounced for the HL-LHC projections. Our results are very similar to the projections presented in a κ_λ fit in [168]. We confront this also with data from searches for Higgs pair production 139 fb^{-1} [166] and HL-LHC projections [169] on Higgs pair production, showing that Higgs pair production will still allow to set stronger limits on C_ϕ.

5.4 Summary and discussion

In this paper, we have computed the NLO corrections induced by third generation four-quark operators in Higgs observables that are relevant for its production and decay at the LHC. Our results show that such processes are sensitive to the all possible chiral structures for the third generation four-quark operators in the dimension-six SMEFT, but in different degrees. Operators with different chiralities are, for instance, the only ones that can contribute to Higgs production via gluon fusion, and the decay of the Higgs boson to gluons, photons and bottom quarks pairs. The latter are particularly sensitive to the top-bottom operators $\mathcal{O}_{QtQb}^{(1),(8)}$, which then also significantly affect the

[2] The correlation matrix for the S2 scenario can be found on the webpage [158].

total decay width. In the associate production of a Higgs boson with a top quark pair, on the other hand, all the third generation four-fermion operators enter. Sensitivity to four-quark operators where all fields have the same chirality, however, is only possible for large values of the Wilson coefficients, in a way that they can generate contributions beyond the size of current theory uncertainties. The $t\bar{t}h$ process is also rather important in setting limits on the four-quark operators $\mathcal{O}_{Qt}^{(1)}$ and $\mathcal{O}_{Qt}^{(8)}$, due to the comparatively large NLO corrections they induce in this process with respect to others. It also breaks a degeneracy among the Wilson coefficients of those two operators, which always appear in a single combination for all other processes.

To illustrate the constraining power of single Higgs processes in bounding these four-quark operators, we performed several simplified fits to these interactions and find that the resulting limits from our fits are, in some cases, comparable or better than similar results obtained from top data [137, 140].

We have also performed a combined fit including the above-mentioned four-quark operators and the operator $\left(\phi^\dagger\phi\right)^3$, that modifies the Higgs potential and the trilinear Higgs self-coupling. Due to the lack of powerful constraints from top data, the inclusion of the four-fermion operators diminishes the power of setting limits on the trilinear Higgs self-coupling from single Higgs observables. From our analysis we conclude that, in the absence of strong direct bounds on the third-generation four-quark operators, these should be included into a global fit on Higgs data, when attempting to obtain model-independent bounds on the trilinear Higgs self-coupling. The results of our calculations are presented such that they can be easily used by the reader in truly global fits including all other interactions entering at the LO. We leave this, as well as the inclusion of differential Higgs data, to future work.

Finally, we also illustrated the increase in constraining power expected during the high-luminosity phase of the LHC by presenting the HL-LHC projections of the above-mentioned fits.

Moving beyond hadron colliders, it must be noted that the interplay between the Higgs trilinear and four heavy-quark operators in Higgs processes is expected to be less of an issue at future leptonic Higgs factories, such as the FCC-ee [170, 171], ILC [172, 173], CEPC [174, 175] or CLIC [176, 177]. At these machines, the effects of C_ϕ are still "entangled" with those of the four-fermion operators in the Higgs rates, but only through the decay process, i.e. via the contributions to the BRs. However, Higgs production is purely electroweak, namely via Higgs-strahlung (Zh: $e^+e^- \to Zh$) or W boson fusion, and receives no contributions from the four-quark operators at the same order in perturbation theory where C_ϕ modifies these processes, i.e. NLO. Moreover, at any of these future e^+e^- Higgs factories there is the possibility of obtaining a sub-percent determination of the total Zh cross section at e^+e^- colliders, by looking at events recoiling against the Z decay products with a recoil mass around m_h. This observable is therefore completely insensitive to the four-quark operators, while still receiving NLO

corrections from C_ϕ. Although, in practice, in a global fit one needs to use data from all the various Higgs rates at two different energies to constrain all possible couplings entering at LO in the Higgs processes and also obtain a precise determination of C_ϕ [178], the previous reasons should facilitate the interpretation of the single-Higgs bounds on the Higgs self-coupling at e^+e^- machines.

We conclude this paper with a few words on the relevance of the results presented here when interpreted from the point of view of specific models of new physics. In particular, one important question is *are there models where one expects large contributions to four-top operators while all other interactions entering in Higgs processes are kept small?* Indeed, large contributions to four-top operators can be expected in various BSM scenarios.[3] For instance, in Composite Higgs Models, in which the top quark couples to the strong dynamics by partial compositeness, one expects on dimensional grounds that some of the four-top quark operators are of order $1/f^2$, where f indicates the scale of strong dynamics [179]. By its own nature, however, Composite Higgs models also predict sizeable contributions to the single Higgs couplings $\sim 1/f^2$. While, in general, sizeable modifications of the Higgs interactions are typically expected in scenarios motivated by "naturalness", this is not necessarily the case in other scenarios. It is indeed possible to think of simple models where modifications of the Higgs self-interactions or contributions to four-quark operators are the only corrections induced by the dimension-six interactions at tree level, see [180]. Thinking, for instance, in terms of scalar extensions of the SM, there are several types of colored scalars whose tree-level effects at low energies can be represented by four-quark operators only, e.g. for complex scalars in the $(6,1)_{\frac{1}{3}}$ and $(8,2)_{\frac{1}{2}}$ SM representations (Ω_1 and Φ in the notation of [180]). If these colored states are the only moderately heavy new particles, our results can provide another handle to constrain such extensions. One must be careful, though, as a consistent interpretation of our results for any such models would require to include higher-order corrections in the matching to the SMEFT. At that level, as shown e.g. by the recent results in [181], multiple contributions that modify Higgs processes at LO are generated at the one-loop level, and are therefore equally important as the NLO effects of the (tree-level) generated four-quark operators.[4] In any case, one must note that, even if similar size contributions to single Higgs processes are generated, the four-top or Higgs trilinear effects can provide extra information on the model. For instance, in some of the most common scalar extensions of the SM, with an extra Higgs doublet, $\varphi \sim (1,2)_{\frac{1}{2}}$, tree-level contributions to some of the four-heavy-quark operators discussed in this paper are generated

[3] Generically, models where four-top interactions are much larger than four-fermion operators of the first and second generation can be easily conceived from some UV dynamics coupling mostly to the third generation of quarks hence respecting the Yukawa hierarchies.

[4] Furthermore, given that some SMEFT interactions induce tree-level contributions to Higgs processes that in the SM are generated at the loop level, e.g. $\mathcal{O}_{\phi G}$ in gluon fusion, a consistent interpretation in terms of new physics models may require to include up to two-loop effects in the matching for such operators, for which there are currently no results or tools available.

together with modifications on the Higgs trilinear self-coupling. These two effects are independent but they are both correlated with the, also tree level, modifications of the single Higgs couplings. Essentially, the LO effects on Higgs observables are proportional to $\lambda_\varphi y_\varphi^f$, where λ_φ is the scalar interaction strength of the $(\varphi^\dagger\phi)(\phi^\dagger\phi)$ operator and y_φ^f the new scalar Yukawa interaction strength, whereas the NLO effects are proportional to the square of each separate coupling. Hence, these effects might help to resolve (even if only weakly) the flat directions in the model parameter space that would appear in a LO global fit. At the end of the day, for a proper interpretation of the SMEFT results in terms of the widest possible class of BSM models, all the above simply remind us of the importance of being global in SMEFT analyses, to which our work contributes by including effects in Higgs physics that enter at the same order in perturbation theory as modifications of the Higgs self-coupling.

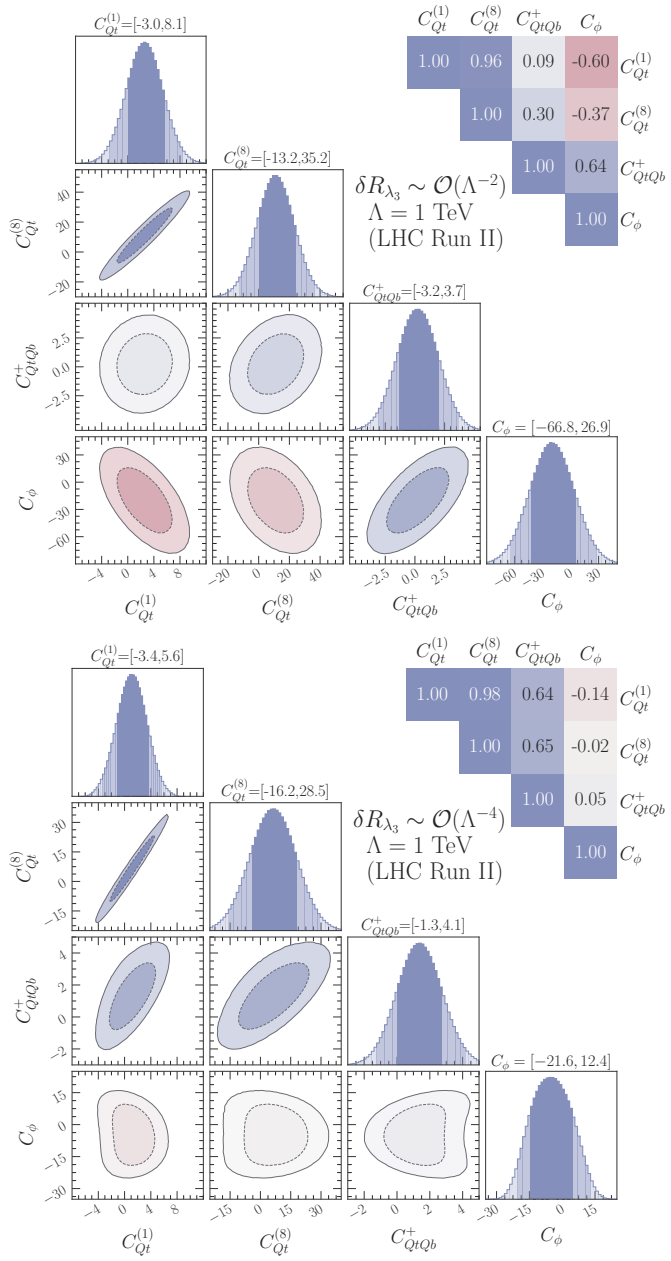

Figure 5.10. The marginalised 68% and 95% HDPI's for the four-parameter fits including the different four-quark Wilson coefficients and C_ϕ. The numbers above the plots show the 95% CI bounds while the correlations are given on the top-right side. These limits correspond to values of the Wilson coefficients evaluated at the scale $\Lambda = 1$ TeV. The upper panel shows the fit including up to $\mathcal{O}(1/\Lambda^2)$ in δR_{λ_3} while the lower one shows the fit with including also $\mathcal{O}(1/\Lambda^4)$.

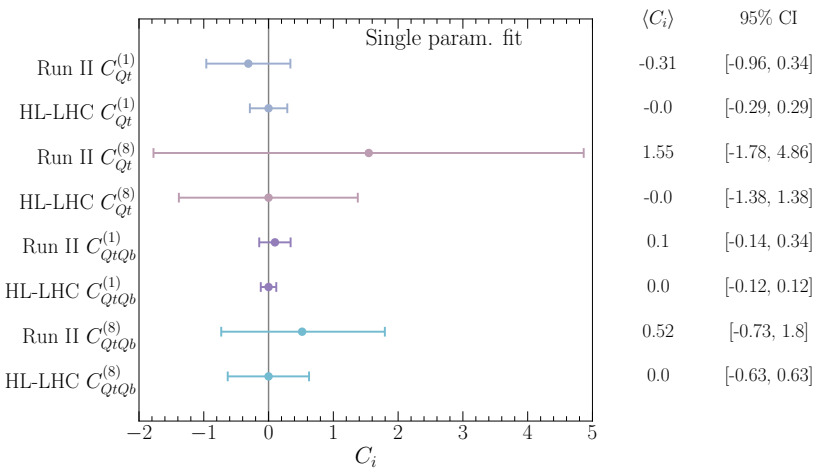

Figure 5.11. Results of a single parameter fit showing the improvement in constraining power of the HL-LHC over the current bounds from Run-2 data. The limits correspond to values of the Wilson coefficients evaluated at the scale $\Lambda = 1$ TeV.

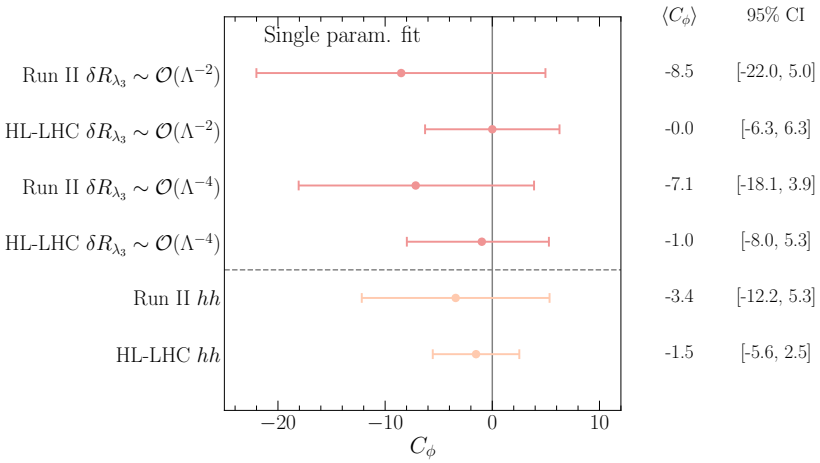

Figure 5.12. A forest plot illustrating the means and 95% CIs of the posteriors built from the C_ϕ in a single-parameter fit, showing also the differences in including terms of $\mathcal{O}(1/\Lambda^2)$ or up to $\mathcal{O}(1/\Lambda^4)$ in the definition of δR_{λ_3}. For comparison, also the limits and projections from searches for Higgs pair production are shown.

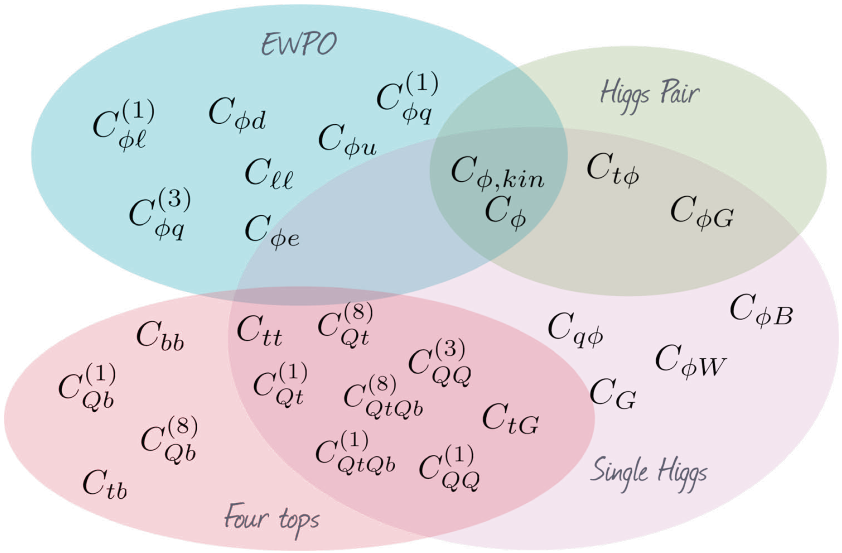

Figure 5.13. A forest plot illustrating the means and 95% CIs of the posteriors built from the C_ϕ in a single-parameter fit, showing also the differences in including terms of $\mathcal{O}(1/\Lambda^2)$ or up to $\mathcal{O}(1/\Lambda^4)$ in the definition of δR_{λ_3}. For comparison, also the limits and projections from searches for Higgs pair production are shown.

6 Virtual two-loop calculation of Zh production via gluon fusion

As we have seen in the previous sections, Higgs couplings to the weak vector bosons, i.e. Z and W is approaching the precision level. Moreover, the associated Higgs production with these bosons is the first channel used to observer the Higgs decaying into beauty quarks $h \to b\bar{b}$ by both ATLAS and CMS [182, 183]. Hence, the Vh Higgs production channels are important channels to look for in the future runs of the LHC for better measurement of the VVh coupling as well as Higgs coupling to the beauty quark. As the statistical and systematic uncertainties coming from the experimental setup of the LHC will be eventually reduced in the future runs, due to higher integrated luminosity, upgraded detectors and improved analysis techniques. There is an exigency to reduce theoretical uncertainties emerging from the perturbative calculations of cross-sections. In order to accomplish that, one should include more terms in the perturbative expansion in the couplings, particularly the strong coupling α_s. In this chapter, we are interested in the channel $pp \to Zh$, which is quark-initiated tree-level process at LO interpreted as **Drell-Yan process** [184, 185]. This process has been computed up to next-to-next-to-leading-order (NNLO) in QCD ($\sim \alpha_s^2$), and at next-to-leading-order (NLO) in the EW interactions ($\sim \alpha^2$) [186].

Despite arising for the first time at NNLO in perturbation theory to the partonic cross-section, the gluon fusion channel $gg \to Zh$ has a non-negligible contribution to the hadronic cross-section $pp \to Zh$, which could reach $> 16\%$ of the total cross-section contribution at 14 TeV [159], see Figure 6.1. The contribution becomes more significant when looking at large invariant mass bins in the differential cross-section. This is due to the significant abundance of gluons at the LHC for large energy faction Q as well as the extra enhancement coming from the top quark initiated contribution near the $t\bar{t}$ threshold [187]. The gluon fusion channel has a higher scale uncertainties than the quark induced one,as one can see from the uncertainty band of Figure 6.1 predominantly coming from the gluon fusion part σ_{gg}. With that in mind, and the absence of gluon fusion channel for Wh channel, the Zh channel has higher theoretical uncertainties. This further motivates NLO calculation of the $gg \to Zh$ channel to higher orders in perturbation theory, such that these uncertainties get reduced. Facilitating the precision measurement of the Zh channel at the future LHC runs, which in term provides better constraints on several observables, such as sign and magnitude of the top Yukawa coupling, dipole operators [188]. Additionally, this channel can receive contributions from new particles

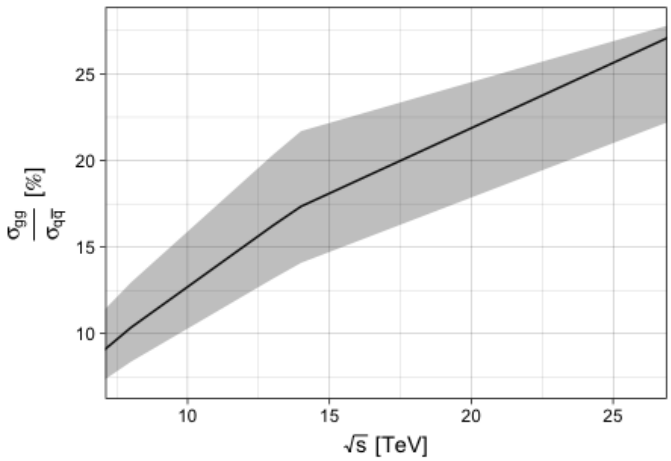

Figure 6.1. The ratio of the LO gluon fusion production cross-section $gg \to Zh$ (σ_{gg}) with respect to the NLO Drell-Yan process $q\bar{q} \to Zh$ cross-section ($\sigma_{q\bar{q}}$) at a pp collider with centre-of-mass energy $\sqrt{s}$. The error band captures the total theoretical uncertainties on both cross-sections dominated by σ_{gg} .

[189], particularly at the large invariant-mass region where the gluon fusion contribution becomes more important. Therefore, better understanding of the SM prediction of the Zh gluon fusion channel is crucial for both the SM precision measurements of Higgs production within the SM and for testing NP in this channel, e.g. new vector-like leptons.

The leading order (LO) contribution to the $gg \to Zh$ amplitude, given by one-loop diagrams, was computed exactly in refs.[190, 191]. However, for the NLO, the virtual corrections contain multi-scale two-loop integrals some of which are still not known analytically (for the box diagram). The first computation of the NLO terms has been done by [192] using an asymptotic expansion in the limit $m_t \to \infty$ and $m_b = 0$, and pointed to a K-factor of about ~ 2. Later, the computation has been improved via soft gluon resummation, and including NLL terms found in ref.[193], the NLL terms has been matched to the fixed NLO computation of [192]. Top quark mass effects to the $gg \to Zh$ process were first implemented using a combination of large-m_t expansion (LME) and Padé approximants [194]. A data-driven approach to extract the gluon fusion dominated non-Drell-Yan part of Zh production using the known relation between Wh and Zh associated production when only the Drell-Yan component of the two processes is considered has been investigated in ref.[195]. The differential distributions of $gg \to Zh$ at NLO was studied in ref.[196] via LO matrix element matching.

More recent studies of the NLO virtual corrections to this process were based on the high-energy (HE) expansion improved by Padé approximants with the LME, which

extended the validity range of the HE expansion [197]. However, this expansion is only valid for in the invariant mass region $\sqrt{\hat{s}} \gtrsim 750\,\text{GeV}$ and $\sqrt{\hat{s}} \lesssim 350\,\text{GeV}$, which only covers $\sim 32\%$ of the hadronic cross section. Additionally, numerical computation of the two-loop virtual corrections, though implemented exactly in [198], are rather slow for practical use in MC simulations. This highlights the importance of an analytical method that can cover the remaining region of the cross-section and can be merged with the HE expansion via Padé approximants. Fortunately, the two-loop corrections to the triangle diagrams can be computed exactly. And the loop integrals appearing in the box correction having no analytic expression can be expanded in small Z (or Higgs) transverse momentum, p_T. This method was first used for Higgs pair production in [199], to compute the NLO virtual corrections to the box diagrams in the forward kinematics.

This chapter is structured as follows : In section 6.1 contains the general notation we have used for the gluon fusion Zh process calculation. Then, in subsection 6.1.1 the transverse momentum expansion method is discussed. Calculation of the LO form-factors in the transverse momentum expansion is illustrated in section 6.2 as a proof of concept for the p_T-expansion technique. Outline of the two-loop calculation is discussed in section 6.3. Finally, in section 6.4, the results of our calculation are shown with concluding remarks at the end.

This chapter is a slightly modified version of [200] published in JHEP and has been reproduced here with the permission of the copyright holder and the co-authors.

6.1 General notation

The amplitude $g_a^\mu(p_1)g_b^\nu(p_2) \to Z^\rho(p_3)h(p_4)$ can be written as

$$\mathcal{A} = i\sqrt{2}\frac{m_Z G_F \frac{\alpha_s^0}{4\pi}(\mu_R)}{\pi}\delta_{ab}\epsilon_\mu^a(p_1)\epsilon_\nu^b(p_2)\epsilon_\rho(p_3)\hat{\mathcal{A}}^{\mu\nu\rho}(p_1,p_2,p_3), \tag{6.1}$$

$$\hat{\mathcal{A}}^{\mu\nu\rho}(p_1,p_2,p_3) = \sum_{i=1}^{6}\mathcal{P}_i^{\mu\nu\rho}(p_1,p_2,p_3)\mathcal{A}_i(\hat{s},\hat{t},\hat{u},m_t,m_h,m_Z), \tag{6.2}$$

where μ_R is the renormalisation scale and $\epsilon_\mu^a(p_1)\epsilon_\nu^b(p_2)\epsilon_\rho(p_3)$ are the polarization vectors of the gluons and the Z boson, respectively. It is possible to decompose the amplitude into a maximum of 6 Lorentz structures encapsulated by the tensors $\mathcal{P}_i^{\mu\nu\rho}$. Due to the presence of the γ_5 these projectors are proportional to the Levi-Civita total anti-symmetric tensor $\epsilon^{\alpha\beta\gamma\delta}$. One can choose to an orthogonal basis explicitly shown in **??**, such that

$$\mathcal{P}_i^{\mu\nu\rho}\mathcal{P}_{j\,\mu\nu\rho} = 0, \quad \text{for } i \neq j \tag{6.3}$$

By this choice one obtains unique form factors corresponding to each projector

$$\mathcal{A}_i(\hat{s},\hat{t},\hat{u},m_t,m_h,m_Z), \tag{6.4}$$

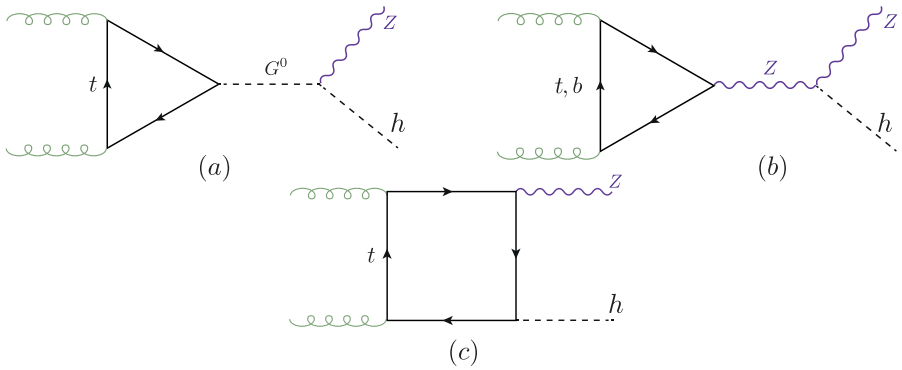

Figure 6.2. Feynman diagrams type for the LO $gg \to Zh$ process. The triangle diagrams in a general ξ gauge involve Z and the neutral Goldstone G^0 propagators.

that are multivariate complex functions of the top (m_t), Higgs (m_h) and Z (m_Z) bosons masses, and of the partonic Mandelstam variables

$$\hat{s} = (p_1 + p_2)^2, \quad \hat{t} = (p_1 + p_3)^2, \quad \hat{u} = (p_2 + p_3)^2, \tag{6.5}$$

where $\hat{s} + \hat{t} + \hat{u} = m_Z^2 + m_h^2$ and all the momenta are considered to be incoming. The form-factors $\mathcal{A}_i$ can be perturbatively expanded in orders of α_s,

$$\mathcal{A}_i = \sum_{k=0} \left(\frac{\alpha_s}{\pi}\right)^k \mathcal{A}_i^{(k)} \tag{6.6}$$

Where $\mathcal{A}_i^{(0)}$ and $\mathcal{A}_i^{(1)}$ are the LO and NLO terms, respectively. Using Fermi's Golden Rule, we can write thee Born partonic cross-section as

$$\hat{\sigma}^{(0)}(\hat{s}) = \frac{m_Z^2 G_F^2 \alpha_s(\mu_R)^2}{64\hat{s}^2(2\pi)^3} \int_{\hat{t}^-}^{\hat{t}^+} d\hat{t} \sum_i \left|\mathcal{A}_i^{(0)}\right|^2, \tag{6.7}$$

where $\hat{t}^{\pm} = [-\hat{s} + m_h^2 + m_Z^2 \pm \sqrt{(\hat{s} - m_h^2 - m_Z^2)^2 - 4m_h^2 m_Z^2}\,]/2$.

The LO has two sets of diagrams, the triangle, and box diagrams shown in Figure 6.2. In (a), the triangle diagrams contains a neutral Goldstone boson G^0, instead in (b) the Z boson is mediated. The interplay between these two diagram types depends on the ξ gauge. Moreover, the Z boson is strictly off-shell, due to Furry's theorem. In the Landau gauge the Z- mediated diagrams will also vanish, this can be seen by considering the subamplitude ggZ^* which in the Landau gauge can be related to the decay of a massive vector boson with mass $\sqrt{\hat{s}}$ into two massless ones, a process that is forbidden by the

Landau-Yang theorem [201, 202]. The triangle diagrams are also proportional to the mass difference between the up and down type quarks. In this calculation, the first and second generation quarks are assumed to be massless, as well as the b quark, hence light quarks loops do not contribute to this process. The same would apply to the box diagrams (c), as they are proportional to the quark Yukawa coupling, and vanish in the massless quarks case. Moreover, triangle diagrams with $b-$ quark loops contribute to $\sim 1\%$ of the total amplitude, computed in the limit $m_b \to 0$.

6.1.1 The transverse momentum expansion

Choosing to expand in small p_T of the Z boson, the first step is expressing p_T in terms of the Mandelstam variables and masses

$$p_T^2 = \frac{\hat{t}\hat{u} - m_Z^2 m_h^2}{\hat{s}}. \tag{6.8}$$

From eq.(6.8), together with the relation between the Mandelstam variables, one finds

$$p_T^2 + \frac{m_h^2 + m_Z^2}{2} \leq \frac{\hat{s}}{4} + \frac{\Delta_m^2}{\hat{s}}, \tag{6.9}$$

where $\Delta_m = (m_h^2 - m_Z^2)/2$. Eq.(6.9) implies $p_T^2/\hat{s} < 1$ that, together with the kinematical constraints $m_h^2/\hat{s} < 1$ and $m_Z^2/\hat{s} < 1$. With these relations in mind, one can expand the amplitudes in terms of small $p_T^2/\hat{s}$, $m_h^2/\hat{s}$ and $m_Z^2/\hat{s}$, which is technically valid throughout the whole phase space, contrary to the LME and HE limits. The caveat for this expansion is that, the amplitude does not depend on p_T explicitly. Instead, one would expand in the reduced Mandelstam variables $t'/s' \ll 1$ or $u'/s' \ll 1$, defined as

$$s' = p_1 \cdot p_2 = \frac{\hat{s}}{2}, \quad t' = p_1 \cdot p_3 = \frac{\hat{t} - m_Z^2}{2}, \quad u' = p_2 \cdot p_3 = \frac{\hat{u} - m_Z^2}{2} \tag{6.10}$$

and satisfy

$$s' + t' + u' = \Delta_m. \tag{6.11}$$

The choice of the expansion parameter t' or u' depends whether one expands in the forward or backwards kinematics. Because the process $gg \to Zh$, has two particles in the final states with different masses, the amplitude is not symmetric under the their exchange. One therefore cannot compute the cross-section by integrating only the forward-expanded amplitude [200], contrary what has been done for the Higgs pair [199]. In order to overcome this issue, one could further examine the projectors in **??** and observe that they can be split into symmetric and anti-symmetric parts with respect to the exchange $t' \leftrightarrow u'$. Then, expand the symmetric part in the forward kinematics, like the Higgs pair case. As for the anti-symmetric part, the antisymmetric factor is simply extracted by multiplying the form-factors by $1/(\hat{t} - \hat{u})$, written as $1/(2s' - 4t' - 2\Delta_m)$,

then perform the expansion in the forward kinematics and finally multiply back by $(\hat{t}-\hat{u})$.

In order to implement the p_T-expansion at the Feynman diagrams level we start by splitting the momenta into longitudinal and transverse with respect to the beam direction, by introducing the vector [199],

$$r^\mu = p_1^\mu + p_3^\mu, \tag{6.12}$$

which satisfies

$$r^2 = \hat{t}, \quad r \cdot p_1 = \frac{\hat{t} - m_Z^2}{2}, \quad r \cdot p_2 = -\frac{\hat{t} - m_h^2}{2}, \tag{6.13}$$

and hence can be also written as

$$r^\mu = -\frac{\hat{t} - m_h^2}{\hat{s}} p_1^\mu + \frac{\hat{t} - m_Z^2}{\hat{s}} p_2^\mu + r_\perp^\mu = \frac{t'}{s'}\left(p_2^\mu - p_1^\mu\right) - \frac{\Delta_m}{s'} p_1^\mu + r_\perp^\mu, \tag{6.14}$$

where

$$r_\perp^2 = -p_T^2. \tag{6.15}$$

substituting the definition of p_T from eq.(6.8) one obtains

$$t' = -\frac{s'}{2}\left\{1 - \frac{\Delta_m}{s'} \pm \sqrt{\left(1 - \frac{\Delta_m}{s'}\right)^2 - 2\frac{p_T^2 + m_Z^2}{s'}}\right\} \tag{6.16}$$

implying that the expansion in small p_T (the minus sign case in eq.(6.16)) can be realized at the level of Feynman diagrams, by expanding the propagators in terms of the vector r^μ around $r^\mu \sim 0$ or, equivalently, $p_3^\mu \sim -p_1^\mu$, see eq.(6.14).

6.2 Born cross-section in the p_T-expansion

As a baseline test for the validity and convergence behaviour of the p_T expansion we start by computing the LO amplitude, and consequently the Born partonic cross-section in the p_T expansion then compare it with the exact results found in [190, 191] .
Starting by defining the one-loop functions appearing in the similar calculation of the Born cross-section for $gg \to hh$ in the same expansion carried out in ref. [199]

$$B_0[\hat{s}, m_t^2, m_t^2] \equiv B_0^+, \qquad B_0[-\hat{s}, m_t^2, m_t^2] \equiv B_0^-, \tag{6.17}$$

$$C_0[0, 0, \hat{s}, m_t^2, m_t^2, m_t^2] \equiv C_0^+, \qquad C_0[0, 0, -\hat{s}, m_t^2, m_t^2, m_t^2] \equiv C_0^- \tag{6.18}$$

$$B_0[q^2, m_1^2, m_2^2] = \frac{1}{i\pi^2}\int \frac{d^n k}{\mu^{n-4}} \frac{1}{(k^2 - m_1^2)((k+q)^2 - m_2^2)}, \tag{6.19}$$

$$C_0[q_a^2, q_b^2, (q_a+q_b)^2, m_1^2, m_2^2, m_3^2] = \frac{1}{i\pi^2}\int \frac{d^dk}{\mu^{d-4}} \frac{1}{[k^2-m_1^2][(k+q_a)^2-m_2^2][(k-q_b)^2-m_3^2]} \tag{6.20}$$

are the Passarino-Veltman functions [203], with d the dimension of spacetime and μ the 't Hooft mass. There are only two non-vanishing form-factors at LO, one is symmetric $\mathcal{A}_2$, and the other is antisymmetric $\mathcal{A}_6$, in the p_T-expansion, these form-factors are give by, up to order $\mathcal{O}(p_T^2)$

$$\mathcal{A}_2^{(0,\triangle)} = -\frac{p_T}{\sqrt{2}\,(m_Z^2+p_T^2)}(\hat{s}-\Delta_m)\,m_t^2 C_0^+, \tag{6.21}$$

$$\begin{aligned}
\mathcal{A}_2^{(0,\square)} &= \frac{p_T}{\sqrt{2}\,(m_Z^2+p_T^2)}\Bigg\{ \\
&\left(m_t^2 - m_Z^2\frac{\hat{s}-6m_t^2}{4\hat{s}} - p_T^2\frac{12m_t^4-16m_t^2\hat{s}+\hat{s}^2}{12\hat{s}^2}\right)B_0^+ \\
&- \left(m_t^2 - \Delta_m\frac{m_t^2}{(4m_t^2+\hat{s})} + m_Z^2\frac{24m_t^4-6m_t^2\hat{s}-\hat{s}^2}{4\hat{s}\,(4m_t^2+\hat{s})} - \right. \\
&\qquad \left. p_T^2\frac{48m_t^6-68m_t^4\hat{s}-4m_t^2\hat{s}^2+\hat{s}^3}{12\hat{s}^2\,(4m_t^2+\hat{s})}\right)B_0^- \\
&+ \left(2m_t^2 - \Delta_m + m_Z^2\frac{3m_t^2-\hat{s}}{\hat{s}} + p_T^2\frac{3m_t^2\hat{s}-2m_t^4}{\hat{s}^2}\right)m_t^2\,C_0^- \\
&+ \left(\hat{s}-2m_t^2 + m_Z^2\frac{\hat{s}-3m_t^2}{\hat{s}} + p_T^2\frac{2m_t^4-3m_t^2\hat{s}+\hat{s}^2}{\hat{s}^2}\right)m_t^2\,C_0^+ \\
&+ \log\left(\frac{m_t^2}{\mu^2}\right)\frac{m_t^2}{(4m_t^2+\hat{s})}\left(\Delta_m + 2m_Z^2 + p_T^2\frac{2\hat{s}-2m_t^2}{3\hat{s}}\right) \\
&- \Delta_m\frac{2m_t^2}{(4m_t^2+\hat{s})} + m_Z^2\frac{\hat{s}-12m_t^2}{4\,(4m_t^2+\hat{s})} + p_T^2\frac{8m_t^4-2m_t^2\hat{s}+\hat{s}^2}{4\hat{s}(4m_t^2+\hat{s})}\Bigg\},
\end{aligned} \tag{6.22}$$

and

$$\mathcal{A}_6^{(0,\triangle)} = 0, \tag{6.23}$$

$$\mathcal{A}_6^{(0,\square)} = \frac{\hat{t}-\hat{u}}{\hat{s}^2}\, p_T \left[\frac{m_t^2}{2}\left(B_0^- - B_0^+\right) - \frac{\hat{s}}{4} \right.$$
$$\left. - \frac{2m_t^2+\hat{s}}{2} m_t^2\, C_0^- + \frac{2m_t^2-\hat{s}}{2} m_t^2\, C_0^+ \right], \tag{6.24}$$

where these form-factors were divided into triangle ($\triangle$) and box ($\square$) contributions, and B_0 functions are understood as the finite part of the integrals on the right hand side of eq.(6.19).

Using several truncations of the p_T-expansion, and comparing it to the exact LO result, one can see in Figure 6.3 the exact Born partonic LO cross section (red line) as a function of the invariant mass of the Zj system, M_{Zh}, in comparison to the p_T-expansions. For the numerical evaluation of the cross section here and in the following, we used as SM input parameters

$$m_Z = 91.1876 \text{ GeV}, \quad m_h = 125.1\,\text{GeV}, \quad m_t = 173.21 \text{ GeV},$$
$$m_b = 0 \text{ GeV}, \quad G_F = 1.16637 \text{ GeV}^{-2}, \quad \alpha_s(m_Z) = 0.118.$$

From the ratio plotted in the lower panel of Figure 6.3 , we observe that the $\mathcal{O}(p_T^0)$ expansion is in good agreement with the exact result when $M_{Zh} \lesssim 2m_t$. Inclusion of higher order terms up tp $\mathcal{O}(p_T^6)$ extended the validity of the expansion to reach $M_{Zh} \lesssim 750\,\text{GeV}$. This is the similar behaviour seen in [199] for Higgs pair. Therefore, one would expect the p_T-expanded two-loop virtual correction to be an accurate approximation with the exact (numerical) result for the region of the invariant mass of $M_{Zh} \sim 700-750\,\text{GeV}$. Similar conclusions can be seen more explicitly in Table 6.1, where it is shown that the partonic cross-section at $\mathcal{O}(p_T^4)$ agrees with the full result for $M_{ZH} \lesssim 600\,\text{GeV}$ on the permille level and the agreement further improves when $\mathcal{O}(p_T^6)$ terms are included.

6.3 NLO calculation

The virtual two-loop corrections to $gg \to Zh$ are shown in Figure 6.4, which involve corrections to the triangle topology in (a) and (b). The corrections to the box topology in (c) and a new topology , dented by double triangle in (d). Both two-loop corrections to the triangles, and the double triangle diagrams can be computed exactly analytically. However, the two-loop box diagrams contain master-integrals (MI's) that have no analytic solutions, so far. The two-loop box diagrams will be computed in the p_T-expansion.

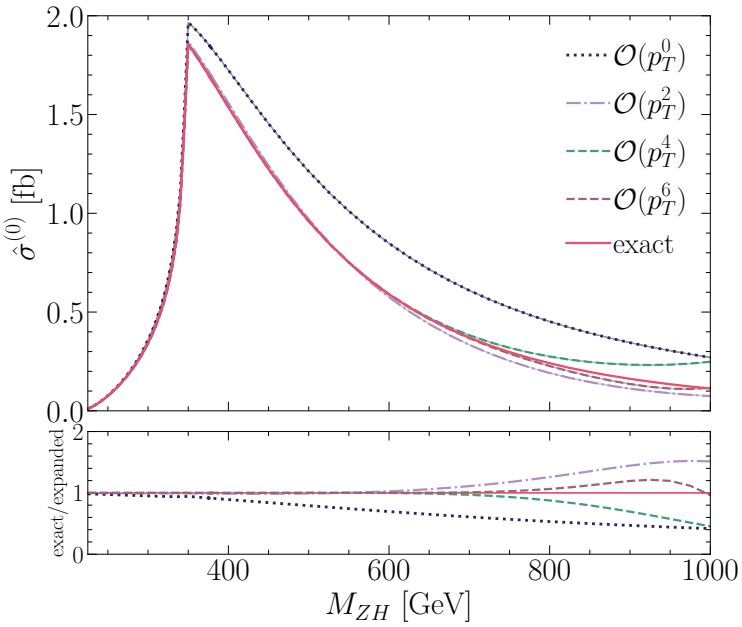

Figure 6.3. The Born partonic cross-section as a function of the invariant mass M_{Zh}. The exact (red line) is plotted together with results at different orders in the p_T-expansion (dashed lines). In the bottom part, the ratio of the full result over the p_T-expanded one at various orders is shown. This plot has been already published in [200]

6.3.1 Renormalisation

The two-loop corrections to the triangle and box diagrams contain both UV and IR divergences. The first emerges from UV divergent sub-diagrams, such as top mass renormalisation and QCD vertex correction. While the lR divergences come from massless loops. In order to remove these divergences, one introduces adequate counter-terms. On the other hand, the double triangle is both UV and IR finite.

We start by the gluon wavefunction renormalisation of the incoming gluons (external legs) such that the amplitude is renormalised by $Z_A^{1/2}$ for each gluon.

$$Z_A = 1 + \frac{\alpha_s^0}{4\pi}\frac{2}{3\epsilon}\left(\frac{\mu_R^2}{m_t^2}\right)^{\epsilon}. \tag{6.25}$$

The on-shell scheme for the top mass renormalisation has been used, in which the bare mass is replaced by the renormalised one $m_0 = Z_m m$ in the propagators this gives the

M_{Zh} [GeV]	$\mathcal{O}(p_T^0)$	$\mathcal{O}(p_T^2)$	$\mathcal{O}(p_T^4)$	$\mathcal{O}(p_T^6)$	full
300	0.3547	0.3393	0.3373	0.3371	0.3371
350	1.9385	1.8413	1.8292	1.8279	1.8278
400	1.6990	1.5347	1.5161	1.5143	1.5142
600	0.8328	0.5653	0.5804	0.5792	0.5794
750	0.5129	0.2482	0.3129	0.2841	0.2919

Table 6.1. The partonic cross section $\hat{\sigma}^{(0)}$ at various orders in p_T and the full computation for several values of M_{Zh}, This table has been already published in [200].

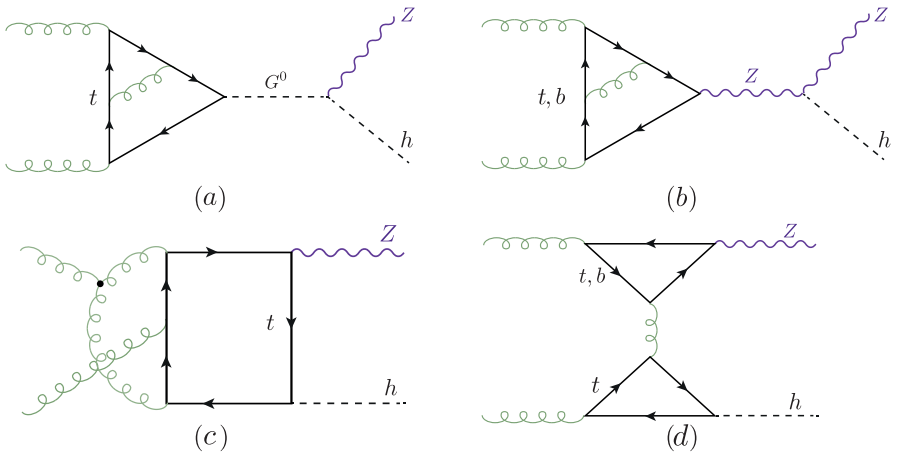

Figure 6.4. Feynman diagrams types for the virtual NLO corrections to the $gg \to Zh$ process.

$\overline{\text{MS}}$ renormalised mass.

$$Z_m = 1 + C_F \frac{3}{\epsilon}. \tag{6.26}$$

In order to convert the mass definition to the on-shell scheme we add the finite renormalisation term

$$Z_m^{OS} = 1 - 2C_F, \tag{6.27}$$

here $C_F = (N_c^2 - 1)/2N_c$ is one of the two Casimir invariants of QCD along with $C_A = N_c$. The $q\bar{q}g$ vertex correction involves a renormalisation of the strong couplings constant α_s which is done via replacing the bare constant α_s^0 with the renormalised one, hence it becomes $\alpha_s^0 = \frac{\mu_R^{2\epsilon}}{S_\epsilon} Z_{\alpha_s} \alpha_s$, where

$$Z_{\alpha_s} = 1 - \frac{\alpha_s}{4\pi} \frac{1}{\epsilon} \left(\beta_0 - \frac{2}{3}\right) \left(\frac{\mu_R^2}{m_t^2}\right)^\epsilon, \tag{6.28}$$

and the constant $\beta_0 = \frac{11}{3} C_A - \frac{2}{3} N_f$, where N_f is the number of "active" flavours. The 5-flavour scheme $N_f = 5$ is adopted here.

The loop integrals were evaluated via dimensional regularisation in $d = 4 - 2\epsilon$ dimensions. Which requires some caution when γ_5 is present in the amplitude. We let γ_5 naively anti-commute with all d-dimensional γ_μ's and then correct that with the finite renormalisation constant known as **Larin counter-term** [204]

$$Z_5 = 1 - 2\, C_F. \tag{6.29}$$

The renormalised amplitude is written as

$$\mathcal{M}(\alpha_s, m, \mu_R) = Z_A \mathcal{M}(\alpha_s^0, m^0). \tag{6.30}$$

Putting all the above substitutions together, we get the renormalised two-loop form-factor:

$$(\mathcal{A}^{(1)})^R = \mathcal{A}^{(1)} - \mathcal{A}^{(0)}_{UV} - \mathcal{A}^{(0)}_{UV,m} + \mathcal{A}^{(0)}_{\text{Larin}} \tag{6.31}$$

$$\begin{aligned} \mathcal{A}^{(0)}_{UV} &= \frac{\alpha_s}{4\pi} \frac{\beta_0}{\epsilon} \left(\frac{\mu_R^2}{\hat{s}}\right)^{-\epsilon} \mathcal{A}^{(0)}. \\ \mathcal{A}^{(0)}_{UV,m} &= \frac{\alpha_s}{4\pi} \left(\frac{3}{\epsilon} - 2\right) C_F \left(\frac{\mu_R^2}{\hat{s}}\right)^{-\epsilon} m^0 \partial_m \mathcal{A}^{(0)}. \end{aligned} \tag{6.32}$$

$$\mathcal{A}^{(0)}_{\text{Larin}} = -\frac{\alpha_s}{4\pi} C_F \mathcal{A}^{(0)}.$$

The following IR-counter-term is used in order to cancel the IR divergences.

$$\mathcal{A}_{IR}^{(0)} = \frac{e^{\gamma_E \epsilon}}{\Gamma(1-\epsilon)} \frac{\alpha_s}{4\pi} \left(\frac{\beta_0}{\epsilon} + \frac{C_A}{\epsilon^2} \right) \left(\frac{\mu_R^2}{\hat{s}} \right)^{2\epsilon} \mathcal{A}^{(0)} \tag{6.33}$$

The one-loop form-factors, need to be expanded up to order $\mathcal{O}(\epsilon^2)$, for the UV and IR counter-terms.

6.3.2 Calculation of the exact virtual corrections

The two-loop calculations of the triangle digrams involves the diagrams of with virtual Z^* and G^0, depending on the gauge of choice. Observations found in ref.[192] shows that due to Landau-Yang theorem in the Landau gauge the diagrams with the Z^* exchange vanishes. Therefore, the part of the top triangle diagrams can be obtained from the decay amplitude of a pseudoscalar boson into two gluons which is known in the literature in the full mass dependence up to NLO terms [205, 206]. On the contrary, in the unitary gauge, the NLO calculation needs to be done with the Z^* exchange diagrams only. The calculations result in apparently different Lorentz structures, that are linked via the Schouten identity

$$q^\alpha \epsilon^{\beta\gamma\delta\phi} + q^\beta \epsilon^{\gamma\delta\phi\alpha} + q^\gamma \epsilon^{\delta\phi\alpha\beta} + q^\gamma \epsilon^{\delta\phi\alpha\beta} + q^\delta \epsilon^{\phi\alpha\beta\gamma} + q^\phi \epsilon^{\alpha\beta\gamma\delta} = 0 \tag{6.34}$$

A cross-check has been preformed in order to ensure that the NLO calculation introduces no new Lorentz structures, and gives the same result in a general R_ξ gauge as the results in [205, 206]. The two-loop calculation has been carried out in R_ξ gauge. The amplitudes have been automatically generated by `FeynArts` [144] and contracted with the projectors as defined in **??** using `FeynCalc` [207, 208] and `Package X` [209] and in-house Mathematica routines. The two-loop integrals were reduced to a set of master integrals MI, illustrated graphically in Figure 6.5 using `Kira` [210]. These MI's are either products of one-loop functions (a)-(c), (e),(f),(h) and (l) or can be found in the literature [206, 211]. Their implementation in our calculation has been validated numerically using `SecDec` [212, 213]. The virtual correction for the triangle diagrams can be separated according to their colour factors into

$$\mathcal{A}^{(1)} = C_F \mathcal{A}_{CF}^{(1)} + C_A \mathcal{A}_{CA}^{(1)}, \tag{6.35}$$

The C_A part contains a double pole $\mathcal{O}(1/\epsilon^2)$ and a single pole $\mathcal{O}(1/\epsilon)$, both coming from the IR divergence. Whilst the C_F part contains a UV divergent pole that needs to be cured via mass renormalisation. The poles do not have a dependence on the renormalisation scale μ_R. However, there is a dependence on that scale in the finite part, as well. No new Lorentz structures appeared, and the final result in R_ξ matched the one found in [205, 206] for the Landau gauge. The explicit results are shown in **??**

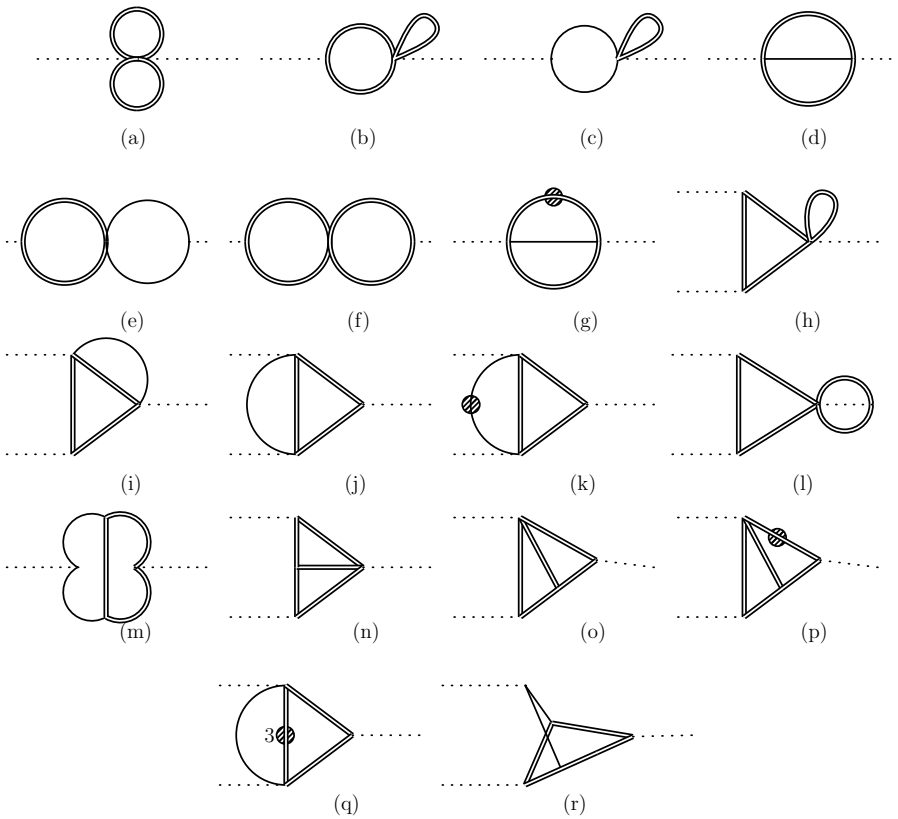

Figure 6.5. The list of two-loop master integrals (MI's) resulting from the reduction of the two-loop triangle corrections, and the product of one-loop MI's appearing in this list also appear in the calculation of the double-triangle diagrams. A single line denotes a massless propagator, while a double line denotes a massive one. The dot denotes a squared propagator, unless the number of the exponent is indicated, here only 3 appears in diagram (q).

The calculation of the double triangle diagrams (d) of Figure 6.4 is fairly straightforward, all of the integrals can be rewritten in terms of products of one-loop functions. All of the Lorentz structures appear in the double triangle except for $\mathcal{P}_6$, analogous to the triangle case. The explicit forms of form-factors corresponding to these structures are presented in **??**. Although we write the amplitude using a different tensorial structure with respect to ref.[197] we have checked, using the relations between the two tensorial structures reported in **??**, that our result is in agreement with the one presented in ref.[194].

6.3.3 Calculation of the p_T-expanded virtual corrections

The two-loop triangle diagrams can also be interpreted as an expansion in p_T, but this expansion terminates at $\mathcal{O}(p_T^2)$, rather being an infinite series. Hence, in this section we concentrate on the two-loop box diagrams p_T-expansion [1].
Similar to the two-loop triangle diagrams, the box diagrams amplitudes were generated projected through the same pipeline. After the contraction of the epsilon tensors the diagrams were expanded as described in subsection 6.1.1, keeping only $\mathcal{O}(p_T^4)$ terms. They were reduced to MI's using `FIRE` [214] and `LiteRed` [215]. The resulting MI's were identical to the one for Higgs pair production [199]. Nearly all of them are expressed in terms of generalised harmonic polylogarithms with the exception of two elliptic integrals [216, 217]. The renormalisation and IR pole subtraction procedure was carried out like prescribed subsection 6.3.1.
As a control, the two-loop box diagrams were also computed in the LME up to $\mathcal{O}(1/m_t^6)$. Since this expansion should be included within the p_T-expansion. We have retained the LME analytic expression by further expanding the p_T-expanded amplitude in small $\hat{s}/m_t^2$. Providing an additional cross-check for the validity of the p_T-expansion.

6.4 Results and conclusions

The virtual corrections to the gluon fusion Zh production have been implemented in a `FORTRAN` code using `handyG` [218], for the evaluation of generalised harmonic polylogarithms, `Chaplin` [219] for the harmonic polylogarithms appearing in the triangle two-loop functions while the elliptic integrals are evaluated using the routines of ref.[217]. Since the result is analytic, the code is significantly faster than the numerical evaluation of the two-loop amplitude [198], with evalution time of ca. 0.5 min per one phase space point on a personal laptop.
In order to facilitate the comparison of our results with the ones presented in the liter-

[1] The calculation of the box diagrams has been done mainly by my collaborators, the co-authors of [200]

$\hat{s}/m_t^2$	$\hat{t}/m_t^2$	ref.[198]	$\mathcal{O}(p_T^6)$
1.707133657190554	-0.441203767016323	35.429092(6)	35.430479
3.876056604162662	-1.616287256345735	4339.045(1)	4340.754
4.130574250302561	-1.750372271104745	6912.361(3)	6915.797
4.130574250302561	-2.595461551488002	6981.09(2)	6984.20

Table 6.2. Comparison of $\mathcal{V}_{fin}4/(\alpha_s^2\alpha^2)$ with the numerical results of ref.[198]. This plot has been already published in [200].

ature, we define the finite part of the virtual corrections as in ref.[197][2]

$$\mathcal{V}_{fin} = \frac{G_F^2 m_Z^2}{16}\left(\frac{\alpha_s}{\pi}\right)^2\left[\sum_i \left|\mathcal{A}_i^{(0)}\right|^2 \frac{C_A}{2}\left(\pi^2 - \log^2\left(\frac{\mu_R^2}{\hat{s}}\right)\right)\right. \\ \left. +2\sum_i \mathrm{Re}\left[\mathcal{A}_i^{(0)}\left(\mathcal{A}_i^{(1)}\right)^*\right]\right] \tag{6.36}$$

and in the numerical evaluation of eq.(6.36) we fixed $\mu_R = \sqrt{\hat{s}}$. Triangle and LME box toopologies were validated against the results of refs.[194, 197] finding perfect agreement at the form-factor level, i,.e.$\mathcal{A}_i^{(1)}$.

The virtual part of the partonic cross-section from the finite part of the virtual corrections in eq.(6.36) is defined by

$$\Delta\hat{\sigma}_{virt} = \int_{\hat{t}^-}^{\hat{t}^+} d\hat{t}\frac{\alpha_s}{16\pi^2}\frac{1}{\hat{s}^2}\mathcal{V}_{fin} \tag{6.37}$$

This function is used to confront p_T-expanded results. Starting with low M_{Zh} we have compared the p_T-expanded with the LME $\mathcal{V}_{fin}$, finding a good numerical agreement. It is important to note that, at the same order in the expansion, the p_T-expanded terms are more accurate than the LME ones, although computationally more demanding. Additional checks have been done using the numerical evaluation of the NLO amplitude by [198], where they have evaluated the exact two-loop MI's using `pySecDec` [220, 221]. Table 6.2 shows a comparison between our p_T-expanded $\mathcal{V}_{fin}4/(\frac{\alpha_s^0}{4\pi}^2\alpha^2)$ versus the exact numerical result of [198] for several phase space points. As can be seen from the table the relative difference between the two results is less than half a permille.

In Figure 6.6, the dashed lines show the different orders of the expansion. For all parts of the matrix elements the best results available, i.e. both $\mathcal{A}^{(0)}$ were used and the double-triangle contribution are evaluated exactly, while for $\mathcal{A}^{(1)}$ we use the various orders in the p_T-expansion. For comparison, the results are shown were $\mathcal{A}^{(1)}$ is replaced

[2] The definition of the matrix elements here differs by a factor of $\frac{1}{\hat{s}}$ from ref.[197], *cf.* also **??**.

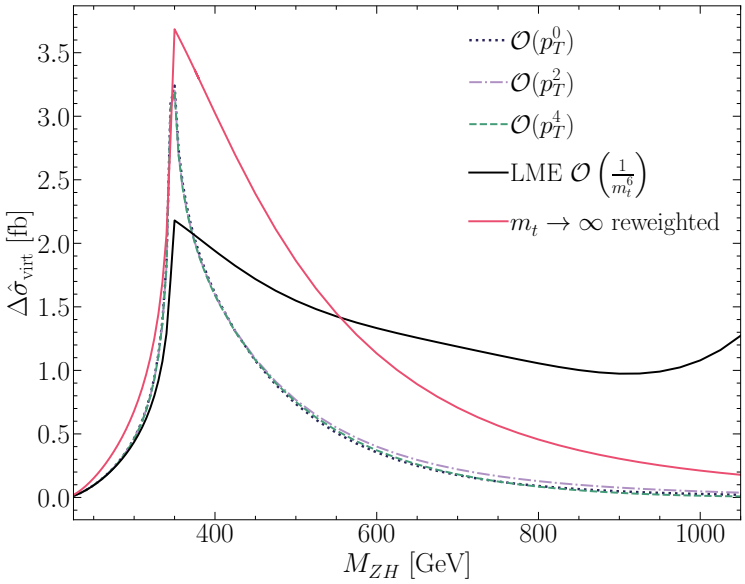

Figure 6.6. $\Delta\hat{\sigma}_{virt}$ defined by eq.(6.37), shown as a function of M_{ZH}. The various orders of the p_T-expansion are plotted as dashed lines, while the black and red continuous lines stand for the LME and reweighted $m_t \to \infty$ results, respectively.This plot has been already published in [200].

by the one computed in LME up to $\mathcal{O}(1/m_t^6)$ (full black line), which as mentioned before is valid up to $M_{ZhH} < 2m_t$. We observe that within the validity of the LME our results agree well with it. Furthermore, the results in the infinite top mass limit reweighted by the full amplitudes squared can be seen as the full red line in the plot, corresponding to the approach of ref.[192], keeping though the double triangle contribution in full top mass dependence. Differently from the LME line, the $m_t \to \infty$ reweighted one shows a behaviour, for $M_{Zh} \gtrsim 400\,\text{GeV}$, similar to the behaviour of the p_T lines. Still, the difference between the reweighted result and the p_T-expanded ones is significant. The p_T-expanded results show very good convergence. The zero order in our expansion agrees extremely well with the higher orders in the expansion, and all the three results are very close up to $M_{Zh} \sim 500\,\text{GeV}$.

The calculation of the virtual two-loop corrections to the $gg \to Zh$ is done using exact results for the triangle and double-triangle topologies, and in the p_T-expansion for the box one. The result of the calculation showed that we get the exact same MI's that was found for Higgs pair production [199] , mostly these MI's are expressed in terms of generalised harmonic polylogarithms with the exception of two elliptic integrals. Using the LO calculation, we have shown the validity of the p_T-expansion covering the invariant mass interval $M_{Zh} \lesssim 750$ GeV which covers $\sim 98\%$ of the total phase space for $13 - 14$

TeV energies.
The p_T-expansion agrees with per mill level with the numerical results found in [198]. However, it allows for fast computation of the amplitude with circa one second per phase space point using a modern laptop with mid-range specifications. Additionally. the integration over the $\hat{t}$ variable in eq.(6.37) converges very well. The flexibility of our analytic results, an application to beyond-the-Standard Model is certainly possible.
Finally, it should be noted that this calculation complements nicely the results obtained in ref.[197] using a high-energy expansion, that according to the authors provides precise results for $p_T \gtrsim 200\,\text{GeV}$. The merging of the two analyses is going to provide a result that covers the whole phase space, can be easily implemented into a Monte Carlo code using Padé approximants, which is currently a work in progress in Cite the new paper here-later

Bibliography

[1] R. A. Minlos, *Introduction to mathematical statistical physics*. No. 19. American Mathematical Soc., 2000.

[2] M. Gell-Mann, "The eightfold way: A theory of strong interaction symmetry,". https://www.osti.gov/biblio/4008239.

[3] C. N. Yang and R. L. Mills, "Conservation of isotopic spin and isotopic gauge invariance," *Phys. Rev.* **96** (Oct, 1954) 191–195. https://link.aps.org/doi/10.1103/PhysRev.96.191.

[4] **Particle Data Group** Collaboration, P. Zyla *et al.*, "Review of Particle Physics," *PTEP* **2020** no. 8, (2020) 083C01.

[5] D. S. Freed, "Lectures on topological quantum field theory," 1993.

[6] R. Dijkgraaf and E. Witten, "Topological gauge theories and group cohomology," *Communications in Mathematical Physics* **129** no. 2, (1990) 393–429.

[7] A. Salam and J. C. Ward, "On a gauge theory of elementary interactions," *Il Nuovo Cimento (1955-1965)* **19** no. 1, (1961) 165–170. https://doi.org/10.1007/BF02812723.

[8] A. Salam and J. C. Ward, "Weak and electromagnetic interactions," *Il Nuovo Cimento (1955-1965)* **11** no. 4, (1959) 568–577. https://doi.org/10.1007/BF02726525.

[9] S. Weinberg, "A model of leptons," *Phys. Rev. Lett.* **19** (Nov, 1967) 1264–1266. https://link.aps.org/doi/10.1103/PhysRevLett.19.1264.

[10] F. Capozzi, E. Lisi, A. Marrone, D. Montanino, and A. Palazzo, "Neutrino masses and mixings: Status of known and unknown 3ν parameters," *Nucl. Phys. B* **908** (2016) 218–234, arXiv:1601.07777 [hep-ph].

[11] **ALEPH, DELPHI, L3, OPAL, SLD, LEP Electroweak Working Group, SLD Electroweak Group, SLD Heavy Flavour Group** Collaboration, S. Schael *et al.*, "Precision electroweak measurements on the Z resonance," *Phys. Rept.* **427** (2006) 257–454, arXiv:hep-ex/0509008 [hep-ex].

[12] **SLD** Collaboration, K. Abe *et al.*, "First direct measurement of the parity violating coupling of the Z0 to the s quark," *Phys. Rev. Lett.* **85** (2000) 5059–5063, arXiv:hep-ex/0006019.

[13] **CDF, D0** Collaboration, T. E. W. Group, "2012 Update of the Combination of CDF and D0 Results for the Mass of the W Boson," arXiv:1204.0042 [hep-ex].

[14] **ALEPH, DELPHI, L3, OPAL, LEP Electroweak** Collaboration, S. Schael *et al.*, "Electroweak Measurements in Electron-Positron Collisions at W-Boson-Pair Energies at LEP," *Phys. Rept.* **532** (2013) 119–244, arXiv:1302.3415 [hep-ex].

[15] **DØ** Collaboration, V. M. Abazov *et al.*, "Measurement of $\sin^2\theta^{\ell}_{\text{eff}}$ and Z-light quark couplings using the forward-backward charge asymmetry in $p\overline{p} \to Z/\gamma^* \to e^+e^-$ events with $\mathcal{L} = 5.0$ fb^{-1} at $\sqrt{s} = 1.96$ TeV," *Phys. Rev. D* **84** (2011) 012007, arXiv:1104.4590 [hep-ex].

[16] **CMS** Collaboration, V. Khachatryan *et al.*, "Measurement of the t-channel single-top-quark production cross section and of the $| V_{tb} |$ CKM matrix element in pp collisions at $\sqrt{s}$= 8 TeV," *JHEP* **06** (2014) 090, arXiv:1403.7366 [hep-ex].

[17] **ATLAS** Collaboration, M. Aaboud *et al.*, "Measurement of the W-boson mass in pp collisions at $\sqrt{s} = 7$ TeV with the ATLAS detector," *Eur. Phys. J. C* **78** no. 2, (2018) 110, arXiv:1701.07240 [hep-ex]. [Erratum: Eur.Phys.J.C 78, 898 (2018)].

[18] Y. Nambu, "Quasi-particles and gauge invariance in the theory of superconductivity," *Phys. Rev.* **117** (Feb, 1960) 648–663. https://link.aps.org/doi/10.1103/PhysRev.117.648.

[19] J. Goldstone, "Field theories with superconductor solutions," *Il Nuovo Cimento (1955-1965)* **19** no. 1, (1961) 154–164.

[20] J. Goldstone, A. Salam, and S. Weinberg, "Broken symmetries," *Phys. Rev.* **127** (Aug, 1962) 965–970. https://link.aps.org/doi/10.1103/PhysRev.127.965.

[21] P. W. Anderson, "Plasmons, gauge invariance, and mass," *Phys. Rev.* **130** (Apr, 1963) 439–442. https://link.aps.org/doi/10.1103/PhysRev.130.439.

[22] F. Englert and R. Brout, "Broken symmetry and the mass of gauge vector mesons," *Phys. Rev. Lett.* **13** (Aug, 1964) 321–323. https://link.aps.org/doi/10.1103/PhysRevLett.13.321.

[23] P. W. Higgs, "Broken symmetries and the masses of gauge bosons," *Phys. Rev. Lett.* **13** (Oct, 1964) 508–509. https://link.aps.org/doi/10.1103/PhysRevLett.13.508.

[24] G. S. Guralnik, C. R. Hagen, and T. W. B. Kibble, "Global conservation laws and massless particles," *Phys. Rev. Lett.* **13** (Nov, 1964) 585–587. https://link.aps.org/doi/10.1103/PhysRevLett.13.585.

[25] G. S. Guralnik, "The History of the Guralnik, Hagen and Kibble development of the Theory of Spontaneous Symmetry Breaking and Gauge Particles," *Int. J. Mod. Phys. A* **24** (2009) 2601–2627, arXiv:0907.3466 [physics.hist-ph].

[26] J. Erler and M. Schott, "Electroweak Precision Tests of the Standard Model after the Discovery of the Higgs Boson," *Prog. Part. Nucl. Phys.* **106** (2019) 68–119, arXiv:1902.05142 [hep-ph].

[27] **CMS** Collaboration, S. Chatrchyan *et al.*, "Observation of a New Boson at a Mass of 125 GeV with the CMS Experiment at the LHC," *Phys. Lett. B* **716** (2012) 30–61, arXiv:1207.7235 [hep-ex].

[28] **ATLAS** Collaboration, G. Aad *et al.*, "Observation of a new particle in the search for the Standard Model Higgs boson with the ATLAS detector at the LHC," *Phys. Lett. B* **716** (2012) 1–29, arXiv:1207.7214 [hep-ex].

[29] N. Cabibbo, "Unitary symmetry and leptonic decays," *Phys. Rev. Lett.* **10** (Jun, 1963) 531–533. https://link.aps.org/doi/10.1103/PhysRevLett.10.531.

[30] M. Kobayashi and T. Maskawa, "CP-Violation in the Renormalizable Theory of Weak Interaction," *Progress of Theoretical Physics* **49** no. 2, (02, 1973) 652–657, https://academic.oup.com/ptp/article-pdf/49/2/652/5257692/49-2-652.pdf. https://doi.org/10.1143/PTP.49.652.

[31] R. E. Behrends, R. J. Finkelstein, and A. Sirlin, "Radiative corrections to decay processes," *Phys. Rev.* **101** (Jan, 1956) 866–873. https://link.aps.org/doi/10.1103/PhysRev.101.866.

[32] T. Kinoshita and A. Sirlin, "Radiative corrections to fermi interactions," *Phys. Rev.* **113** (Mar, 1959) 1652–1660. https://link.aps.org/doi/10.1103/PhysRev.113.1652.

[33] I. Mohammad and A. Donnachie, "Radiative Corrections to Radiative Muon Decay,".

[34] T. van Ritbergen and R. G. Stuart, "Complete 2-loop quantum electrodynamic contributions to the muon lifetime in the fermi model," *Phys. Rev. Lett.* **82** (Jan, 1999) 488–491. https://link.aps.org/doi/10.1103/PhysRevLett.82.488.

[35] D. Ross and M. Veltman, "Neutral currents and the higgs mechanism," *Nuclear Physics B* **95** no. 1, (1975) 135–147. https://www.sciencedirect.com/science/article/pii/055032137590485X.

[36] A. Djouadi, "The Anatomy of electro-weak symmetry breaking. I: The Higgs boson in the standard model," *Phys. Rept.* **457** (2008) 1–216, arXiv:hep-ph/0503172.

[37] M. J. Dugan, H. Georgi, and D. B. Kaplan, "Anatomy of a composite higgs model," *Nuclear Physics* **254** (1985) 299–326.

[38] C. T. Hill and E. H. Simmons, "Strong Dynamics and Electroweak Symmetry Breaking," *Phys. Rept.* **381** (2003) 235–402, arXiv:hep-ph/0203079. [Erratum: Phys.Rept. 390, 553–554 (2004)].

[39] M. Schwartz, *Quantum Field Theory and the Standard Model*. Quantum Field Theory and the Standard Model. Cambridge University Press, 2014. https://books.google.nl/books?id=HbdEAgAAQBAJ.

[40] M. Peskin and D. Schroeder, *An Introduction To Quantum Field Theory*. Frontiers in Physics. Avalon Publishing, 1995. https://books.google.de/books?id=EVeNNcslvX0C.

[41] M. Einhorn, D. Jones, and M. Veltman, "Heavy particles and the rho parameter in the standard model," *Nuclear Physics B* **191** no. 1, (1981) 146–172. https://www.sciencedirect.com/science/article/pii/0550321381902923.

[42] M. E. Peskin and T. Takeuchi, "New constraint on a strongly interacting higgs sector," *Phys. Rev. Lett.* **65** (Aug, 1990) 964–967. https://link.aps.org/doi/10.1103/PhysRevLett.65.964.

[43] M. E. Peskin and T. Takeuchi, "Estimation of oblique electroweak corrections," 1991.

[44] M. Golden and L. Randall, "Radiative corrections to electroweak parameters in technicolor theories," *Nuclear Physics B* **361** no. 1, (1991) 3–23. https://www.sciencedirect.com/science/article/pii/0550321391906144.

[45] B. Holdom and J. Terning, "Large corrections to electroweak parameters in technicolor theories," *Physics Letters B* **247** no. 1, (1990) 88–92. https://www.sciencedirect.com/science/article/pii/037026939091054F.

[46] G. Altarelli, R. Barbieri, and S. Jadach, "Toward a model-independent analysis of electroweak data," *Nuclear Physics B* **369** no. 1, (1992) 3–32. https://www.sciencedirect.com/science/article/pii/055032139290376M.

[47] R. S. Chivukula, S. B. Selipsky, and E. H. Simmons, "Nonoblique effects in the zbb^{-} vertex from extended technicolor dynamics," *Phys. Rev. Lett.* **69** (Jul, 1992) 575–577. https://link.aps.org/doi/10.1103/PhysRevLett.69.575.

[48] E. H. Simmons, R. S. Chivukula, and J. Terning, "Testing extended technicolor with R(b)," *Prog. Theor. Phys. Suppl.* **123** (1996) 87–96, arXiv:hep-ph/9509392.

[49] G. Valencia and S. Willenbrock, "Goldstone-boson equivalence theorem and the higgs resonance," *Phys. Rev. D* **42** (Aug, 1990) 853–859. https://link.aps.org/doi/10.1103/PhysRevD.42.853.

[50] L. Di Luzio, R. Gröber, and M. Spannowsky, "Maxi-sizing the trilinear Higgs self-coupling: how large could it be?," *Eur. Phys. J. C* **77** no. 11, (2017) 788, arXiv:1704.02311 [hep-ph].

[51] M. Lindner, "Implications of Triviality for the Standard Model," *Z. Phys. C* **31** (1986) 295.

[52] M. Sher, "Electroweak Higgs Potentials and Vacuum Stability," *Phys. Rept.* **179** (1989) 273–418.

[53] J. A. Casas, J. R. Espinosa, and M. Quiros, "Standard model stability bounds for new physics within LHC reach," *Phys. Lett. B* **382** (1996) 374–382, arXiv:hep-ph/9603227.

[54] G. Isidori, G. Ridolfi, and A. Strumia, "On the metastability of the standard model vacuum," *Nucl. Phys. B* **609** (2001) 387–409, arXiv:hep-ph/0104016.

[55] G. Degrassi, S. Di Vita, J. Elias-Miro, J. R. Espinosa, G. F. Giudice, G. Isidori, and A. Strumia, "Higgs mass and vacuum stability in the Standard Model at NNLO," *JHEP* **08** (2012) 098, arXiv:1205.6497 [hep-ph].

[56] J. Ellis, "Physics goals of the next century@ cern," in *AIP Conference Proceedings*, vol. 542, pp. 267–292, American Institute of Physics. 2000.

[57] "LHC-facts." http://www.lhc-facts.ch.

[58] "Weltmaschine- CERN und LHC." https://www.weltmaschine.de/cern_und_lhc/lhc/.

[59] "LHC Design Report Vol.1: The LHC Main Ring,".

[60] "LHC lomg term schedule ." https://lhc-commissioning.web.cern.ch/schedule/LHC-long-term.htm.

[61] "High-Luminosity Large Hadron Collider (HL-LHC) : Preliminary Design Report,".

[62] "LHC preformance tracking." https://bpt.web.cern.ch/lhc/.

[63] "Taking a look at the LHC." https://www.lhc-closer.de/taking_a_closer_look_at_lhc/0.luminosity.

[64] "ATLAS Run 2 luminosity public results ." https://twiki.cern.ch/twiki/bin/view/AtlasPublic/LuminosityPublicResults.

[65] "CMS luminosity public results ." https://twiki.cern.ch/twiki/bin/view/CMSPublic/LumiPublicResults.

[66] "ATLAS Run 2 luminosity public results ." https://twiki.cern.ch/twiki/bin/view/AtlasPublic/LuminosityPublicResultsRun2.

[67] S. Fartoukh *et al.*, "LHC Configuration and Operational Scenario for Run 3," tech. rep., CERN, Geneva, Nov, 2021. https://cds.cern.ch/record/2790409.

[68] **CMS** Collaboration, A. M. Sirunyan *et al.*, "A measurement of the Higgs boson mass in the diphoton decay channel," *Phys. Lett. B* **805** (2020) 135425, arXiv:2002.06398 [hep-ex].

[69] **ATLAS** Collaboration, M. Aaboud *et al.*, "Measurement of the Higgs boson mass in the $H \to ZZ^* \to 4\ell$ and $H \to \gamma\gamma$ channels with $\sqrt{s} = 13$ TeV pp collisions using the ATLAS detector," *Phys. Lett. B* **784** (2018) 345–366, arXiv:1806.00242 [hep-ex].

[70] **ATLAS, CMS** Collaboration, G. Aad *et al.*, "Combined Measurement of the Higgs Boson Mass in pp Collisions at $\sqrt{s} = 7$ and 8 TeV with the ATLAS and CMS Experiments," *Phys. Rev. Lett.* **114** (2015) 191803, arXiv:1503.07589 [hep-ex].

[71] **CMS** Collaboration, A. M. Sirunyan *et al.*, "Measurements of properties of the Higgs boson decaying into the four-lepton final state in pp collisions at $\sqrt{s} = 13$ TeV," *JHEP* **11** (2017) 047, arXiv:1706.09936 [hep-ex].

[72] P. M. Aronow and B. T. Miller, *Foundations of Agnostic Statistics*. Cambridge University Press, 2019.

[73] J. De Blas, G. Durieux, C. Grojean, J. Gu, and A. Paul, "On the future of Higgs, electroweak and diboson measurements at lepton colliders," *JHEP* **12** (2019) 117, arXiv:1907.04311 [hep-ph].

[74] S. Banerjee, R. S. Gupta, O. Ochoa-Valeriano, and M. Spannowsky, "High energy lepton colliders as the ultimate Higgs microscopes," arXiv:2109.14634 [hep-ph].

[75] **ATLAS** Collaboration, M. Aaboud *et al.*, "Constraints on off-shell Higgs boson production and the Higgs boson total width in $ZZ \to 4\ell$ and $ZZ \to 2\ell 2\nu$ final states with the ATLAS detector," *Phys. Lett. B* **786** (2018) 223–244, arXiv:1808.01191 [hep-ex].

[76] **CMS** Collaboration, A. M. Sirunyan *et al.*, "Measurements of the Higgs boson width and anomalous HVV couplings from on-shell and off-shell production in the four-lepton final state," *Phys. Rev. D* **99** no. 11, (2019) 112003, arXiv:1901.00174 [hep-ex].

[77] **ATLAS** Collaboration, G. Aad *et al.*, "Study of the spin and parity of the Higgs boson in diboson decays with the ATLAS detector," *Eur. Phys. J. C* **75** no. 10, (2015) 476, arXiv:1506.05669 [hep-ex]. [Erratum: Eur.Phys.J.C 76, 152 (2016)].

[78] **CMS** Collaboration, V. Khachatryan *et al.*, "Constraints on the spin-parity and anomalous HVV couplings of the Higgs boson in proton collisions at 7 and 8 TeV," *Phys. Rev. D* **92** no. 1, (2015) 012004, arXiv:1411.3441 [hep-ex].

[79] **CMS** Collaboration, V. Khachatryan *et al.*, "Measurement of differential and integrated fiducial cross sections for Higgs boson production in the four-lepton decay channel in pp collisions at $\sqrt{s} = 7$ and 8 TeV," *JHEP* **04** (2016) 005, arXiv:1512.08377 [hep-ex].

[80] "Measurements of the total cross sections for Higgs boson production combining the $H \to \gamma\gamma$ and $H \to ZZ^* \to 4\ell$ decay channels at 7, 8 and 13 TeV center-of-mass energies with the ATLAS detector,".

[81] **CMS** Collaboration, A. M. Sirunyan *et al.*, "Measurement and interpretation of differential cross sections for Higgs boson production at $\sqrt{s} = 13$ TeV," *Phys. Lett. B* **792** (2019) 369–396, arXiv:1812.06504 [hep-ex].

[82] **CMS** Collaboration, A. M. Sirunyan *et al.*, "Measurements of production cross sections of the Higgs boson in the four-lepton final state in proton–proton collisions at $\sqrt{s} = 13\,\text{TeV}$," *Eur. Phys. J. C* **81** no. 6, (2021) 488, arXiv:2103.04956 [hep-ex].

[83] **ATLAS** Collaboration, "Combined measurement of the total and differential cross sections in the $H \to \gamma\gamma$ and the $H \to ZZ^* \to 4\ell$ decay channels at $\sqrt{s}$ =13 TeV with the ATLAS detector,".

[84] **ATLAS** Collaboration, "Measurements and interpretations of Higgs-boson fiducial cross sections in the diphoton decay channel using 139 fb^{-}1 of pp collision data at $\sqrt{s} = 13$ TeV with the ATLAS detector,".

[85] **CMS** Collaboration, "Measurements of properties of the Higgs boson in the four-lepton final state in proton-proton collisions at $\sqrt{s} = 13$ TeV,".

[86] N. Berger *et al.*, "Simplified Template Cross Sections - Stage 1.1," arXiv:1906.02754 [hep-ph].

[87] **ATLAS** Collaboration, "A combination of measurements of Higgs boson production and decay using up to 139 fb^{-1} of proton–proton collision data at $\sqrt{s} = 13$ TeV collected with the ATLAS experiment," Tech. Rep. ATLAS-CONF-2020-027, 2020.

[88] **CMS** Collaboration, A. M. Sirunyan *et al.*, "Measurements of Higgs boson production cross sections and couplings in the diphoton decay channel at $\sqrt{\mathrm{s}} =$ 13 TeV," *JHEP* **07** (2021) 027, arXiv:2103.06956 [hep-ex].

[89] **CMS Collaboration** Collaboration, "Sensitivity projections for Higgs boson properties measurements at the HL-LHC," tech. rep., CERN, Geneva, 2018. https://cds.cern.ch/record/2647699.

[90] **CMS** Collaboration, "Combined Higgs boson production and decay measurements with up to 137 fb-1 of proton-proton collision data at sqrts = 13 TeV," Tech. Rep. CMS-PAS-HIG-19-005, 2020.

[91] **CMS** Collaboration, "Measurement of Higgs boson production in association with a W or Z boson in the H $\rightarrow$ WW decay channel," Tech. Rep. CMS-PAS-HIG-19-017, 2021.

[92] **ATLAS** Collaboration, "Combined measurements of Higgs boson production and decay using up to 139 fb^{-1} of proton-proton collision data at $\sqrt{s} = 13$ TeV collected with the ATLAS experiment,".

[93]

[94] **CMS** Collaboration, A. M. Sirunyan *et al.*, "Search for associated production of a Higgs boson and a single top quark in proton-proton collisions at $\sqrt{s} = 13$ TeV," *Phys. Rev. D* **99** no. 9, (2019) 092005, arXiv:1811.09696 [hep-ex].

[95] **CMS** Collaboration, A. M. Sirunyan *et al.*, "Observation of Higgs boson decay to bottom quarks," *Phys. Rev. Lett.* **121** no. 12, (2018) 121801, arXiv:1808.08242 [hep-ex].

[96] **ATLAS** Collaboration, M. Aaboud *et al.*, "Observation of $H \to b\bar{b}$ decays and VH production with the ATLAS detector," *Phys. Lett. B* **786** (2018) 59–86, arXiv:1808.08238 [hep-ex].

[97] **ATLAS** Collaboration, M. Aaboud *et al.*, "Measurement of VH, H $\to$ b$\bar{\text{b}}$ production as a function of the vector-boson transverse momentum in 13 TeV pp collisions with the ATLAS detector," *JHEP* **05** (2019) 141, arXiv:1903.04618 [hep-ex].

[98] **ATLAS** Collaboration, M. Aaboud *et al.*, "Cross-section measurements of the Higgs boson decaying into a pair of τ-leptons in proton-proton collisions at $\sqrt{s} = 13$ TeV with the ATLAS detector," *Phys. Rev. D* **99** (2019) 072001, arXiv:1811.08856 [hep-ex].

[99] **CMS** Collaboration, "Measurement of Higgs boson production and decay to the $\tau\tau$ final state,".

[100] **ATLAS** Collaboration, G. Aad *et al.*, "A search for the dimuon decay of the Standard Model Higgs boson with the ATLAS detector," *Phys. Lett. B* **812** (2021) 135980, arXiv:2007.07830 [hep-ex].

[101] **CMS** Collaboration, A. M. Sirunyan *et al.*, "Evidence for Higgs boson decay to a pair of muons," *JHEP* **01** (2021) 148, arXiv:2009.04363 [hep-ex].

[102] **ATLAS** Collaboration, "Direct constraint on the Higgs-charm coupling from a search for Higgs boson decays to charm quarks with the ATLAS detector,".

[103] **CMS** Collaboration, A. M. Sirunyan *et al.*, "A search for the standard model Higgs boson decaying to charm quarks," *JHEP* **03** (2020) 131, arXiv:1912.01662 [hep-ex].

[104] **ATLAS Collaboration** Collaboration, C. Bernius, "HL-LHC prospects from ATLAS and CMS," tech. rep., CERN, Geneva, Mar, 2019. https://cds.cern.ch/record/2666331.

[105] **ATLAS** Collaboration, "Prospects for $H \to c\bar{c}$ using Charm Tagging with the ATLAS Experiment at the HL-LHC," Tech. Rep. ATL-PHYS-PUB-2018-016, CERN, Geneva, Aug, 2018. http://cds.cern.ch/record/2633635.

[106] **ATLAS** Collaboration, G. Aad *et al.*, "A search for the $Z\gamma$ decay mode of the Higgs boson in pp collisions at $\sqrt{s} = 13$ TeV with the ATLAS detector," *Phys. Lett. B* **809** (2020) 135754, arXiv:2005.05382 [hep-ex].

[107] S. Dawson, S. Dittmaier, and M. Spira, "Neutral Higgs boson pair production at hadron colliders: QCD corrections," *Phys. Rev. D* **58** (1998) 115012, arXiv:hep-ph/9805244.

[108] A. Papaefstathiou and K. Sakurai, "Triple Higgs boson production at a 100 TeV proton-proton collider," *JHEP* **02** (2016) 006, arXiv:1508.06524 [hep-ph].

[109] M. McCullough, "An Indirect Model-Dependent Probe of the Higgs Self-Coupling," *Phys. Rev. D* **90** no. 1, (2014) 015001, arXiv:1312.3322 [hep-ph]. [Erratum: Phys.Rev.D 92, 039903 (2015)].

[110] M. Gorbahn and U. Haisch, "Indirect probes of the trilinear Higgs coupling: $gg \to h$ and $h \to \gamma\gamma$," *JHEP* **10** (2016) 094, arXiv:1607.03773 [hep-ph].

[111] G. Degrassi, P. P. Giardino, F. Maltoni, and D. Pagani, "Probing the Higgs self coupling via single Higgs production at the LHC," *JHEP* **12** (2016) 080, arXiv:1607.04251 [hep-ph].

[112] W. Bizon, M. Gorbahn, U. Haisch, and G. Zanderighi, "Constraints on the trilinear Higgs coupling from vector boson fusion and associated Higgs production at the LHC," *JHEP* **07** (2017) 083, arXiv:1610.05771 [hep-ph].

[113] F. Maltoni, D. Pagani, A. Shivaji, and X. Zhao, "Trilinear Higgs coupling determination via single-Higgs differential measurements at the LHC," *Eur. Phys. J. C* **77** no. 12, (2017) 887, arXiv:1709.08649 [hep-ph].

[114] G. Degrassi and M. Vitti, "The effect of an anomalous Higgs trilinear self-coupling on the $h \to \gamma Z$ decay," *Eur. Phys. J. C* **80** no. 4, (2020) 307, arXiv:1912.06429 [hep-ph].

[115] G. Degrassi, B. Di Micco, P. P. Giardino, and E. Rossi, "Higgs boson self-coupling constraints from single Higgs, double Higgs and Electroweak measurements," *Phys. Lett. B* **817** (2021) 136307, arXiv:2102.07651 [hep-ph].

[116] U. Haisch and G. Koole, "Off-shell Higgs production at the LHC as a probe of the trilinear Higgs coupling," arXiv:2111.12589 [hep-ph].

[117] B. Grzadkowski, M. Iskrzynski, M. Misiak, and J. Rosiek, "Dimension-Six Terms in the Standard Model Lagrangian," *JHEP* **10** (2010) 085, arXiv:1008.4884 [hep-ph].

[118] R. Grober, M. Muhlleitner, and M. Spira, "Higgs Pair Production at NLO QCD for CP-violating Higgs Sectors," *Nucl. Phys. B* **925** (2017) 1–27, arXiv:1705.05314 [hep-ph].

[119] G. F. Giudice, C. Grojean, A. Pomarol, and R. Rattazzi, "The Strongly-Interacting Light Higgs," *JHEP* **06** (2007) 045, arXiv:hep-ph/0703164.

[120] R. Contino, M. Ghezzi, C. Grojean, M. Muhlleitner, and M. Spira, "Effective Lagrangian for a light Higgs-like scalar," *JHEP* **07** (2013) 035, arXiv:1303.3876 [hep-ph].

[121] J. Elias-Miró, C. Grojean, R. S. Gupta, and D. Marzocca, "Scaling and tuning of EW and Higgs observables," *JHEP* **05** (2014) 019, arXiv:1312.2928 [hep-ph].

[122] K. Hagiwara, S. Ishihara, R. Szalapski, and D. Zeppenfeld, "Low-energy effects of new interactions in the electroweak boson sector," *Phys. Rev. D* **48** (1993) 2182–2203.

[123] C. Hartmann and M. Trott, "Higgs Decay to Two Photons at One Loop in the Standard Model Effective Field Theory," *Phys. Rev. Lett.* **115** no. 19, (2015) 191801, arXiv:1507.03568 [hep-ph].

[124] B. Bellazzini, C. Csaki, J. Hubisz, J. Serra, and J. Terning, "A Higgslike Dilaton," *Eur. Phys. J. C* **73** no. 2, (2013) 2333, arXiv:1209.3299 [hep-ph].

[125] G. Buchalla, O. Cata, A. Celis, and C. Krause, "Standard Model Extended by a Heavy Singlet: Linear vs. Nonlinear EFT," *Nucl. Phys. B* **917** (2017) 209–233, arXiv:1608.03564 [hep-ph].

[126] **ATLAS** Collaboration, G. Aad *et al.*, "Combined measurements of Higgs boson production and decay using up to 80 fb^{-1} of proton-proton collision data at $\sqrt{s} = 13$ TeV collected with the ATLAS experiment," *Phys. Rev. D* **101** no. 1, (2020) 012002, arXiv:1909.02845 [hep-ex].

[127] **CMS** Collaboration, A. M. Sirunyan *et al.*, "Combined measurements of Higgs boson couplings in proton–proton collisions at $\sqrt{s} = 13\,\text{TeV}$," *Eur. Phys. J. C* **79** no. 5, (2019) 421, arXiv:1809.10733 [hep-ex].

[128] J. F. Gunion, H. E. Haber, G. L. Kane, and S. Dawson, "The Higgs Hunter's Guide," *Front. Phys.* **80** (2000) 1–404.

[129] S. Di Vita, C. Grojean, G. Panico, M. Riembau, and T. Vantalon, "A global view on the Higgs self-coupling," *JHEP* **09** (2017) 069, arXiv:1704.01953 [hep-ph].

[130] **ATLAS** Collaboration, "Constraints on the Higgs boson self-coupling from the combination of single-Higgs and double-Higgs production analyses performed with the ATLAS experiment," Tech. Rep. ATLAS-CONF-2019-049, 2019.

[131] R. Frederix, D. Pagani, and M. Zaro, "Large NLO corrections in $t\bar{t}W^{\pm}$ and $t\bar{t}t\bar{t}$ hadroproduction from supposedly subleading EW contributions," *JHEP* **02** (2018) 031, arXiv:1711.02116 [hep-ph].

[132] **CMS** Collaboration, A. M. Sirunyan *et al.*, "Search for the production of four top quarks in the single-lepton and opposite-sign dilepton final states in proton-proton collisions at $\sqrt{s} = 13$ TeV," *JHEP* **11** (2019) 082, arXiv:1906.02805 [hep-ex].

[133] **ATLAS** Collaboration, G. Aad *et al.*, "Evidence for $t\bar{t}t\bar{t}$ production in the multilepton final state in proton–proton collisions at $\sqrt{s} = 13$ TeV with the ATLAS detector," *Eur. Phys. J. C* **80** no. 11, (2020) 1085, arXiv:2007.14858 [hep-ex].

[134] **CMS** Collaboration, A. M. Sirunyan *et al.*, "Measurement of the cross section for $\mathrm{t\bar{t}}$ production with additional jets and b jets in pp collisions at $\sqrt{s} = 13$ TeV," *JHEP* **07** (2020) 125, arXiv:2003.06467 [hep-ex].

[135] **ATLAS** Collaboration, "Measurements of fiducial and differential cross-sections of $t\bar{t}$ production with additional heavy-flavour jets in proton-proton collisions at $\sqrt{s} = 13$ TeV with the ATLAS detector," Tech. Rep. ATLAS-CONF-2018-029, 2018.

[136] J. D'Hondt, A. Mariotti, K. Mimasu, S. Moortgat, and C. Zhang, "Learning to pinpoint effective operators at the LHC: a study of the $\mathrm{t\bar{t}b\bar{b}}$ signature," *JHEP* **11** (2018) 131, arXiv:1807.02130 [hep-ph].

[137] N. P. Hartland, F. Maltoni, E. R. Nocera, J. Rojo, E. Slade, E. Vryonidou, and C. Zhang, "A Monte Carlo global analysis of the Standard Model Effective Field Theory: the top quark sector," *JHEP* **04** (2019) 100, arXiv:1901.05965 [hep-ph].

[138] C. Degrande, G. Durieux, F. Maltoni, K. Mimasu, E. Vryonidou, and C. Zhang, "Automated one-loop computations in the standard model effective field theory," *Phys. Rev. D* **103** no. 9, (2021) 096024, arXiv:2008.11743 [hep-ph].

[139] J. de Blas, M. Chala, and J. Santiago, "Renormalization Group Constraints on New Top Interactions from Electroweak Precision Data," *JHEP* **09** (2015) 189, arXiv:1507.00757 [hep-ph].

[140] **SMEFiT** Collaboration, J. J. Ethier, G. Magni, F. Maltoni, L. Mantani, E. R. Nocera, J. Rojo, E. Slade, E. Vryonidou, and C. Zhang, "Combined SMEFT interpretation of Higgs, diboson, and top quark data from the LHC," *JHEP* **11** (2021) 089, arXiv:2105.00006 [hep-ph].

[141] A. Dedes, W. Materkowska, M. Paraskevas, J. Rosiek, and K. Suxho, "Feynman rules for the Standard Model Effective Field Theory in R_ξ -gauges," *JHEP* **06** (2017) 143, arXiv:1704.03888 [hep-ph].

[142] H. Patel, "Package-X: A Mathematica package for the analytic calculation of one-loop integrals," *Comput. Phys. Commun.* **197** (2015) 276–290, arXiv:1503.01469 [hep-ph].

[143] P. Maierhöfer, J. Usovitsch, and P. Uwer, "Kira—A Feynman integral reduction program," *Comput. Phys. Commun.* **230** (2018) 99–112, arXiv:1705.05610 [hep-ph].

[144] T. Hahn, "Generating Feynman diagrams and amplitudes with FeynArts 3," *Comput. Phys. Commun.* **140** (2001) 418–431, arXiv:hep-ph/0012260.

[145] A. Alloul, N. D. Christensen, C. Degrande, C. Duhr, and B. Fuks, "FeynRules 2.0 - A complete toolbox for tree-level phenomenology," *Comput. Phys. Commun.* **185** (2014) 2250–2300, arXiv:1310.1921 [hep-ph].

[146] A. Smirnov, "Algorithm FIRE – Feynman Integral REduction," *JHEP* **10** (2008) 107, arXiv:0807.3243 [hep-ph].

[147] S. Dawson and P. P. Giardino, "Higgs decays to ZZ and $Z\gamma$ in the standard model effective field theory: An NLO analysis," *Phys. Rev. D* **97** no. 9, (2018) 093003, arXiv:1801.01136 [hep-ph].

[148] E. E. Jenkins, A. V. Manohar, and M. Trott, "Renormalization Group Evolution of the Standard Model Dimension Six Operators I: Formalism and lambda Dependence," *JHEP* **10** (2013) 087, arXiv:1308.2627 [hep-ph].

[149] E. E. Jenkins, A. V. Manohar, and M. Trott, "Renormalization Group Evolution of the Standard Model Dimension Six Operators II: Yukawa Dependence," *JHEP* **01** (2014) 035, arXiv:1310.4838 [hep-ph].

[150] R. Gauld, B. D. Pecjak, and D. J. Scott, "One-loop corrections to $h \to b\bar{b}$ and $h \to \tau\bar{\tau}$ decays in the Standard Model Dimension-6 EFT: four-fermion operators and the large-m_t limit," *JHEP* **05** (2016) 080, arXiv:1512.02508 [hep-ph].

[151] J. Alwall, R. Frederix, S. Frixione, V. Hirschi, F. Maltoni, O. Mattelaer, H. S. Shao, T. Stelzer, P. Torrielli, and M. Zaro, "The automated computation of tree-level and next-to-leading order differential cross sections, and their matching to parton shower simulations," *JHEP* **07** (2014) 079, arXiv:1405.0301 [hep-ph].

[152] G. Ossola, C. G. Papadopoulos, and R. Pittau, "Reducing full one-loop amplitudes to scalar integrals at the integrand level," *Nucl. Phys. B* **763** (2007) 147–169, arXiv:hep-ph/0609007.

[153] G. Ossola, C. G. Papadopoulos, and R. Pittau, "CutTools: A Program implementing the OPP reduction method to compute one-loop amplitudes," *JHEP* **03** (2008) 042, arXiv:0711.3596 [hep-ph].

[154] G. Ossola, C. G. Papadopoulos, and R. Pittau, "On the Rational Terms of the one-loop amplitudes," *JHEP* **05** (2008) 004, arXiv:0802.1876 [hep-ph].

[155] R. D. Ball *et al.*, "Parton distributions with LHC data," *Nucl. Phys. B* **867** (2013) 244–289, arXiv:1207.1303 [hep-ph].

[156] I. Brivio, Y. Jiang, and M. Trott, "The SMEFTsim package, theory and tools," *JHEP* **12** (2017) 070, arXiv:1709.06492 [hep-ph].

[157] R. Alonso, E. E. Jenkins, A. V. Manohar, and M. Trott, "Renormalization Group Evolution of the Standard Model Dimension Six Operators III: Gauge Coupling Dependence and Phenomenology," *JHEP* **04** (2014) 159, arXiv:1312.2014 [hep-ph].

[158] "Guidelines for extrapolation of cms and atlas lhc/hl-lhc couplings projections to he-lhc." https://twiki.cern.ch/twiki/bin/view/LHCPhysics/GuidelinesCouplingProjections2018#Details%20of%20the%20CMS%20projections.

[159] M. Cepeda *et al.*, "Report from Working Group 2: Higgs Physics at the HL-LHC and HE-LHC," *CERN Yellow Rep. Monogr.* **7** (2019) 221–584, arXiv:1902.00134 [hep-ph].

[160] J. Salvatier, T. V. Wiecki, and C. Fonnesbeck, "Probabilistic programming in python using PyMC3," *PeerJ Computer Science* **2** (Apr, 2016) e55. https://doi.org/10.7717/peerj-cs.55.

[161] R. Kumar, C. Carroll, A. Hartikainen, and O. Martin, "Arviz a unified library for exploratory analysis of bayesian models in python," *Journal of Open Source Software* **4** no. 33, (2019) 1143. https://doi.org/10.21105/joss.01143.

[162] J. de Blas *et al.*, "HEPfit: a Code for the Combination of Indirect and Direct Constraints on High Energy Physics Models," *Eur. Phys. J. C* **80** no. 5, (2020) 456, arXiv:1910.14012 [hep-ph].

[163] J. Ellis, M. Madigan, K. Mimasu, V. Sanz, and T. You, "Top, Higgs, Diboson and Electroweak Fit to the Standard Model Effective Field Theory," *JHEP* **04** (2021) 279, arXiv:2012.02779 [hep-ph].

[164] I. Brivio, S. Bruggisser, F. Maltoni, R. Moutafis, T. Plehn, E. Vryonidou, S. Westhoff, and C. Zhang, "O new physics, where art thou? A global search in the top sector," *JHEP* **02** (2020) 131, arXiv:1910.03606 [hep-ph].

[165] C. Zhang, "Constraining *qqtt* operators from four-top production: a case for enhanced EFT sensitivity," *Chin. Phys. C* **42** no. 2, (2018) 023104, arXiv:1708.05928 [hep-ph].

[166] **ATLAS** Collaboration, "Search for Higgs boson pair production in the two bottom quarks plus two photons final state in *pp* collisions at $\sqrt{s} = 13$ TeV with the ATLAS detector," Tech. Rep. ATLAS-CONF-2021-016, 2021.

[167] L. Alasfar, R. Gröber, C. Grojean, A. Paul, and Z. Qian, "Machine learning augmented probes of light-quark Yukawa and trilinear couplings from Higgs pair production," *In preparation* (2021) .

[168] J. Alison *et al.*, "Higgs boson potential at colliders: Status and perspectives," *Rev. Phys.* **5** (2020) 100045, arXiv:1910.00012 [hep-ph].

[169] **CMS** Collaboration, "Prospects for HH measurements at the HL-LHC," *CMS-PAS-FTR-18-019* (2018) .

[170] **FCC** Collaboration, A. Abada *et al.*, "FCC Physics Opportunities: Future Circular Collider Conceptual Design Report Volume 1," *Eur. Phys. J. C* **79** no. 6, (2019) 474.

[171] **FCC** Collaboration, A. Abada *et al.*, "FCC-ee: The Lepton Collider: Future Circular Collider Conceptual Design Report Volume 2," *Eur. Phys. J. ST* **228** no. 2, (2019) 261–623.

[172] P. Bambade *et al.*, "The International Linear Collider: A Global Project," arXiv:1903.01629 [hep-ex].

[173] **LCC Physics Working Group** Collaboration, K. Fujii *et al.*, "Tests of the Standard Model at the International Linear Collider," arXiv:1908.11299 [hep-ex].

[174] F. An *et al.*, "Precision Higgs physics at the CEPC," *Chin. Phys. C* **43** no. 4, (2019) 043002, arXiv:1810.09037 [hep-ex].

[175] **CEPC Study Group** Collaboration, M. Dong *et al.*, "CEPC Conceptual Design Report: Volume 2 - Physics & Detector," arXiv:1811.10545 [hep-ex].

[176] **CLICdp, CLIC** Collaboration, T. K. Charles *et al.*, "The Compact Linear Collider (CLIC) - 2018 Summary Report," arXiv:1812.06018 [physics.acc-ph].

[177] J. de Blas *et al.*, "The CLIC Potential for New Physics," arXiv:1812.02093 [hep-ph].

[178] S. Di Vita, G. Durieux, C. Grojean, J. Gu, Z. Liu, G. Panico, M. Riembau, and T. Vantalon, "A global view on the Higgs self-coupling at lepton colliders," *JHEP* **02** (2018) 178, arXiv:1711.03978 [hep-ph].

[179] G. Banelli, E. Salvioni, J. Serra, T. Theil, and A. Weiler, "The Present and Future of Four Top Operators," *JHEP* **02** (2021) 043, arXiv:2010.05915 [hep-ph].

[180] J. de Blas, J. C. Criado, M. Perez-Victoria, and J. Santiago, "Effective description of general extensions of the Standard Model: the complete tree-level dictionary," *JHEP* **03** (2018) 109, arXiv:1711.10391 [hep-ph].

[181] Anisha, S. D. Bakshi, S. Banerjee, A. Biekötter, J. Chakrabortty, S. K. Patra, and M. Spannowsky, "Effective limits on single scalar extensions in the light of recent LHC data," arXiv:2111.05876 [hep-ph].

[182] **ATLAS** Collaboration, M. Aaboud *et al.*, "Observation of $H \to b\bar{b}$ decays and VH production with the ATLAS detector," *Phys. Lett. B* **786** (2018) 59–86, arXiv:1808.08238 [hep-ex].

[183] **CMS** Collaboration, A. M. Sirunyan *et al.*, "Observation of Higgs boson decay to bottom quarks," *Phys. Rev. Lett.* **121** no. 12, (2018) 121801, arXiv:1808.08242 [hep-ex].

[184] T. Han and S. Willenbrock, "QCD correction to the p p —> W H and Z H total cross-sections," *Phys. Lett. B* **273** (1991) 167–172.

[185] O. Brein, A. Djouadi, and R. Harlander, "NNLO QCD corrections to the Higgs-strahlung processes at hadron colliders," *Phys. Lett. B* **579** (2004) 149–156, arXiv:hep-ph/0307206.

[186] S. Amoroso *et al.*, "Les Houches 2019: Physics at TeV Colliders: Standard Model Working Group Report," in *11th Les Houches Workshop on Physics at TeV Colliders: PhysTeV Les Houches*. 3, 2020. arXiv:2003.01700 [hep-ph].

[187] C. Englert, M. McCullough, and M. Spannowsky, "Gluon-initiated associated production boosts Higgs physics," *Phys. Rev. D* **89** no. 1, (2014) 013013, arXiv:1310.4828 [hep-ph].

[188] C. Englert, R. Rosenfeld, M. Spannowsky, and A. Tonero, "New physics and signal-background interference in associated $pp \to HZ$ production," *EPL* **114** no. 3, (2016) 31001, arXiv:1603.05304 [hep-ph].

[189] R. V. Harlander, S. Liebler, and T. Zirke, "Higgs Strahlung at the Large Hadron Collider in the 2-Higgs-Doublet Model," *JHEP* **02** (2014) 023, arXiv:1307.8122 [hep-ph].

[190] B. A. Kniehl, "Associated Production of Higgs and Z Bosons From Gluon Fusion in Hadron Collisions," *Phys. Rev. D* **42** (1990) 2253–2258.

[191] D. A. Dicus and C. Kao, "Higgs Boson - Z^0 Production From Gluon Fusion," *Phys. Rev. D* **38** (1988) 1008. [Erratum: Phys.Rev.D 42, 2412 (1990)].

[192] L. Altenkamp, S. Dittmaier, R. V. Harlander, H. Rzehak, and T. J. Zirke, "Gluon-induced Higgs-strahlung at next-to-leading order QCD," *JHEP* **02** (2013) 078, arXiv:1211.5015 [hep-ph].

[193] R. V. Harlander, A. Kulesza, V. Theeuwes, and T. Zirke, "Soft gluon resummation for gluon-induced Higgs Strahlung," *JHEP* **11** (2014) 082, arXiv:1410.0217 [hep-ph].

[194] A. Hasselhuhn, T. Luthe, and M. Steinhauser, "On top quark mass effects to $gg \to ZH$ at NLO," *JHEP* **01** (2017) 073, arXiv:1611.05881 [hep-ph].

[195] R. Harlander, J. Klappert, C. Pandini, and A. Papaefstathiou, "Exploiting the WH/ZH symmetry in the search for New Physics," *Eur. Phys. J. C* **78** no. 9, (2018) 760, arXiv:1804.02299 [hep-ph].

[196] B. Hespel, F. Maltoni, and E. Vryonidou, "Higgs and Z boson associated production via gluon fusion in the SM and the 2HDM," *JHEP* **06** (2015) 065, arXiv:1503.01656 [hep-ph].

[197] J. Davies, G. Mishima, and M. Steinhauser, "Virtual corrections to $gg \to ZH$ in the high-energy and large-m_t limits," arXiv:2011.12314 [hep-ph].

[198] L. Chen, G. Heinrich, S. P. Jones, M. Kerner, J. Klappert, and J. Schlenk, "ZH production in gluon fusion: two-loop amplitudes with full top quark mass dependence," arXiv:2011.12325 [hep-ph].

[199] R. Bonciani, G. Degrassi, P. P. Giardino, and R. Gröber, "Analytical Method for Next-to-Leading-Order QCD Corrections to Double-Higgs Production," *Phys. Rev. Lett.* **121** no. 16, (2018) 162003, arXiv:1806.11564 [hep-ph].

[200] L. Alasfar, G. Degrassi, P. P. Giardino, R. Gröber, and M. Vitti, "Virtual corrections to $gg \to ZH$ via a transverse momentum expansion," *JHEP* **05** (2021) 168, arXiv:2103.06225 [hep-ph].

[201] L. D. Landau, "On the angular momentum of a system of two photons," *Dokl. Akad. Nauk SSSR* **60** no. 2, (1948) 207–209.

[202] C.-N. Yang, "Selection Rules for the Dematerialization of a Particle Into Two Photons," *Phys. Rev.* **77** (1950) 242–245.

[203] G. Passarino and M. J. G. Veltman, "One Loop corrections for e^+e^- annihilation into $\mu^+\mu^-$ in the Weinberg Model," *Nucl. Phys.* **B160** (1979) 151.

[204] S. Larin, "The Renormalization of the axial anomaly in dimensional regularization," *Phys. Lett. B* **303** (1993) 113–118, arXiv:hep-ph/9302240.

[205] M. Spira, A. Djouadi, D. Graudenz, and P. M. Zerwas, "Higgs boson production at the LHC," *Nucl. Phys. B* **453** (1995) 17–82, arXiv:hep-ph/9504378.

[206] U. Aglietti, R. Bonciani, G. Degrassi, and A. Vicini, "Analytic Results for Virtual QCD Corrections to Higgs Production and Decay," *JHEP* **01** (2007) 021, arXiv:hep-ph/0611266.

[207] R. Mertig, M. Bohm, and A. Denner, "FEYN CALC: Computer algebraic calculation of Feynman amplitudes," *Comput. Phys. Commun.* **64** (1991) 345–359.

[208] V. Shtabovenko, R. Mertig, and F. Orellana, "New Developments in FeynCalc 9.0," *Comput. Phys. Commun.* **207** (2016) 432–444, arXiv:1601.01167 [hep-ph].

[209] H. H. Patel, "Package-X 2.0: A Mathematica package for the analytic calculation of one-loop integrals," *Comput. Phys. Commun.* **218** (2017) 66–70, arXiv:1612.00009 [hep-ph].

[210] P. Maierhöfer, J. Usovitsch, and P. Uwer, "Kira—A Feynman integral reduction program," *Comput. Phys. Commun.* **230** (2018) 99–112, arXiv:1705.05610 [hep-ph].

[211] R. Bonciani, P. Mastrolia, and E. Remiddi, "Master integrals for the two loop QCD virtual corrections to the forward backward asymmetry," *Nucl. Phys. B* **690** (2004) 138–176, arXiv:hep-ph/0311145.

[212] S. Borowka and G. Heinrich, "Massive non-planar two-loop four-point integrals with SecDec 2.1," *Comput. Phys. Commun.* **184** (2013) 2552–2561, arXiv:1303.1157 [hep-ph].

[213] S. Borowka, G. Heinrich, S. P. Jones, M. Kerner, J. Schlenk, and T. Zirke, "SecDec-3.0: numerical evaluation of multi-scale integrals beyond one loop," *Comput. Phys. Commun.* **196** (2015) 470–491, arXiv:1502.06595 [hep-ph].

[214] A. V. Smirnov, "FIRE5: a C++ implementation of Feynman Integral REduction," *Comput. Phys. Commun.* **189** (2015) 182–191, arXiv:1408.2372 [hep-ph].

[215] R. N. Lee, "LiteRed 1.4: a powerful tool for reduction of multiloop integrals," *J. Phys. Conf. Ser.* **523** (2014) 012059, arXiv:1310.1145 [hep-ph].

[216] A. von Manteuffel and L. Tancredi, "A non-planar two-loop three-point function beyond multiple polylogarithms," *JHEP* **06** (2017) 127, arXiv:1701.05905 [hep-ph].

[217] R. Bonciani, G. Degrassi, P. P. Giardino, and R. Gröber, "A Numerical Routine for the Crossed Vertex Diagram with a Massive-Particle Loop," *Comput. Phys. Commun.* **241** (2019) 122–131, arXiv:1812.02698 [hep-ph].

[218] L. Naterop, A. Signer, and Y. Ulrich, "handyG —Rapid numerical evaluation of generalised polylogarithms in Fortran," *Comput. Phys. Commun.* **253** (2020) 107165, arXiv:1909.01656 [hep-ph].

[219] S. Buehler and C. Duhr, "CHAPLIN - Complex Harmonic Polylogarithms in Fortran," *Comput. Phys. Commun.* **185** (2014) 2703–2713, arXiv:1106.5739 [hep-ph].

[220] S. Borowka, G. Heinrich, S. Jahn, S. P. Jones, M. Kerner, J. Schlenk, and T. Zirke, "pySecDec: a toolbox for the numerical evaluation of multi-scale integrals," *Comput. Phys. Commun.* **222** (2018) 313–326, arXiv:1703.09692 [hep-ph].

[221] S. Borowka, G. Heinrich, S. Jahn, S. P. Jones, M. Kerner, and J. Schlenk, "A GPU compatible quasi-Monte Carlo integrator interfaced to pySecDec," *Comput. Phys. Commun.* **240** (2019) 120–137, arXiv:1811.11720 [physics.comp-ph].